

**ANALYSIS OF INFLUENCE OF LAND USE
LAND COVER AND CLIMATE CHANGES
ON STREAMFLOW OF NETRAVATI
BASIN, INDIA**

Thesis

Submitted in partial fulfilment of the requirements for the degree of

DOCTOR OF PHILOSOPHY

by

DINU MARIA JOSE



DEPARTMENT OF WATER RESOURCES AND OCEAN ENGINEERING

NATIONAL INSTITUTE OF TECHNOLOGY KARNATAKA

SURATHKAL, MANGALORE – 575025

DECEMBER, 2022

ANALYSIS OF INFLUENCE OF LAND USE LAND COVER AND CLIMATE CHANGES ON STREAMFLOW OF NETRAVATI BASIN, INDIA

Thesis

Submitted in partial fulfilment of the requirements for the degree of

DOCTOR OF PHILOSOPHY

by

DINU MARIA JOSE

177080AM004

Under the guidance of

Dr. G S Dwarakish

Professor,

Dept. of Water Resources and Ocean Engineering

NITK, Surathkal



DEPARTMENT OF WATER RESOURCES AND OCEAN ENGINEERING

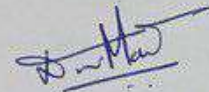
NATIONAL INSTITUTE OF TECHNOLOGY KARNATAKA

SURATHKAL, MANGALORE – 575025

DECEMBER, 2022

DECLARATION

I hereby *declare* that the Research Thesis entitled **Analysis of Influence of Land Use Land Cover and Climate Changes on Streamflow of Netravati Basin, India** which is being submitted to the National Institute of Technology Karnataka, Surathkal in partial fulfilment of the requirements for the award of the Degree of Doctor of Philosophy in **Department of Water Resources and Ocean Engineering** is a *bonafide report of the research work carried out by me*. The material contained in this Research Thesis has not been submitted to any University or Institution for the award of any degree.



Dinu Maria Jose

(177080AM004)

Department of Water Resources and Ocean Engineering

Place: NITK-Surathkal

Date: 26/12/2022

CERTIFICATE

This is to *certify* that the Research Thesis entitled **Analysis of Influence of Land Use Land Cover and Climate Changes on Streamflow of Netravati Basin, India** submitted by **DINU MARIA JOSE**, (Register Number: 177080AM004) as the record of the research work carried out by her, is *accepted as the Research Thesis submission* in partial fulfilment of the requirements for the award of degree of Doctor of Philosophy.

G.S. Dwarakish
30.12.22
Research Guide

(Name and Signature with Date and Seal)

Dr. G.S. DWARAKISH

Ph.D. (Coastal Engg. and RS & GIS)

Assistant Professor

DEPT. OF APPLIED MECHANICS AND HYDRAULICS
National Institute of Technology, Karnataka, Surathkal
P.O. SRINIVASNAGAR - 575 025



Dhanan
Chairman - DRPC

(Signature with Date and Seal)

PROFESSOR & HEAD

Dept. of Water Resources & Ocean Engineering
(Formerly Dept. of Applied Mechanics & Hydraulics)
NITK Surathkal, P.O. Srinivasnagar, Mangaluru-575025

ACKNOWLEDGEMENTS

In my journey towards the completion of my doctoral thesis, I was assisted and shown the path by numerous people.

Words are insufficient to express my sincere gratitude and thanks to my research supervisor, **Prof. G S Dwarakish**, Department of Water Resources and Ocean Engineering, NITK, Surathkal, for his infinite love, care, motivation and invaluable guidance throughout my research work. I am grateful to him for his keen interest in the preparation of this thesis. I have learnt a lot and still have plenty to learn from him. It has been my pleasure and honour to work with him.

I wish to thank **Prof. Mahesha A.**, **Prof. Amba Shetty**, and **Prof. Dodamani B M**, the successive Heads of the Department of Water Resources and Ocean Engineering, NITK, for the kind support and encouragement extended by them. I will always be grateful to all faculty members of the Department of Water Resources and Ocean Engineering, for their kind support and encouragement, throughout my tenure as a research scholar in the Department. I wish to place on record my sincere thanks to **Prof. Arkal Vittal Hegde**, **Prof. Lakshman Nandagiri**, Department of Water Resources and Ocean Engineering and **Dr. Savita Bhat**, Associate Professor, School of Management, the members of my Research Progress Assessment Committee, for their valuable suggestions and the encouragement provided at various stages of this work. Special thanks for the help extended to me by all the members of staff of the Department of Water Resources and Ocean Engineering, especially **Mr. Balakrishna**, **Mrs. Prathima**, **Ms. Sweekritha**, **Mr. Anil**, **Mr. Ananda**, **Mr. Harish**, **Mr. Seetharam** and **Mr. Gopala Krishna** during various stages of my stay at Department of Water Resources and Ocean Engineering, NITK.

Whatever I am today is because of the lifelong support of my father **Mr. Jose Joseph** and my mother **Mrs. Moly Jose**. This thesis would not have been possible without the amazing support, patience, constant encouragement, care, unfettered belief and prayers of my parents, my brother and other family members. Words aren't enough to express my gratitude for them. I am grateful to my better half **Mr. Sajan John V**, for the honest feedbacks, proofreadings, emotional support, love and care he has offered. He was with

me through all my ups and downs during this journey. I am extremely grateful to him and my in-laws for their unlimited support and encouragement during this research work. Special thanks to **Mr. Balu**, my brother from another mother; without him this journey would have been much more difficult for me. I am grateful to him and his family for the love and support they have offered.

I have plenty of love and gratitude towards my 'left' and 'right', **Mr. Tom** and **Mr. Athul** for the friends they are and will always be. Special thanks to **Ms. Amala** and others of M. Tech batch 2017-2019 for the love and support they have offered. My journey at NITK started off much colorful with their company. Thanks to my sweetest 'chechymar' **Mrs. Ashwitha**, **Mrs. Alka**, **Mrs. Nithya**, **Mrs. Anjali**, and **Mrs. Chythanya** for the immense love, care and support they have given me. Special thanks to **Mr. Parthasarathy**, **Mr. Rony**, **Mrs. Arya** and others of 'Civil+AMD+EC' for the love and support they have offered me during this journey of mine. I was fortunate to have the encouragement and support from my seniors especially **Mr. Pruthvin**, **Dr. Arun**, **Dr. Sinan**, **Dr. Diwan**, **Mr. Punithraj**, **Mr. Sahaj**, **Mr. Pandu**, and **Mr. Surajit**. Many thanks to **Mr. Waleed**, the sweetest junior, for the help and support he has offered. I am very much thankful to other friends and fellow research scholars of this institute for their continuous encouragement and suggestions during the course of my research work. The informal support and encouragement of my friends have been indispensable.

Finally, I thank the God Almighty for making all these events happen smoothly and for every one of them who has encouraged, supported and contributed to the successful completion of my doctoral research.

Dinu Maria Jose

ABSTRACT

Massive Land Use/Land Cover (LULC) change is a result of human activities. These changes have, in turn, affected the stationarity of climate, i.e., climate change is beyond the past variability. Studies indicate the effect of LULC change and climate change on the hydrological regime and mark the necessity of its timely detection at watershed/basin scales for efficient water resource management. This study aims to analyse and predict the influence of climate change and LULC change on streamflow of Netravati basin, a tropical river basin on the south-west coast of India.

For future climate data, researchers depend on general circulation models (GCMs) outputs. However, significant biases exist in GCM outputs when considered at a regional scale. Hence, six bias correction (BC) methods were used to correct the biases of high-resolution daily maximum and minimum temperature simulations. Considerable reduction in the bias was observed for all the BC methods employed except for the Linear Scaling method. While there are several BC methods, a BC considering frequency, intensity and distribution of rainfall are few. This study used an effective bias correction method which considers these characteristics of rainfall. This study also assessed and ranked the performance of 21 GCMs from the National Aeronautics Space Administration (NASA) Earth Exchange Global Daily Downscaled Projections (NEX-GDDP) dataset and bias-corrected outputs of 13 Coupled Model Inter-comparison Project, Phase 6 (CMIP6) GCMs in reproducing precipitation and temperature in the basin. Four multiple-criteria decision-making (MCDM) methods were used to identify the best GCMs for precipitation and temperature projections. For the CMIP6 dataset, BCC-CSM2-MR was seen as the best GCM for precipitation, while INM-CM5-0 and MPIESM1-2-HR were found to be the best for minimum and maximum temperature in the basin by group ranking procedure. However, the best GCMs for precipitation and temperature projections of the NEX-GDDP dataset were found to be MIROCESM-CHEM and IPSL-CM5A-LR, respectively. Multi-Model Ensembles (MMEs) are used to improve the performance of GCM simulations. This study also evaluates the performance of MMEs of precipitation and temperature developed by six methods, including mean and Machine Learning (ML) techniques.

The results of the study reveal that the application of an LSTM model for ensembling performs significantly better than models. In general, all ML approaches performed better than the mean ensemble approach.

Analysis and mapping of LULC is essential to improve our understanding of the human-nature interactions and their effects on land-use changes. The effects of topographic information and spectral indices on the accuracy of LULC classification were investigated in this study. Further, a comparison of the performance of Support Vector Machine (SVM) and Random Forest (RF) classifiers was evaluated. The RF classifier outperformed SVM in terms of accuracy. Finally, the classified maps by RF classifier using reflectance values, topographic factors and spectral indices, along with other driving factors are used for making the future projections of LULC in the Land Change Modeler (LCM) module of TerrSet software. The results reveal that the area of built-up is expected to increase in the future. In contrast, a drop in forest and barren land is expected.

The SWAT model is used to study the impacts of LULC and climate change on streamflow. The results indicate a reduction in annual streamflow by 2100 due to climate change. While an increase in streamflow of 13.4 % is expected due to LULC change by the year 2100 when compared to the year 2020. The effect of climate change on streamflow is more compared to LULC change. A reduction in change is seen in the streamflow from near to far future.

Keywords: Climate change, Bias correction, GCM, LULC, SWAT, Multi-model ensembles, Streamflow

TABLE OF CONTENTS

ABSTRACT	i
TABLE OF CONTENTS	iii
LIST OF FIGURES	ix
LIST OF TABLES	xiii
ABBREVIATIONS	xv
1 INTRODUCTION	1
1.1 GENERAL	1
1.2 HYDROLOGY	1
1.2.1 Streamflow	1
1.2.2 Hydrological modelling	2
1.3 CLIMATE CHANGE	2
1.3.1 Causes and impacts of climate change.....	2
1.3.2 Circulation models and climate forecasting.....	3
1.4 LAND USE LAND COVER	4
1.4.1 Causes and impacts of land use land cover change	4
1.4.2 Land use land cover prediction	4
1.5 SCOPE OF THE WORK	5
1.6 ORGANIZATION OF THE THESIS	5
2 REVIEW OF LITERATURE	7
2.1 UNCERTAINTIES IN PREDICTING IMPACTS OF CLIMATE CHANGE ON HYDROLOGY IN A BASIN SCALE	7
2.1.1 Uncertainties in climate impact studies	8

2.1.2	Climate scenarios	14
2.1.3	Climate modelling- GCMs and downscaling.....	15
2.1.4	Data and bias correction.....	16
2.1.5	Discussion	18
2.2	DETECTION OF LULC CHANGE	20
2.2.1	Use of machine learning and auxiliary datasets in LULC classification	22
2.2.2	LULC projection modelling.....	23
2.2.3	Discussion	24
2.3	HYDROLOGICAL MODELLING TO STUDY THE IMPACTS OF CLIMATE AND LULC CHANGE AT BASIN SCALE	25
2.3.1	Impacts of LULC change on hydrology	25
2.3.2	Impacts of climate change on hydrology	26
2.3.3	Combined effects of climate change and LULC change	26
2.3.4	Model comparison studies	27
2.3.5	Discussion	28
2.4	LITERATURE GAPS	35
2.5	OBJECTIVES OF THE STUDY.....	36
2.6	STUDY AREA.....	36
3	DATA PRODUCTS AND METHODOLOGY	39
3.1	DATA PRODUCTS	39
3.1.1	Bias correction (BC)	39
3.1.2	Ranking of GCMs.....	40
3.1.2.1	Observed precipitation and temperature dataset	40
3.1.2.2	GCM precipitation and temperature dataset	40
3.1.3	Creation of MMEs	41
3.1.4	LULC prediction.....	41
3.1.5	Hydrological modelling	49

3.2	METHODOLOGY	49
3.2.1	Bias correction	51
3.2.1.1	Bias correction of rainfall	51
3.2.1.2	Bias correction of temperature.....	54
3.2.2	Ranking of GCMs	61
3.2.2.1	Performance indicators for evaluating GCMs	61
3.2.2.2	Normalization and weight computation of indicators.....	63
3.2.2.3	Multicriteria decision-making techniques.....	64
3.2.2.4	Group decision-making.....	67
3.2.3	Creation of MMEs	68
3.2.3.1	Data Preparation.....	69
3.2.3.2	Principal Component Analysis	69
3.2.3.3	Machine Learning Algorithms.....	70
3.2.3.4	Performance Evaluation.....	73
3.2.4	LULC change detection and prediction	74
3.2.4.1	Data processing.....	74
3.2.4.2	LULC classification.....	75
3.2.4.3	Selection of the best classification scenario.....	76
3.2.4.4	Training and validation	76
3.2.4.5	LULC prediction.....	77
3.2.5	Hydrological modelling using SWAT	77
4	RESULTS AND DISCUSSION	79
4.1	INTRODUCTION.....	79
4.2	BIAS CORRECTION.....	79
4.2.1	Bias correction of rainfall	79
4.2.1.1	Distribution of rainfall in the basin.....	79
4.2.1.2	Evaluation of simulated data.....	81
4.2.1.3	Evaluation of Bias Correction method.....	83
4.2.2	Bias correction of temperature.....	85

4.2.2.1	Evaluation of bias correction methods.....	85
4.3	RANKING OF GCMS.....	92
4.3.1	Performance indicators and weights	93
4.3.2	Ranking of the GCMs by different MCDM techniques and their comparison 94	
4.3.3	Group ranking of GCMs	99
4.3.4	Discussion.....	108
4.4	CREATION OF MMEs.....	109
4.4.1	Performance Evaluation of MMEs in the case of precipitation.....	110
4.4.1.1	Performance evaluation of MMEs for daily rainfall.....	110
4.4.1.2	Performance Evaluation of MMEs for monsoon season	114
4.4.2	Performance evaluation of MMEs in the case of maximum temperature .	119
4.4.3	Performance evaluation of MMEs in the case of minimum temperature ..	122
4.4.4	Inter-comparisons of performance of different MMEs.....	126
4.5	LULC CHANGE DETECTION AND PREDICTION.....	126
4.5.1	Classification in GEE.....	126
4.5.2	Prediction of future LULC using TerrSet	130
4.5.3	Discussion	135
4.6	HYDROLOGICAL MODELLING USING SWAT	135
5	SUMMARY AND CONCLUSIONS	139
5.1	SUMMARY AND CONCLUSIONS	139
5.1.1	Bias correction	139
5.1.1.1	Bias correction of rainfall	139
5.1.1.2	Bias correction of temperature.....	140
5.1.2	Ranking of GCMs	141
5.1.3	Ensembling of GCMs	142
5.1.4	LULC change detection and prediction	143

5.1.5 Hydrological modelling using SWAT	144
5.2 LIMITATION OF THE STUDY.....	144
5.3 SCOPE OF FUTURE WORK	145
REFERENCES-----	147
PUBLICATIONS-----	175
BRIEF BIO-DATA-----	177

List of Figures

Figure 2.1 Location of study area-Netravati basin.....	37
Figure 3.1 Methodology.....	50
Figure 3.2 Methodology followed for ranking of GCMs	62
Figure 3.3 Architecture of a LSTM cell.....	74
Figure 3.4 Representation of SWAT methodology	78
Figure 4.1 Location of Raingauge Stations.....	80
Figure 4.2 Station-wise monthly distribution of rainfall during the period 1971–2014	80
Figure 4.3 Station-wise trend of annual rainfall during 1971 and 2014	81
Figure 4.4 Average rainy days during the period 1971–2014	82
Figure 4.5 Average annual cycle of precipitation during the period 1971–2014	82
Figure 4.6 Spatially averaged daily precipitation Q-Q plot of observed and corrected/uncorrected simulated precipitation for the validation period	83
Figure 4.7 Taylor diagram of spatially averaged observed, uncorrected and bias-corrected monthly precipitation during the period 2001– 2014.....	84
Figure 4.8 Q-Q plots comparing the observed and bias corrected/uncorrected simulated maximum temperature of an example grid cell during the validation period 1995–2014.	86
Figure 4.9 Q-Q plots comparing the observed and bias corrected/uncorrected simulated minimum temperature of an example grid cell during the validation period 1995–2014	87
Figure 4.10 Taylor diagram of observed, uncorrected and bias-corrected maximum temperature of an example grid cell during the validation period 1995–2014.	88
Figure 4.11 Taylor diagram of observed, uncorrected and bias-corrected minimum temperature of an example grid cell during the validation period 1995–2014.	89
Figure 4.12 Annual distribution of bias corrected maximum temperature values along with observed and uncorrected maximum temperature values for one year	90
Figure 4.13 Annual distribution of bias corrected minimum temperature values along with observed and uncorrected minimum temperature values for one year	91

Figure 4.14 GCMs occupying first positions by a) VIKOR, b) TOPSIS, c) weighted average and d) PROMETHEE-II methods in the case of precipitation for NEX-GDDP dataset	97
Figure 4.15 GCMs occupying first positions by a) VIKOR, b) TOPSIS, c) weighted average and d) PROMETHEE-II methods in the case of precipitation for CMIP6 dataset	97
Figure 4.16 GCMs occupying first positions by a) VIKOR, b) TOPSIS, c) Weighted Average and d) PROMETHEE-II methods in the case of maximum temperature for NEX-GDDP dataset	101
Figure 4.17 GCMs occupying first positions by a) VIKOR, b) TOPSIS, c) Weighted Average and d) PROMETHEE-II methods in the case of minimum temperature for NEX-GDDP dataset	101
Figure 4.18 GCMs occupying first positions by a) VIKOR, b) TOPSIS, c) Weighted Average and d) PROMETHEE-II methods in the case of maximum temperature for CMIP6 dataset.....	102
Figure 4.19 GCMs occupying first positions by a) VIKOR, b) TOPSIS, c) Weighted Average and d) PROMETHEE-II methods in the case of minimum temperature for CMIP6 dataset.....	102
Figure 4.20 GCMs occupying first four positions after group decision-making technique in the case of precipitation for NEX-GDDP dataset	104
Figure 4.21 GCMs occupying first four positions after group decision-making technique in case the of maximum temperature for NEX-GDDP dataset	104
Figure 4.22 GCMs occupying first four positions after group decision-making technique in the case of minimum temperature for NEX-GDDP dataset	105
Figure 4.23 GCMs occupying first four positions after group decision-making technique in the case of precipitation for CMIP6 dataset	105
Figure 4.24 GCMs occupying first four positions after group decision-making technique in case the of maximum temperature for CMIP6 dataset	106
Figure 4.25 GCMs occupying first four positions after group decision-making technique in the case of minimum temperature for CMIP6 dataset.....	106

Figure 4.26 Scatter plot of observed and MME simulated monthly precipitation for NEX-GDDP dataset	111
Figure 4.27 Scatter plot of observed and MME simulated monthly precipitation for CMIP6 dataset.....	112
Figure 4.28 Taylor diagram of observed and MME simulated monthly precipitation of NEX-GDDP dataset during the validation period	113
Figure 4.29 Taylor diagram of observed and MME simulated monthly precipitation of CMIP6 dataset during the validation period	113
Figure 4.30 Scatter plot of observed and MME simulated monthly monsoon precipitation for NEX-GDDP dataset	116
Figure 4.31 Scatter plot of observed and MME simulated monthly monsoon precipitation for CMIP6 dataset.....	117
Figure 4.32 Taylor diagram of observed and MME simulated monthly monsoon precipitation of NEX-GDDP dataset during the validation period.....	118
Figure 4.33 Taylor diagram of observed and MME simulated monthly monsoon precipitation of CMIP6 dataset during the validation period.....	118
Figure 4.34 Taylor diagram of observed and MME simulated average monthly maximum temperature of NEX-GDDP dataset during the validation period.....	119
Figure 4.35 Scatter plot of observed and MME simulated average monthly maximum temperature for NEX-GDDP dataset	120
Figure 4.36 Scatter plot of observed and MME simulated average monthly maximum temperature for CMIP6 dataset	121
Figure 4.37 Taylor diagram of observed and MME simulated average monthly maximum temperature of CMIP6 dataset during the validation period	122
Figure 4.38 Scatter plot observed and MME simulated average monthly minimum temperature for NEX-GDDP dataset	123
Figure 4.39 Scatter plot of observed and MME simulated average monthly minimum temperature for CMIP6 dataset.....	124
Figure 4.40 Taylor diagram of observed and MME simulated average monthly minimum temperature of NEX-GDDP dataset during the validation period	125

Figure 4.41 Taylor diagram of observed and MME simulated average monthly minimum temperature of CMIP6 dataset during the validation period	125
Figure 4.42 Graphical representation of percentage change in the LULC classes from 1990 to 2020	129
Figure 4.43 LULC classification using RF	129
Figure 4.44 Driver variables for the CA–Markov model	132
Figure 4.45 Graphical representation of percentage change in the LULC classes from 2020 to 2100	133
Figure 4.46 Predicted LULC for the years 2030, 2040, 2050, 2075 and 2100.....	134
Figure 4.47 Observed and simulated monthly streamflow in the validation period at Bantwal gauging station.....	136

List of Tables

Table 2.1 Studies evaluating various sources of uncertainties in climate impact studies	9
Table 2.2 Advantages and disadvantages of downscaling methods (Trzaska and Schnarr 2014)	16
Table 2.3 Studies on impacts of land use land cover on hydrology	29
Table 2.4 Studies on impacts of climate change on hydrology	31
Table 2.5 Studies on impacts of land use land cover and climate change on hydrology	33
Table 3.1 Twenty-one CMIP5 models included in NEX-GDDP dataset	42
Table 3.2 Thirteen CMIP6 models considered in the study.....	46
Table 3.3 Data Products used as input for SWAT model	49
Table 3.4 Performance of QDM based on the size of the moving window used	59
Table 3.5 Spectral indices and formula.....	75
Table 4.1 Performance of bias correction methods in correcting monthly precipitation time series (2001-2014).....	85
Table 4.2 Performance of bias correction methods in correcting maximum temperature daily time series (1995-2014)	92
Table 4.3 Performance of bias correction methods in correcting minimum temperature daily time series (1995-2014)	92
Table 4.4 Performance indicators for precipitation simulated by the NEX-GDDP dataset at the the grid with latitude 12.5° and longitude 75.5°.....	94
Table 4.5 Selected GCMs (first rank) for precipitation at different grid points in the basin for the NEX-GDDP dataset using different methods.....	95
Table 4.6 Selected GCMs (first rank) for precipitation at different grid points in the basin for the CMIP6 dataset using different methods.....	96
Table 4.7 Selected GCMs (first rank) for maximum and minimum temperature at different grid points in the basin for NEX-GDDP dataset using different methods	98
Table 4.8 Selected GCMs (first rank) for maximum and minimum temperature at different grid points in the basin for CMIP6 dataset using different methods.....	99

Table 4.9 Correlation between ranks obtained from different MCDM techniques for the NEX-GDDP dataset	103
Table 4.10 Correlation between ranks obtained from different MCDM techniques for the CMIP6 dataset	103
Table 4.11 Ranking of NEX-GDDP dataset for the basin	107
Table 4.12 Ranking of CMIP6 dataset GCMs for the basin	108
Table 4.13 Performance of various MMEs in simulating daily P, T _{min} and T _{max} ..	110
Table 4.14 Performance of various MMEs in simulating monsoon P	115
Table 4.15 Accuracy results for each modelling scenario	127
Table 4.16 Comparison of κ and OA for SVM and RF	127
Table 4.17 Cramer's V for each driver variable	130
Table 4.18 Area (%) of each LULC class	131
Table 4.19 Parameters and ranges used in the sensitivity analysis and ranking	136
Table 4.20 Percentage change in streamflow due to climate change	137
Table 4.21 Percentage change in streamflow due to LULC change	137
Table 4.22 Percentage change in streamflow due to LULC change and climate change	138

List of Abbreviations

Abbreviation	Meaning
ANN	Artificial Neural Network
API	Application Programming Interface
AQM	Adjusted Quantile Mapping
AR5	Fifth Assessment Report
AR6	Sixth Assessment Report
BC	Bias Correction
BCSD	Bias-Correction Spatial Disaggregation
BHO	Bayesian Hyperparameter Optimisation
BSI	Bare Soil Index
CA	Cellular Automata
CART	Classification And Regression Decision Tree
CDF	Cumulative Distribution Function
CMIP5	Fifth phase of Coupled Model Intercomparison Project
CMIP6	Sixth phase of Coupled Model Intercomparison Project
CORDEX	Coordinated Regional Downscaling Experiment
CUP	Calibration and Uncertainty Program
DC	Delta Change
DEM	Digital Elevation Model
DM	Distribution Mapping
DSM	Digital Surface Model
EQM	Empirical Quantile Mapping
ERTS	Earth Resources Technology Satellite
ETM+	Enhanced Thematic Mapper Plus
ETR	Extra Tree Regressor
GCM	General Circulation Models
GEE	Google Earth Engine

GPD	Generalised Pareto Distribution
GHG	Greenhouse Gases
GIS	Geographical Information System
GMFD	Global Meteorological Forcing Dataset
GPQM	Gamma-Pareto Quantile Mapping
HRU	Hydrologic Response Unit
IMD	India Meteorological Department
IPCC	Intergovernmental Panel on Climate Change
JAXA	Japanese Aerospace Exploration Agency
LC	Land Cover
LCM	Land Change Modeller
LI	Local Intensity
LLS	Linear Least Square
LS	Linear Scaling
LSTM	Long Short-Term Memory
LU	Land Use
LULC	Land Use Land Cover
MAE	Mean Absolute Error
MC	Markov Chain
MCDM	Multi-Criteria Decision Making
MIPI	Multi-Indicator Preference Index
ML	Machine Learning
MLC	Maximum Likelihood Classifier
MLP	Multilayer Perceptron
MLR	Multiple Linear Regression
MME	Multi-Model Ensemble
MNDWI	Modified Normalised Difference Water Index
MSL	Mean Sea Level
NASA	National Aeronautics and Space Administration
NCCS	NASA Centre for Climate Simulation
NDBI	Normalised Difference Built-Up Index

NDVI	Normalised Difference Vegetation Index
NEX-GDDP	NASA Earth Exchange Global Daily Downscaled Projections
NIR	Near Infrared
NSE	Nash-Sutcliffe Efficiency
OA	Overall Accuracy
OLI	Operation Land Images
OOB	Out Of Bag
PBIAS	Percentage Bias
PC	Principle Component
PCA	Principle Component Analysis
PDF	Probability Distribution Function
PT	Power Transform
QDM	Quantile Delta Mapping
Q-Q Plot	Quantile-Quantile Plot
r	Correlation Coefficient
R ²	Coefficient of Determination
RCM	Regional Climate Model
RCP	Representative Concentration Pathways
RF	Random Forest
RMSD	Root Mean Square Deviation
RMSE	Root Mean Square Error
SCS	Soil Conservation Service
SD	Standard Deviation
SRES	Special Report on Emission Scenarios
SS	Skill Score
SSP	Shared Socio-Economic Pathways
SST	Sea Surface Temperature
SUFI – 2	Sequential Uncertainty Fitting Ver. 2
SVM	Support Vector Machines
SVR	Support Vector Regression

SWAT	Soil and Water Assessment Tool
SWIR	Shortwave Infrared
TF	Transfer Function
TM	Thematic Mapper
UC	Un-Corrected
UGB	Upper Ganges Basin
VC	Vapnik-Chervonenkis
VS	Variance scaling
WCRP	World Climate Research Program
κ	Kappa Coefficient

CHAPTER 1

INTRODUCTION

1.1 GENERAL

The environment has been altered by human activities for thousands of years (Vitousek 1994). A considerable increase in population, migration and socio-economic activities has led to drastic changes in the environment over the last few decades. These changes have, in turn, affected the stationarity of climate, i.e. climate change is beyond the past variability (Milly et al. 2008). Massive Land Use/Land Cover (LULC) change is a result of human activities. Studies indicate the effect of LULC change on the hydrological regime and mark the necessity of its timely detection at appropriate scales for efficient water resource management (Isik et al. 2013). These two influencing forces (LULC and climate change) can affect the hydrological components at global, continental, regional and basin scales in all parts of the world (Praskievicz and Chang 2009). Hydrological modelling is an important tool which is used by researchers all over the world for analysing the influence of climate change and LULC change on natural water sources and for predicting potential future impacts from various possible scenarios.

1.2 HYDROLOGY

The science of occurrence, movement and distribution of water on earth and its atmosphere is termed as hydrology. Hydrology involves processes like evapotranspiration, condensation, precipitation, runoff and percolation. These processes form the hydrological cycle. Runoff is generated by draining off of precipitation from an area through a channel (Subramanya, 2008). Streamflow represents the runoff part of the hydrological cycle.

1.2.1 Streamflow

Streamflow is the discharge of a stream or river expressed as volume per unit time. The quantity varies with space and time. Excess streamflow might lead to a flooding event. And lack of streamflow is unfavourable to humans and the ecosystem. So, monitoring the same with the knowledge of its quantity and quality is vital for the proper

management and design of water resources projects. The path travelled by stream and its volume is influenced by physical and ecological changes. For example, the streamflow reduces due to afforestation and increases due to deforestation (Meter et al. 2016). Climatic factors like rainfall and temperature have a direct influence on streamflow. The magnitude and distribution of rainfall play a vital role in streamflow generation. So an analysis of climate change and land use land cover is necessary (Yirsaw et al. 2017).

1.2.2 Hydrological modelling

Hydrologic models are simplified representations of the real-world hydrologic system (Moradkhani and Sorooshian 2009). Various factors which affect the hydrologic system include climate change, land use, topography, geology etc. (Praskievicz and Chang 2009). With the help of hydrologic models, the impact of these factors on the hydrologic system can be ascertained.

The models can be mainly classified based on their physical and spatial structure (Krysanova and Srinivasan 2015). The models can be grouped as distributed, semi-distributed and lumped based on the representation of spatial heterogeneity at the watershed scale (Dwarakish and Ganasri 2015). Distributed and semi-distributed models capture the spatial variability better than the lumped models (Bormann et al. 2009). Depending on the process description, models can be categorised as conceptual, empirical and physical. Based on the consideration of randomness, models are classified as stochastic and deterministic models. Former involves randomness while the latter does not (Dwarakish and Ganasri 2015).

1.3 CLIMATE CHANGE

1.3.1 Causes and impacts of climate change

Climate change has been of worldwide concern, and recent happenings have confirmed the world's growing susceptibility to the same. As a result of the burning of fossil fuels, there has been an increase in the amount of CO₂ and other Greenhouse gases (GHGs). This has led to the 'Greenhouse effect', which is the rise in the temperature (Pielke et al. 2011). The forest cover which acts as 'carbon sinks' shows a declining trend.

The influence of climate change on hydrological processes is widely investigated (Gosain et al. 2006; Narsimlu et al. 2013; Pervez and Henebry 2015). As climate change intervenes in the hydrological cycle, there would be changes in the pattern of precipitation and temperature, which would, in turn, affect the water resources of an area. Therefore, it is significant to explore the trend of climate change and its future impact on hydrology.

1.3.2 Circulation models and climate forecasting

The General Circulation Models (GCMs) are the advanced tool for the prediction of climate data (Chen et al. 2017). These are numerical models driven by the principles of radiative heat transfer, thermodynamics, and fluid dynamics. GCM has the capability to represent physical processes associated with the land surface, ocean, atmosphere, and cryosphere. The response of these processes to changes in GHG concentration can be evaluated. But, GCMs are inept at giving climate data information to higher resolutions. In this case, Regional Climate Models (RCMs) are used to convert GCM data to finer scales (Van Vuuren et al. 2011). Nevertheless, for accurate climate data, there is a need for bias correction of RCM outputs.

Since 1990, the Intergovernmental Panel on Climate Change (IPCC) has been developing long-term emission scenarios. These scenarios have progressed from the IS92 in 1992 to the Special Report on Emission Scenarios (SRES) in 2000. In the Fifth Assessment Report (AR5) of IPCC, the SRES got replaced by Representative Concentration Pathways (RCPs). The effect of GHGs is represented by radiative forcing. RCPs with four radiative forcing form the basis of modelling experiments. These pathways are developed up to the year 2100 with a radiative forcing of 2.6, 4.5, 6.0 and 8.5 W/m² (Jubb et al. 2013) and hence named RCP2.6, RCP4.5, RCP6.0, and RCP8.5. The Shared Socio-economic Pathways (SSPs) are the most recent version of the scenarios used for the Sixth phase of Coupled Model Intercomparison Project (CMIP6) and IPCC Sixth Assessment Report (AR6). The SSPs scenarios are the most complex ones developed to date and range from very ambitious emission reduction to continuous emission growth. New versions of the scenarios -RCP2.6, RCP4.5, RCP6.0, and RCP8.5 can be found in CMIP6. These new scenarios, which go by the names

SSP1-2.6 (SSP126), SSP2-4.5 (SSP245), SSP4-6.0 (SSP460), and SSP5-8.5 (SSP585), each produce radiative forcing levels in 2100 that are comparable to those of their predecessors in AR5. For CMIP6, a series of additional scenarios are also being employed to provide scientists with a larger range of potential futures to simulate. SSP1-1.9, SSP4-3.4, SSP5-3.4OS, and SSP3-7.0 are the new ones.

1.4 LAND USE LAND COVER

1.4.1 Causes and impacts of land use land cover change

Land Cover (LC) denotes the natural distribution of a region as forests, wetlands, grasslands etc. Whereas Land Use (LU) is an alteration of the natural distribution of land by humans for buildings, roads etc. Change in LULC affects the land-river ecosystem and hence causes changes in streamflow and sediment yield (Gyamfi et al. 2016a). These changes are due to changes in evapotranspiration, canopy interaction, and topography.

Alterations of streamflow and sediment yield in a watershed are two noticeable hydrological responses to changes in LULC. Quantification of the same is required for efficient water resource management. For this, a change detection analysis has to be done. Remote sensing and Geographical Information System (GIS) techniques prove to be more efficient than conventional approaches (Rawat and Kumar 2015). Hence the use of satellite images for LULC change detection is preferred.

1.4.2 Land use land cover prediction

Land use land cover change models typically predict where or how much change would potentially occur in the future. This is done by knowing the factors which affect the land use change. The major factors include population, distance to roads, type of soil, former land use etc. (Veldkamp and Lambin 2001). The choice of model would depend on the factors which influence the change. Prediction of LULC change in the future is crucial for the understanding of protentional modifications that might happen in the future. These predictions would help land use planners, resource managers, and conservation practitioners in planning and better decision-making (Halmy et al. 2015).

1.5 SCOPE OF THE WORK

The study has explored the efficiency of various bias correction techniques in correcting the biases in precipitation and temperature predicted by GCMs. Further, an attempt has been made to rank bias corrected GCM outputs based on their ability to simulate the climate variables (precipitation and temperature) in the historical time period. The efficiency of various techniques to create multi-model ensembles of GCMs is also explored. This study focused on determining how future precipitation and temperature will affect streamflow under various emission scenarios given by IPCC (RCP 4.5, RCP 8.5, SSP126, SSP245, SSP370 and SSP485). Additionally, the study evaluated the effects of the LULC change on the Netravati basin's streamflow. The effect of LULC on future streamflow is also studied by projecting the future LULC through the Cellular Automata (CA)-Markov model with the help of various driving factors. The effect of auxiliary datasets and Machine Learning (ML) classifiers like Support Vector Machines (SVM) and Random Forest (RF) on LULC classification accuracy has also been examined. Finally, the study determines the effect of LULC and climate change on streamflow of Netravati basin using the Soil and Water Assessment Tool (SWAT). This study aids planners and decision-makers in developing site-specific adaptation and mitigation strategies to lessen the anthropogenic and climate change impacts in the Netravati basin. The scope of this study is set to Netravati basin.

1.6 ORGANIZATION OF THE THESIS

The five chapters that make up this thesis are divided into the following sections.

Chapter 1: In the first chapter, the study's background and scope were defined.

Chapter 2: There are six main sections in this chapter. The first three sections covered the studies related to climate change data analysis, LULC classification and hydrological modelling at the basin scale. The fourth section summarises the literature gaps identified and key conclusions from these studies. In the fifth chapter, the objectives of this study are given. Finally, the study area used in this research is introduced.

Chapter 3: The data products and the methodology used for fulfilling each objective of this study are outlined in this chapter.

Chapter 4: The findings from the study and their detailed discussion are given in this chapter.

Chapter 5: The summary of the findings and conclusions drawn from the study are presented in this last chapter. This chapter is followed by the references used for the study.

REVIEW OF LITERATURE

2.1 UNCERTAINTIES IN PREDICTING IMPACTS OF CLIMATE CHANGE ON HYDROLOGY IN A BASIN SCALE

The IPCC gives regular scientific assessments on climate change. Climate change, as a result of global warming, influences the availability and distribution of water as it affects the rate of climatic extremes like drought, flood and heat waves (IPCC 2012). Climatic factors like rainfall and temperature have a direct influence on streamflow and are site-specific (Boorman and Sefton 1997). The magnitude and distribution of rainfall play a vital role in streamflow generation. The influence of climate change on hydrological processes is widely investigated. Some studies have also analysed the effect of climate change on water quality (Azadi et al. 2019). As climate change intervenes in the hydrological cycle, there will be changes in the pattern of precipitation and temperature, which would, in turn, affect the water resources of an area. The ambiguity related to water resources sustainability will influence agriculture, socio-economy, and the environment. The effect of climate change on developing countries would be significant as the population is largely dependent on agriculture (Worqlul et al. 2017). Climate change impacts differ between watersheds or even smaller areas due to their unique characteristics and sensitivity to changes (Mamuye and Kebebewu 2018). Modelling these changes at a regional scale is thus necessary. Even though advances are made in climate physics and its response to the increase in greenhouse gases, it is hard to predict the effect of climate change on individual locations. There are uncertainties involved at every stage of hydrological impact assessment of climate change at a local scale. They are: scenario uncertainty in climate scenario selection, model uncertainty in climate simulation by GCMs, uncertainties while downscaling GCMs/RCMs, biases in RCMs, erroneous input to the hydrological model, and finally the uncertainty structure and parameterization of the hydrological model (Kundzewicza et al. 2018; Mujumdar 2013). A crucial aspect of assessing the predictability of the

hydrological impact of climate change is the quantification of the total uncertainty associated with the results (Maraun et al. 2010).

2.1.1 Uncertainties in climate impact studies

A considerable amount of uncertainty is involved in the physical response of a hydrological system to changes in climatic variables like precipitation and temperature. To quantify these sources of uncertainties, the application of multiple scenarios and models is required (Mileham et al. 2009). The effect of these uncertainties on impact analysis change with location, methodology and focus area. It is essential to determine the sensitivity of impact studies to various uncertainties. For example, the uncertainty involved in streamflow prediction could be due to uncertainties involved in GCMs, scenarios, downscaling and model parameterisation (Basheer et al. 2016). Table 2.1 provides some of the studies which have considered various uncertainties involved in climate impact studies. Measurement of uncertainty can determine the confidence limit of model results and thus help in efficient policy making.

Table 2.1 Studies evaluating various sources of uncertainties in climate impact studies

Author	Parameters considered	Impact variable	Major conclusions
(Jiang et al. 2007)	Eight GCM simulations (CCSM3, CNRM-CM3, ECHAM5/MPI-OM, ECHO-G, IPSL-CM4, MIROC3.2, PCM, UKMO-HadCM3), two emission scenarios (A1B, B1) and four hydrologic models (Sacramento Soil Moisture Accounting (SAC-SMA) model, Thornthwaite-Mather model (TM) Conceptual HYdrologic MODel (HYMOD) and the Precipitation Runoff Modelling System (PRMS))	Runoff change	Hydrological model uncertainty is lesser than GCM uncertainty, except during the dry season, implying that the hydrological model selection is important when evaluating the hydrologic climate change impact.
(Minville et al. 2008)	5 GCMs (HadCM3, ECHAM4, CSIRO, CCSRNIES and GCM3) and two emission scenarios (A2 and B2)	Streamflow	The most significant uncertainty is from the choice of a GCM.
(Bastola et al. 2011)	Three GCMs, two emission scenarios, and four conceptual hydrological models	Streamflow	The uncertainty from the choice of GCM is larger than from the emission scenario.

(Chen et al. 2011)	Two emission scenarios (A2, B1), six GCMs (CGCM3, GFDL-CM2.0, MPI-ECHAM5, CSIRO-Mk3.5, MIROC3.2-medres, MRI-CGCM2.3), five GCM initial conditions, four downscaling techniques, three hydrological model structures (HSAMI, HMETs and Hydrotel), and ten sets of hydrological model parameters.	Mean annual and seasonal discharges, peak discharge, annual low flow (95%), time to peak discharge, time to the beginning of the flood and time to the end of the flood	Choice of GCM is a major contributor to uncertainty.
(Nóbrega et al. 2011)	Greenhouse gas emission scenarios (A1b, A2, B1, B2) 6 GCMs (CCCMA CGCM31, NCAR CCSM30, CSIRO Mk30, IPSL CM4, MPI ECHAM5, UKMO HadGEM1)	Mean monthly river flow	A greater source of uncertainty is from the GCM than from the emission scenario
(Dobler et al. 2012)	Three GCMs (ECHAM5, HadCM3, BCM), 3 RCMs (RCA, REMO, RACMO), three bias correction methods (delta change method, local scaling, and quantile mapping), 17 hydrological model parameters	Mean annual runoff, Mean monthly runoff and 10% and 1% flow exceedance probabilities	Uncertainty with GCM structure is found to be important

(Jung et al. 2012)	Two emission scenarios (A1B and B1), two basins (Clackamas River Basin and Tualatin River Basin) and eight general circulation models (CCSM3, CNRM-CM3, ECHAM5/MPI-OM, ECHO-G, IPSL-CM4, MIROC3.2(hires), PCM, UKMO-HadCM3, CCS) and hydrological parameters	Runoff	Snow-dominated regions require more attention as winter runoff is more affected by hydrologic model parameter uncertainty.
(Xu et al. 2012)	Three scenarios (A1B, A2 and B1) and three GCMs (HadCM3, ECHAM5, CCSM3)	24-hr design rainfall depth	Paper concludes that uncertainty arises from emission scenarios, GCMs, downscaling approaches and impact analysis models.
(Karlsson et al. 2016)	Four climate models (ARPEGE-RM5.1, ECHAM5-HIRHAM5, ECHAM5-RCA3, HadCM3-HadRM3), three hydrological models (NAM, SWAT and MIKE SHE) and four land use scenarios (Agriculture for nature, high-tech agriculture, extensive agriculture and market driven agriculture)	Mean, one percentile and 99 percentiles of streamflow and hydraulic head.	Choice of climate models is ascertained as most important, followed by the structure of the hydrological model chosen.

(Su et al. 2017)	Five GCMs (GFDL-ESM2M, HadGEM2-ES, IPSL-5 CM5ALR, MIROC-ESM-CHEM, and NorESM1-M), four RCP scenarios and four hydrological models (HBV, SWAT, SWIM and VIC)	Annual average discharge, daily peak discharge and seasonal high flow	Climate input is the greatest source of uncertainty
(Valentina et al. 2017)	<p>Nine Hydrological models (ECOMAG, mHM, SWAT, SWIM, HBV, HYMOD, HYPE, VIC and WaterGAP3)</p> <p>12 basins (Rhine and Tagus in Europe, Ganges, Lena, Upper Yellow and Upper Yangtze in Asia, Niger and Blue Nile in Africa, Upper Mississippi, MacKenzie and Upper Amazon in America, and Darling in Australia)</p> <p>Five GCMs (GFDL-ESM2M, HadGEM2-ES, IPSL- CM5A-LR, MIROC-ESM-CHEM, and NorESM1-M)</p> <p>Four RCPs (RCP2.6, RCP4.5, RCP6.0 and RCP8.5)</p>	Projected two annual runoff quantiles Q10 and Q90 and annual mean flow	Uncertainty was 27% for RCPs, 57% for GCMs and 16% for hydrological models

(Vetter et al. 2017)	Nine hydrological models, four RCPs, five Coupled Model Intercomparison Project Phase 5 GCMs	The two runoff quantiles Q10 and Q90 and the mean flow	Uncertainties associated with GCMs are the highest, followed by RCPs, and then hydrological models.
(Das et al. 2018)	Five GCM (ACCESS1.0, CNRM-CM5, CCSM4, GFDL-CM3, MPI-ESM-LR, NorESM1-M), two scenarios (RCP 4.5 and 8.5)	Streamflow	Uncertainty associated with GCM is more significant than the scenario uncertainty.
(Hattermann et al. 2018)	Five climate models (HadGEM2-ES, IPSL-CM5A-LR, GFDL-ESM2M, MIROC-ESM-CHEM, NorESM1-M), thirteen hydrological models (ECOMAG, HBV, HYMOD, HYPE, mHM, SWAT, SWIM, VIC, WaterGAP3, H08, MPI-HM, PCR-GLOBWB and WBM), nine large scale river basins and four RCPs	Daily river discharge	Climate model related uncertainty is the largest

2.1.2 Climate scenarios

Emission scenarios are plausible future emissions of GHGs based on an internally consistent set of assumptions on driving forces like demographic, technological and socio-economic changes and their interactions (Riahi et al. 2017). These are formed as a result of collaboration between climate, terrestrial ecosystem, integrated assessment, and emission inventory modellers. According to the storyline of RCP 4.5, the rate of population growth will reduce, the economy will display a steady growth, and solid land-use regulations will be ascertained such that environmental preservation is suitably valued (Thomson et al. 2011). While the RCP 8.5 storyline proposes that urban demands will rise with population growth connected with relatively low economic development and society will concentrate more on development than on environmental preservation (Kim et al. 2013). Thus, each RCP trajectory is an outcome of specific socio-economic and technological development scenarios. So, the selection of RCP plays a significant role in rightly predicting future impacts of climate change (Kundu et al. 2018).

The socioeconomic and technological developments in the future are mostly inexplicable and may not be similar to historical changes. The levels of emissions will depend on the mitigation policy that will be taken in the future, as it would affect the anthropogenic contribution to emissions. Hence it is recommended not to go for a single best or average case but to go for a range of possible scenarios (Kundzewicza et al. 2018; Vano et al. 2015).

In the near future, climate scenario uncertainties will have a smaller effect compared to climate model uncertainties. This is because the near-term climate is much dependent on past emissions, whereas the far future climate is much more sensitive to the uncertainty in emission scenarios (Vetter et al. 2017). Nevertheless, climate change scenarios are commonly used for studying the future impacts of changing climate. For planning long-term projects, climate scenario uncertainties are to be given due importance. Decisions should be made considering all plausible future climatic conditions (Ntegeka et al. 2014; Talchabhadel and Karki 2019). Katz (2002) suggests giving weights to the scenarios according to their likelihood, as all scenarios are not equally likely.

The right scenario is often considered the one which projects the present well. However, one has to consider the future parameters like LULC, SSPs etc., before deciding on the scenarios. SSPs are mapped to RCPs by O'Neill et al. (2014). New scenarios incorporating SSPs are being developed considering the future changes of both climate and society to find climate impacts along with possible adaptation and mitigation options (O'Neill et al. 2017).

2.1.3 Climate modelling- GCMs and downscaling

Although GCMs are beneficial in predicting future emissions, they do not detect fine-scale heterogeneity in climate change because of their coarser resolution (Kour et al. 2016; Maurer and Hidalgo, 2008; Xu, 2000). Fine-scale climate information is required to study its potential impact on hydrology at a local scale. This process of deriving fine-scale information from coarser GCM outputs is termed as downscaling. Downscaling can be spatial (e.g., 500 km grid cell GCM output to a 20 km resolution) or temporal (e.g., monthly rainfall data to daily rainfall data) (Trzaska and Schnarr 2014).

The process of downscaling involves uncertainties due to underlying assumptions. There are statistical and dynamical downscaling methods (Laflamme et al. 2016). In statistical downscaling, an empirical relationship between historical large-scale atmospheric and local climate variables is established. It assumes that the relationship between the predictor and the predictand remains stationary over time. This method is appropriate if time and financial resources are limited (Wilby and Wigley 1997). Dynamical downscaling uses RCM, which is similar to a GCM in its principles but has a higher resolution. This method is consistent and physically based but requires more computational power (Tang et al. 2016). Table 2.2 summarises the pros and cons of both downscaling methods.

Table 2.2 Advantages and disadvantages of downscaling methods (Trzaska and Schnarr 2014)

	Dynamic Downscaling	Statistical Downscaling
Disadvantages	<p>Resolution is limited to 20–50 km</p> <p>Require a substantial amount of data input</p> <p>RCMs have trouble in accurately simulating convective precipitation and extreme precipitation</p> <p>Require high computational resources and expertise</p> <p>RCMs may need as much processing time as a GCM to compute projections</p> <p>It may require further downscaling and bias correction of RCM outputs</p>	<p>It assumes that present-day statistical relationships between large and regional scale variables will remain the same in the future.</p> <p>Requires a substantial amount of good observational data</p>
Advantages	<p>It can provide information at sites with no observational data</p> <p>Ability to model local atmospheric processes and land cover changes explicitly</p> <p>Not constrained by historical records so that novel scenarios can be simulated</p>	<p>Ability to give site-specific or station-scale climate projections</p> <p>Methods are freely available and range from simple to intricate</p> <p>Few methods can even capture extreme events</p> <p>Require medium/low computational resources and volume of data inputs</p>

2.1.4 Data and bias correction

Hydrological models require high-resolution meteorological forcing data for climate impact assessments. Thus, RCMs provide more dependable results than GCMs in the case of regional climate impact studies. As hydrological models are often calibrated with observational data, they are sensitive to biases in the meteorological forcing data. However,

meteorological data directly obtained from RCMs have a considerable bias. Hence, different bias correction methods are to be applied before using these data in hydrological models (Dobler and Ahrens 2008; Hay et al. 2002; Piani et al. 2010; Wood et al. 2002). Xu et al. (2019) have reviewed dynamic downscaling methods and have concluded that the ultimate way to get accurate climate simulations is by improving climate models. However, in the current scenario, bias correction is an efficient method for improving downscaled data.

Teutschbein and Seibert (2012) analysed the performance of six bias correction methods, namely linear scaling, variance scaling, local intensity scaling, power transformation, distribution transfer and the delta-change approach and found that distribution mapping performed the best in streamflow simulation of the five Swedish catchments considered in the study. The choice of the bias correction method has a significant role in hydrological impact studies. Mudbhatkal and Mahesha (2018) evaluated the performance of four bias correction methods (linear scaling (LS), delta change (DC), variance scaling (VS), and the distribution mapping (DM)) for temperature and five bias correction methods (local intensity (LI) scaling, LS, DC, DM, VS, power transform (PT)) for precipitation in the Western Ghats of India. The study found that the DC method is the best for bias correction in the study area and emphasised the need for evaluating the performance of various bias correction methods before choosing one. Various other studies have assessed the performance of bias correction methods (Berg et al. 2012; Mudbhatkal and Mahesha 2018; Piani et al. 2010; Teutschbein and Seibert 2012). Employing daily correction factors instead of monthly correction factors is better as it gives a smooth transition (Smitha et al. 2018). The selection of the precipitation correction method is more crucial than the selection of the temperature correction method as the RCMs/GCMs better represent the temperature domain than the precipitation domain (Fang et al. 2015).

Bias correction methods improve the raw RCM values, but their level of success varies. It can be done only if observations are available for the variable of interest. And so, bias correction is as good as the observations used for the process. Data used must be consistent

and adequate (Kauffeldt et al. 2013). Studies have evaluated the errors and inconsistencies in datasets (Pechlivanidis and Arheimer 2015). The effect of poor data on the calibration of models is discussed by Beven and Smith (2015) and Beven and Westerberg (2011). Due to poor observational data, there are chances of rejecting good models and accepting bad ones. So input data for calibration or bias correction should be given due care. Kim, Kwon, and Han (2015) employed a method to reduce the distributional parametric uncertainty included with observational and climate model data.

2.1.5 Discussion

Impact studies of climate change involve various uncertainties. As knowledge stock expands with time, the uncertainty range also expands as various factors which were ignored earlier are uncovered (Blöschl and Montanari 2010; Hawkins and Sutton 2009; Kundzewicza et al. 2018). Thus, cutting-edge methodologies can improve uncertainty quantifications (Katz et al. 2013; Zhang et al. 2014). Uncertainties are considered as barriers to climate change adaptation. Addressing these uncertainties can significantly improve future predictions and thus improve climate adaptation options (Kusangaya et al. 2014). As a result revealing, reducing and representing uncertainties is necessary for planning water resource adaptation strategies (Clark et al. 2016).

Uncertainties connected with GCMs and emission scenarios are found to be the largest among all uncertainties (Kundzewicza et al. 2018). Considering a large number of models for doing a detailed climate impact assessment is often unfeasible with existing computational and human resources. In practice, a single climate model or a small ensemble of climate models is chosen for the assessment. A single model is often selected based on its ability to simulate present and past climate (past performance approach). Selection of an ensemble of models which represent the full uncertainty range and the region of interest is not straightforward. It needs evaluation of multiple criteria (Evans et al. 2013). Uncertainties related to climate model projections are often the largest source of uncertainty in climate impact studies (Minville et al. 2008). Therefore, the selection of climate model is a critical step in climate impact studies (Lutz et al. 2016).

On the other hand, in the prospect of longer planning, the uncertainties related to climate scenario selection are of prime importance. Future climate projections are heavily influenced by the emission scenario chosen. There is a high amount of uncertainty associated with future emissions of greenhouse gases from human activities (Holman et al. 2019). It is essential to understand that the relative importance of sources of uncertainties changes over time. Therefore, a decision-making framework for future development must consider the timescale of planning before deciding the relative importance of the different sources of uncertainties (Chaumont 2014).

GCM outputs require downscaling before being used for local or fine-scale impact studies. The selection of a suitable downscaling method depends on the resource and time constraints (Trzaska and Schnarr 2014). Correction of biases can considerably reduce the errors in raw RCM climatic variables (Woldemeskel et al. 2014). But, the level of success depends on the bias correction method selected for the process. For current conditions, a single best bias correction method is reasonable enough. But when it comes to future climate, the basic assumption of stationarity in bias correction procedures makes the selection process questionable. Thus, there is a need to find new ways to account for the biases involved in RCM simulations, or RCM simulations have to be improved in the first place (Teutschbein and Seibert 2012).

Model evaluation enhances the scientific reliability and acceptance of modelled results of climate change impact studies. Multi-model ensembles outputs are more reliable than those given by individual models (Bhatt and Mall 2015). Hydrological models with flexible structures and better representation of hydrological processes are needed in the future (Dams et al. 2015). Climate models and impact models are expected to be better integrated in the future. The problems with scale mismatch between models would thus be solved. It would help water managers and other stakeholders in the efficient management of available water resources in this era of climate change (Oyebode et al. 2014). For the time being, it is essential to rely on multi-step attribution in which human activities affecting climate change result in hydrological changes.

Based on the review, the following key points are emphasised:

- Uncertainties due to climate scenarios in the near future are smaller compared to far future climate. A range of possible climate scenarios is recommended for impact studies as future emissions would be largely dependent on mitigation policies taken in the future, which are uncertain. The use of a single best or average case climate scenario may be misleading.
- GCMs are often the largest contributors to uncertainty, followed by climate scenarios and impact models. Care has to be taken while interpreting a single GCM output. Selection of a representative GCM ensemble which is manageable and accounts for the uncertainties involved is recommended.
- GCM simulations need downscaling in order to apply them for regional or local impact studies. The choice of the downscaling method solely depends on the requirement of spatial and temporal scales as well as on the time and computational constraints.
- Generally, raw RCM simulations are severely biased. Precipitation simulation correction is more crucial than temperature simulation correction as temperature fields are often better represented by RCMs. Bias correction methods can make simulations significantly better. The best bias correction methods are case specific.
- Impact studies use either a multi-model ensemble or a single model after evaluating their performance. Latter is recommended for regional-scale studies where adaptation strategies would be taken based on the result.

2.2 DETECTION OF LULC CHANGE

One of the most noticeable ways that humans are changing the ecosystem of the globe is through LU/LC alteration. One of the key research areas in landscape ecology is the investigation of the causes, mechanisms, and effects of LULC (Frazier et al. 2019). In order to better understand the functioning of the land use system and to aid in land use planning and policy, models that predict land use change are used (Koko et al. 2020). The causes that alter land usage over time in a particular location are known as driving factors. The driving factors have an impact at various temporal and spatial scales and comprise a

complex system of dependencies, interactions, and feedback loops (Ganasri et al. 2013). The four categories of driving forces that affect the land use pattern identified are economical, biophysical, institutional/policy and social/cultural. Market forces, trade agreements and policies, economic policy, land use and tenure policies, and economic policy are some examples of the economic driving forces. Rainfall, runoff, and topography are examples of biophysical factors. National and international policies to maintain biodiversity and the natural climate are examples of institutional/policy driving forces. Urbanization, immigration, population dynamics, and cultural change are some of the social and cultural driving forces (Anwar et al. 2022; Berihun et al. 2019). Height, slope, distance from the river, soil erosion, soil drainage, distance from main roads, distance from a built-up area, and population density are all elements that affect land-use change in any region or watershed (Hyandye 2015; Kamwi et al. 2018). However, in order to predict future trends in land use change, it is vital to take into account various policies and scenarios (Campbell et al. 2005).

Both spatial and non-spatial data are necessary for the analysis of how land use patterns evolve over time and the identification of driving forces. One of the effective sources of geographical and temporal data is remote sensing data. It is quicker and less time-consuming than the conventional approach (Çöltekin et al. 2020). Satellite photographs are one of the most often used sources for analysis. Launched in 1972 as Earth Resources Technology Satellite (ERTS)-1, Landsat was given its current designation in 1975. Eight sets of satellites have been launched by Landsat, and its data has been continuously available for approximately 50 years. Landsat 7 and Landsat 8 are now operational. This series of satellites has become one of the most significant long-term publicly available data for civilian uses in a variety of fields, including coastal surveillance, LULC, vegetation phenology, and hydrology (Abijith et al. 2020; Banskota et al. 2014; Parthasarathy et al. 2022). Therefore, Landsat provides a deeper understanding of LULC changes for better resource management and decision-making.

2.2.1 Use of machine learning and auxiliary datasets in LULC classification

Detailed LULC information at local, regional and global scales is essential for numerous environmental applications, like management of natural resources, sustainable development and climate change (Chokkavarapu and Mandla 2017; Govind and Ramesh 2019; Kondraju et al. 2014; Rajbongshi et al. 2018). Remotely sensed satellite data are widely used for this purpose (Alshari and Gawali 2021). However, for areas with heterogeneous vegetation structure and extensive human-induced LULC disturbance with high intra-class variability and low inter-class separability, usage of multispectral satellite data alone is insufficient for achieving high accuracy in LULC classifications (Debats et al. 2016; Hurskainen et al. 2019). In order to improve the accuracy of LULC classification, researchers have attempted to combine satellite data and auxiliary datasets (also known as ancillary, collateral or multi-source data) (Qu et al. 2021). Obtaining high classification accuracy in heterogeneous and complex areas can be challenging with the sole use of spectral band information. Thus, exploring the role of different auxiliary data in improving classification accuracy is necessary. These techniques increase the precision of LULC categorization since they are based on the concept that the distribution of vegetation is directly or indirectly connected to environmental elements such terrain, geology, soil, climate, and water availability (Franklin 1995; Maxwell et al. 2019). Remote sensing indices are also used as auxiliary data for LULC classification (Izurieta et al. 2017; Naboureh et al. 2020; Qu et al. 2021).

Even though the usage of auxiliary data for improving the LULC classification accuracy is a topic of interest for 40 years, its wider use is limited by two major reasons: a) tedious work of collecting the data from various sources and b) computational and storage requirements for processing a larger number of features used for classification (Phiri and Morgenroth 2017; Richards et al. 1982). To resolve these problems, many cloud computing platforms have been developed. Google Earth Engine (GEE) is one of the most commonly used platform (Xie et al. 2019). GEE provides a powerful and free cloud-based platform for geospatial analysis which can directly call satellite imagery and various types of

geospatial datasets for complex calculations and processing (Gorelick et al. 2017). The GEE platform also makes it possible to implement different ML algorithms for the classification process (Shelestov et al. 2017; Xie et al. 2019). The past two decades saw the usage of several ML algorithms. Among these SVM and RF have gained utmost popularity in LULC classification for several remote sensing applications (Sheykhmousa et al. 2020). A RF classifier builds numerous decision trees using a random selection of training samples and variables. It is a type of multi-decision tree ensemble classifier (Ali et al. 2012). SVM is a reliable and effective approach for both classification and regression. The support vectors at the borders of the class domain are used by the SVM to construct hyperplanes across classes in feature space. The model looks for the best hyperplane to divide the classes by a wide margin (Cervantes et al. 2020).

2.2.2 LULC projection modelling

The two types of land use change models are aspatial and spatially explicit, respectively. Empirical-statistical models, as opposed to spatial optimization models, have been created to identify the driving forces behind land-use changes and forecast future patterns of land-use change in response to changing driving forces as defined in scenarios (Ren et al. 2019). Top-down dynamics models and bottom-up dynamics models are the two primary categories of dynamics models (Ganasri et al. 2013). While the bottom-up model reflects the micro spatial pattern, the top-down model deals with the macro drivers. Top-down models include System Dynamics (SD) and Artificial Neural Networks (ANN), whereas bottom-up models include Cellular Automata. The complex interaction between the micro-spatial pattern of land use change is simulated by the CA model. Consequently, using a bottom-up strategy is an effective way to research the complexity of spatial automatic changes (Wang et al. 2022).

An effective assessment for standardisation and compatibility between data sets, as well as the ability to map, depends on the appropriate current and future use of the land. Modelling of LULC transitions and predictions is necessary for environmental planning and

management strategies. Several studies in the past have revealed that Land Change Modeler (LCM), which is based on an integrated multilayer perceptron (MLP) with a Markov chain (MC), is a reliable model for the prediction of LULC change (Kumar et al. 2016; Nath et al. 2020; Shahi et al. 2020). To comprehend the mechanisms influencing the spatiotemporal distribution of LULC and to forecast future LULC changes, a CA-Markov chain model is applied. This hybrid model combines the CA and the Markov chain model to predict the change in LULC (Hamad et al. 2018). The Markov chain model predicts a cell's transition probability, or how likely it is that the cell will shift from one state to another. The Markov chain model does not consider the influence of nearby cells over one another, which is a drawback. Consequently, it is incapable of spatial modelling (Ghalehtimouri et al. 2022). For future estimation, the CA model only considers the relevant surrounding cell. Thus, the CA-Markov model was created to examine the spatiotemporal changes in the land cover using the two models in combination. To examine the change in trend, two LULC time periods are used as the input. This software helps with analysis and model development when the land cover is steady as opposed to when the environment is changing quickly. According to Friehat et al. (2015), LCM makes it easier to compare LULC categories, the net change experienced by each class, and the factors contributing to the net change experienced by each other LULC category.

2.2.3 Discussion

LULC alteration has numerous environmental effects that have made it a global concern. It is a key component that directly influences the hydrology of a watershed. The hydrological cycle gets affected in various ways by LULC (Garg et al. 2019). The distribution of precipitation into interception, infiltration, evapotranspiration, surface runoff, and groundwater recharge are impacted by changes in LULC. Water scarcity, flood risk, and erosion rate can all rise as a result of LULC variations (Näschen et al. 2019). Therefore, it is crucial to comprehend how LULC change may affect a watershed.

2.3 HYDROLOGICAL MODELLING TO STUDY THE IMPACTS OF CLIMATE AND LULC CHANGE AT BASIN SCALE

Hydrological models are widely used across the world for studying the effects of various processes on water resources and thus for predicting potential future impacts on the same (Praskievicz and Chang 2009). The models can be mainly classified based on their physical and spatial structure (Krysanova et al. 2015). The models can be grouped as distributed, semi-distributed and lumped based on the representation of spatial heterogeneity at the watershed scale (Dwarakish and Ganasri 2015). Distributed and semi-distributed models capture the spatial variability better than the lumped models (Bormann et al. 2009). Depending on the process description, models can be categorized as conceptual, empirical and physical. Based on the consideration of randomness, models are classified as stochastic and deterministic models. The former involves randomness while the latter doesn't (Dwarakish and Ganasri 2015).

Latitude, topography, geology, and land use affect the hydrological impacts of climate in a basin. The rise in the surface runoff and undesirable high and low storm hydrograph are significant impacts of land use land cover change (Praskievicz and Chang 2009). The changes in climate and LULC are interconnected and are capable of modifying hydrological processes (Legesse et al. 2003; Li et al. 2009). Nevertheless, the influence of climate and LULC change on the hydrological regime are frequently researched separately. For example, there are research done to find out the influence of LULC change on evaporation losses (Dias et al. 2015), infiltration rates (Weatherhead and Howden 2009), and runoff volume (Hundecha and Bárdossy 2004). And there are studies which predict how climate change affects streamflow (Mudbhatkal and Mahesha 2017; Piao et al. 2010; Treesa et al. 2017), groundwater recharge (Soro et al. 2017), sediment load (Rodríguez-Blanco et al. 2016) and water quality (Glavan et al. 2015).

2.3.1 Impacts of LULC change on hydrology

There are many studies which evaluate the impact of LULC change on various temporal and spatial scales (Fan and Shibata 2015; Zhou et al. 2013). As a result of anthropogenic

activities, there has been a subsequent increase in impervious areas. This leads to the alteration of the water balance of the catchment, with an increase in runoff, decrease in evapotranspiration and groundwater recharge. Factors like altitude, slope, distance from the river, type of agricultural practices, type of soil and magnitude of erosion, frequency of drought and flood, population density and distance from a built-up area affect the rate of LULC change (Lin et al. 2009). The magnitude of impacts depends on several factors like soil depth, precipitation events, the spatial layout of deforestation areas, area of the watershed (Bi et al. 2014) etc. Numerous research have been done to study the effects of LULC on the hydrological regime (Table 2.3).

2.3.2 Impacts of climate change on hydrology

Climate change has weakened the stationarity principle, a basic concept in water resource engineering which says that future hydrological events will fluctuate within the past variability (Milly et al. 2008). This is a result of human intervention in the natural processes of earth leading to changes in the means and extremes of evapotranspiration, precipitation and runoff. Studies are done to understand the trend of extreme rainfall events using various statistical methods (Babar and Ramesh 2014).

Commonly used climate change scenarios were those which are in SRES of IPCC AR4 (Ficklin et al., 2009; Tu, 2009; Yoshimura et al., 2009; Praskievicz and Chang, 2011). The scenarios of AR5 of the IPCC, i.e., RCPs have become common. The new scenarios named SSP are yet to be explored. Table 2.4 shows the studies conducted to ascertain the effects of climate change on various hydrologic parameters.

2.3.3 Combined effects of climate change and LULC change

Hydrological models simulate the impacts of climate and human activities on the hydrological regime when the hydro-meteorological data are fed to them. These can be used for finding the individual impacts of the same on streamflow. This is done by simulating the streamflow by assuming one of them constant and changing the other (Dey and Mishra 2017). SWAT has been extensively used for studying the effects of changing

climate and land use land cover on streamflow (Dixon and Earls 2012). SWAT is equally popular in water quality studies (Glavan et al. 2015). Models like AVGWLF (Tu 2009), SWIM (Krysanova et al. 2015), PRMS (Legesse et al. 2003), MIKESHE (Wang et al. 2013), GR2M (Ahn and Merwade 2014), GBHM(Ma et al. 2010) etc. are also used for the same purpose. Studies considering both climate change and land use effects are shown in Table 2.5.

2.3.4 Model comparison studies

Tegegne et al. (2017) compared two conceptual models (GR4J, IHACRES) and a semi-distributed model (SWAT) in four watersheds of Ethiopia. The results could not conclude that any specific model was better than the other in all the watersheds. The conceptual models performed better in smaller watersheds than in largest watersheds while SWAT performed better in largest watershed. Depending on the watershed, the model performance varied. The study further combined the models using ANN and found a reduction in RMSE (Root Mean Square Error) values. Coupling semi-distributed models with ANN can improve the prediction of daily streamflow (Noori and Kalin 2016). These hydrological models need meteorological data, topographic data like Digital Elevation Model (DEM), soil etc. An approach to integrate different models can help in better understanding the response of watersheds to LULC change and climate change (Kundu et al. 2017).

Krysanova and Hattermann (2017) made a comparison of the impacts of climate change on 12 basins distributed in important geographical zones. The hydrological models used were ECOMAG, HBV, HYMOD, HYPE, mHM, SWAT, SWIM, VIC and WaterGAP3. The climate scenarios were simulated using HadGEM2-ES, IPSL-CM5A-LR, MIROC-ESM-CHEM, GFDL-ESM2M and NorESM1-M considering RCP2.6, RCP4.5, RCP6.0 and RCP8.5. The study concludes that the uncertainty associated with projections depends largely on the selected GCM, followed by the selected RCP, and the hydrological model selected is the least contributor.

2.3.5 Discussion

There is a huge usage of hydrological models in the study of impacts of land use land cover and climate change on water quality and quantity. Although there are uncertainties associated with the modelling process, it can be useful in understanding the complex interaction of various components and gives possible ranges of impacts in the coming years. There is a necessity for more studies evaluating the effects of climate change and land use land cover in many basins, as their interactive impacts are likely to occur and are not well understood. There are several gaps in the area of hydrological modelling that could improve the accuracy of the outputs. Improvements in the downscaling methods, choice of models, and quality of input data can improve the efficiency of the modelling exercise. Quantification of uncertainties associated with the modelling results could improve the reliability of modelled future projections.

In the land use land cover change studies, the sensors on the Landsat series of satellites are the popular ones because of the high temporal resolution and free availability of data. And SWAT is the most popular among the hydrological models because it is less data-intensive but gives reasonably accurate results. Based on the results of various modelling studies, it can be concluded that, depending on the characteristics of watershed and scenario assumptions, the combined effects of climate change and LULC change may ameliorate or deteriorate each other's influence. These effects may vary with the season or land use classes involved in change. Hydrological modelling integrating future climate change and LULC change scenarios can be an effective tool in planning future water resource management strategies.

Table 2.3 Studies on impacts of land use land cover on hydrology

Author(s)	Study area	Study period	Hydrological model	DEM/ Satellite	Key conclusions	Parameter
(Babar and Ramesh 2015)	Netravathi River Basin, India	2001-2009	SWAT and RCRM	ASTER/I RS 1D LISS-3, Landsat	Sensitive parameters for the SWAT model were ascertained. RCRM which requires few input parameters can predict stream flows acceptably.	Surface runoff
(Sinha and Eldho 2018)	Netravathi river basin, India	1972, 1979, 1991, 2000, 2012 and 2030	SWAT	ASTER/ Landsat	An increase in sediment yield and streamflow was observed due to the increase in the urban and agricultural area and a decrease in the forest, leading to changes in the hydrological regime.	Streamflow and sediment yield
(Zhu and Li 2014)	Little River Watershed, Tennessee	1984-2010	SWAT	National Elevation Dataset - DEM, Landsat	Overall a 3% increase in streamflow for the whole watershed. 34.6% sediment and about 10% nutrient reduction from 1984 to 2010, closely related to the decrease in agricultural land	Streamflow, Sediment yield, Total nitrogen, Total phosphorous

(Petchpra yoon et al. 2010)	Yom watershed, Thailand	1990-2006	MIKE 11	Landsat	The rate of increase in discharge in areas downstream of the rapid urbanisation was significantly greater than that of other areas.	Peak river discharge
(Gyamfi et al. 2016b)	Olifants Basin, South Africa	2000-2013	SWAT	SRTM/ Landsat	An increase of 46.97% in surface runoff generation was observed. Urbanization was revealed as the strongest contributor to increases in surface runoff generation, water yield and evapotranspiration	Surface runoff, Lateral flow, Water yield, Groundwater Lateral flow, ET, Groundwater

Table 2.4 Studies on impacts of climate change on hydrology

Author (s)	Study area	Study period	Hydrological model	GCM/RCM	Key conclusions	Scenario	Parameter
(Narsimlu et al. 2013)	Upper Sind River Basin, India	1992-2098	SWAT	PRECIS RCM	A significant increase in the runoff and baseflow is predicted. An increase in streamflow during monsoon season and a decrease in the offseason are also predicted.	IPCC A1B Scenario s	Surface runoff
(Ficklin et al. 2009)	San Joaquin River watershed, US	1992-2005	SWAT	-	The 50-year averaged outcomes show that the basin is highly sensitive to future climate changes.	IPCC A1F1 and B1	Evapotranspiration, water yield, streamflow

(Treesa et al. 2017)	Wainganga river basin, India	1971-2040	VIC	CanESM2, IPSL-CM5A-MR, MIROC-ESM, ACCESS1-0, GISS-E2-R and GFDL-ESM2M	Streamflow did not show a significant increase in the monsoon season but in the non-monsoon season.	RCP 4.5	Streamflow
(Soro et al. 2017)	Bandama Basin, West Africa	1986–2085	GR2M model	HadGEM2-ES model under	The results of the simulated impacts for RCP 4.5 and 8.5 were very different. The study highlights that there are huge uncertainties associated with impacts studies done with models	RCP 4.5 and RCP 8.5	Surface water and groundwater
(Rwigi et al. 2016)	Sondu River basin, Kenya	1961-2050	SWAT	PRECIS	The study predicts an overall increase in water yields with wetter dry seasons and drier wet seasons in the future.	IPCC A2	Water yields

Table 2.5 Studies on impacts of land use land cover and climate change on hydrology

Author (s)	Study Area	Study period	Hydrological model	Results	Parameter studied	Emission Scenario	GCM(s)/RCM(s)
(Chawla and Mujumdar 2015)	Upper Ganga basin (UGB), India	1971 to 2100	VIC model	Streamflow is extremely sensitive to modifications in the urban stretch while moderately sensitive to modifications in croplands. Climate change has a higher impact on streamflow than LULC change.	Streamflow	RCP 4.5, RCP 8.5	ACCESS1.0 (ACC), CNRM-CM5 (CNR), CCSM4 (CCS), GFDL-CM3 (GFD), MPI-ESM-LR (MPI) and NorESM1-M (NOR),
(Ahn and Merwade 2014)	Indiana, New York, Arizona and Georgia area	1950 to 2010	GR2M	The impact of human influence on streamflow is greater than that of climate impact.	Streamflow		-

(Kundu et al. 2017)	Elbow River watershed in southern Alberta, Canada	1961-2070	MIKE SHE/MIKE 11 is	From the seasonal assessment it was understood that the LULC and climate change scenario gave higher streamflow in spring. The study emphasizes on the fact that based on the direction and magnitude of impact LULC change and climate change can offset or magnify each other's influence on the hydrological regime.	Streamflow	A1B, B2	NCARPCM and CGCM2
(Kim et al. 2013)	Hoeya River Basin, Korea	2020-2050	SWAT	The effect of LULC is less than that of climate change.	Streamflow	RCP 4.5, 8.5	HadGEM3-RA
(Mango et al. 2011)	Mara River Basin, Kenya	2002-2099	SWAT	Large variations in runoff were seen from small variations in precipitation and land use land cover.	Streamflow	A1B	Minimum, median and maximum of 21 global models in the MMD (multi-model data set)

2.4 LITERATURE GAPS

Both climate change and LULC change have an impact on hydrology. Since there is a complex interaction between LULC and climate change, it is difficult to clearly understand their effect on hydrological processes by just considering one of them (Notebaert et al. 2011). Thus, an integrated modelling method is necessary to examine the combined influence of climate and LULC changes on the hydrological system. From the past studies, it is noticed that there are few studies which have evaluated the combined effects of future climate change and future LULC on the streamflow. Among the studies which have been done in the Netravati basin, no study evaluated the effects of future climate change and LULC on streamflow. Also, a long-term analysis of future effects of LULC changes on the streamflow beyond 2030 is not done. So, there is a necessity for a study which does the evaluation of future LULC and climate change on streamflow.

LULC prediction is based on historical LULC maps and other driving factors. Usage of auxiliary datasets and ML algorithms for classification are scarce. GCMs or downscaled GCMs, which are used for future climate predictions, are often severely biased and require bias correction. Evaluation of the performance of each bias correction method is necessary before choosing one. When it comes to the prediction of future climate change impacts on hydrology, many of the Coupled Model Intercomparison Project Phase 5 (CMIP5) models and all CMIP6 model outputs are not explored in the Netravati basin. There is a necessity for evaluation of the performance of GCMs before using it for impact analysis at a local scale. To the best of the author's knowledge, studies which rank GCMs at a basin scale are scarce in India. Further, studies evaluating GCMs of different generations are few. Moreover, studies ranking of CMIP6 GCMs is limited. Many of the earlier studies used the outputs of a single GCM. Recently, usage of ensembles of several GCMs known as Multi-Model Ensembles (MMEs) has been recommended. Studies using ML techniques and comparing their performances in creating MMEs are few.

2.5 OBJECTIVES OF THE STUDY

Based on the literature review, the following objectives are formulated for the present research work.

- To identify the best bias correction method for precipitation and temperature in Netravati Basin.
- To rank the GCMs according to their performance in simulating precipitation and temperature in Netravati Basin.
- To compare different ensembling methods for the creation of multi-model ensembles.
- To analyse the historical trend of LULC change and to predict the future trend of LULC change in Netravati Basin.
- To ascertain and predict the effect of LULC and climate changes on streamflow of Netravati Basin.

2.6 STUDY AREA

Western Ghats of India, also known as ‘Sahyadri Ranges’ is one of the biodiversity hotspots of the world (Myers et al. 2000). Netravati basin with an area of about 3415 km² is located in the central zone of Western Ghats of India, between 12°30'N and 13°10'N latitudes and 74°50'E and 75°50'E longitudes (Figure 2.1). The basin has a tropical monsoon climate with an average annual rainfall of around 4000 mm. It has a river gauging station at Bantwal which is nearly 25 km from the mouth of the river. The rainfall is distributed in three seasons, namely, pre-monsoon (March-May), south-west monsoon (June-September), and north-east monsoon (October-December). The south-west monsoon contributes about 70-80% of annual precipitation. The climate is marked by heavy rainfall, high humidity, and harsh weather in the hot season. The weather is very humid throughout the year, exceeding 85% during June and July months (Simpson 1921). The average daily temperature from March to May is 35°C, while in the coolest part of the year, during December, the daily average temperature goes below 20°C. The elevation of the basin varies from 0 to 1884 m with respect to the Mean Sea Level (MSL). The upper part of the basin mainly consists of sandy clay loam soil, while the lower parts consist of clay loam soil. Geologically, the basin is of Precambrian

formations. The thickness of top laterite layer decreases towards the coast. A thin layer of clay is formed underneath the porous lateritic layer because of heavy leaching in the rainy season. The upstream parts of the river are mountainous with dense forest coverage, while the lower parts are undulated plains with predominant agriculture and urban lands. Netravati river is a major source of water for agriculture, industries and civic life in cities like Mangaluru, Bantwal, Puttur, Dharmasthala, Ujire etc., in the basin.

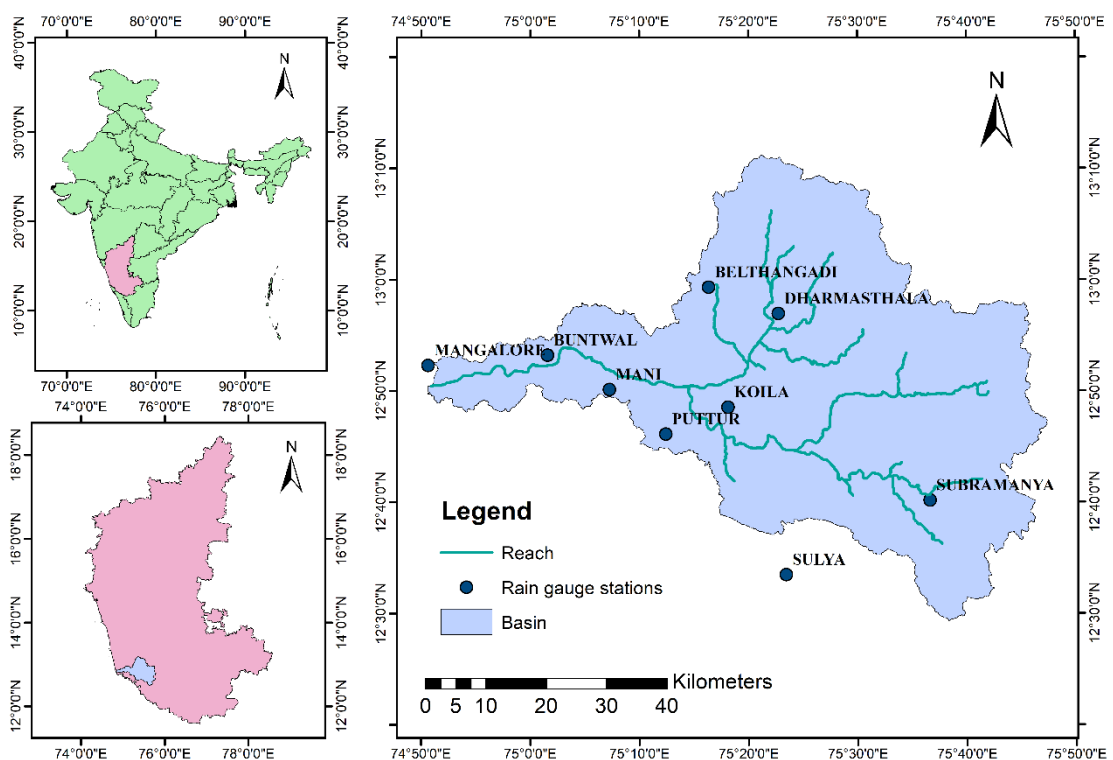


Figure 2.1 Location of study area-Netravati basin

Netravati river is a part of the project in which the waters of west flowing rivers are being diverted to the east. The Yettinahole Diversion Project aims to transfer water from the west to the eastern end of the state by diverting the head waters of the Gundia River (a tributary of the Kumardhara, which is a tributary of the Netravati). There have been discussions about the project's technological, social, and economic viability as well as its significant effects on the environment of the Eastern Plains and the Western Ghats. So, studies on the streamflow quantity which is affected by climate and LULC change are necessary.

DATA PRODUCTS AND METHODOLOGY

3.1 DATA PRODUCTS

The datasets for this study are given in this chapter. The details about the data used for each objective are given under the corresponding section headings as given below.

3.1.1 Bias correction (BC)

In this study, high-resolution precipitation and temperature simulations of Meteorological Research Institute atmospheric GCM version 3.2 (MRI-AGCM3-2-S) at a daily timescale with a horizontal grid size of about 20 km is used. This dataset is generated as a part of the CMIP6 assessment and is downloaded from the World Climate Research Programme (WCRP) climate data portal (<https://esgf-node.llnl.gov/search/cmip6/>). Mizuta et al. (2012) gives more information about the model and mention its better performance in simulating precipitation and temperature. Precipitation, maximum and minimum temperature data from 1950 to 2014 simulated by the model is used for BC. The model gives future data from 2015 to 2050 using SST/sea-ice derived from CMIP5 RCP8.5 simulations and a scenario as close to RCP8.5 as possible within CMIP6. Hereafter, the MRI-AGCM-2-S model is referred to as GCM in sections 3.1.1, 3.2.1, 4.2 and 5.1.1.

The rain gauge station data is used as the observational dataset instead of gridded observational datasets in the case of precipitation. Consistent and continuous daily rainfall data available at nine stations in and around the basin from the year 1971 to 2014 (overlapping with GCM data) was used to correct the biases in the model simulation. The rain gauge station locations are shown in Figure 2.1.

The 1° longitude \times 1° latitude spatial resolution gridded daily maximum and minimum temperature dataset generated by Indian Meteorological Department (IMD) was used as the reference or observation dataset in this study (Srivastava et al. 2009). This data is available from 1951 and is developed based on the observations collected from 395 quality-controlled stations using a modified version of Shepard's angular distance

weighting algorithm for interpolation. The data was accessed through IMD Pune's website

(http://www.imdpune.gov.in/Clim_Pred_LRF_New/Grided_Data_Download.html).

This dataset is extensively used in climate-related studies in India (Kumar et al. 2020; Nilawar and Waikar 2019; Venkatesh and Ramesh 2018).

3.1.2 Ranking of GCMs

3.1.2.1 Observed precipitation and temperature dataset

This study uses high resolution gridded daily rainfall and temperature dataset from the IMD. Daily precipitation data from the year 1901 at a resolution of 0.25° longitude \times 0.25° latitude is made available by IMD. This dataset is generated by converting 6995 station-based observations into gridded datasets employing Shepard's interpolation technique (Pai et al. 2014). This dataset can represent the spatial rainfall distribution, such as scarce rainfall in the leeward side of the Western Ghats and intense rainfall regions in the orographic areas of the west coast.

3.1.2.2 GCM precipitation and temperature dataset

The study uses a statistically downscaled and bias-corrected CMIP5 dataset provided by the National Aeronautics Space Administration (NASA) Earth Exchange Global Daily Downscaled Projections (NEX-GDDP). It includes historical and future climate projections (RCPs 4.5 and 8.5) of precipitation and temperature at high spatial (25 km^2 grid-scale) and temporal (daily) resolutions from 21 GCMs. It is generated using Bias-Correction Spatial Disaggregation (BCSD) method (Wood et al. 2004) using the Global Meteorological Forcing Dataset (GMFD) provided by the Terrestrial Hydrology Research Group at Princeton University (Jain et al. 2019). This data can be accessed from NASA Centre for Climate Simulation (NCCS) portal (<https://portal.nccs.nasa.gov/datashare/NEXGDDP/>). The list of 21 GCMs with the country of their origin is given in Table 3.1. This dataset has been utilized in many research papers around the world (Bao and Wen 2017; Jain et al. 2019; Singh and Xiaosheng 2019). It is considered as the highest resolution and most accurate climate data based on CMIP5 in India (Singh et al. 2019). The high resolution of NEX-GDDP not only provides tidings at finer scales but also incorporates local topography effects

which influence the local extremes of rainfall events. A study by Jain et al. (2019) evaluated and compared the performance of the NEX-GDDP dataset with CMIP5 and CORDEX datasets in India. They found that the NEX-GDDP data could realistically capture the precipitation and temperature variability in India and recommended it for future climate impact studies.

Bias-corrected daily projections of precipitation, maximum temperature, and minimum temperature for South Asia developed by Mishra et al. (2020) using outputs from 13 CMIP6 GCMs are used in the study. This dataset is bias-corrected using Empirical Quantile Mapping (EQM) for the historical (1951–2014) and projected (2015–2100) period. The dataset contains bias corrected projections for the four scenarios (SSP126, SSP245, SSP370, SSP585). This bias-corrected dataset is technically validated against the observations for both mean and extremes (Mishra et al. 2020). The spatial resolution of bias corrected projections is 0.25 deg. The list of these 13 GCMs with the country of their origin is given in Table 3.2. Hereafter these GCMs are collectively referred to as the CMIP6 dataset.

3.1.3 Creation of MMEs

The daily gridded rainfall and temperature dataset from the IMD (mentioned in section 3.1.2.1) was used in the study as the reference/observation dataset. The MMEs of precipitation and temperature of NEX-GDDP and CMIP6 data (mentioned in 3.1.2.2) are created in this study.

3.1.4 LULC prediction

Atmospherically corrected surface reflectance data from the Landsat 8 Operation Land Imager (OLI) sensors, Landsat 7 Enhanced Thematic Mapper Plus (ETM+) sensor and Landsat 5 Thematic Mapper (TM) sensor images for the years 1990, 2000, 2010 and 2020 are used in the study. The reflectance information of Blue, Green, Red, Near Infrared (NIR), Shortwave Infrared 1 (SWIR1) and Shortwave Infrared 2 (SWIR2) bands along with the ALOS World 3D (AW3D30) dataset, which is a global digital surface model (DSM) was used. Both the datasets have a spatial resolution of 30 m. The reflectance values of various bands of Landsat and DEM information were used for creating auxiliary data for classification.

Table 3.1 Twenty-one CMIP5 models included in NEX-GDDP dataset

Model name	Country	Latitude resolution (degree)	Longitude resolution (degree)	Description	Institution/Agency
ACCESS1-0	Australia	1.25	1.875	Australian Community Climate and Earth System Simulator, version 1.0	Commonwealth Scientific and Industrial Research Organisation (CSIRO) and Bureau of Meteorology (BoM)
BNU-ESM	China	2.8	2.8	Beijing Normal University Earth System Model	College of Global Change and Earth System Science and Beijing Normal University
CCSM4	United States	0.94	1.25	Community Climate System Model (CCSM), version 4	University Corporation for Atmospheric Research
CESM1-BGC	United States	0.94	1.25	Community Earth System Model, version 1–Biogeochemistry	National Science Foundation, Department of Energy, National Centre for Atmospheric Research
CNRM-CM5	France	1.4	1.4	Centre National de Recherches Météorologiques Coupled Global Climate Model, version 5	Centre National de Recherches Meteorologiques / Centre Europeen de Recherche et Formation Avancees en Calcul Scientifique

CSIRO-Mk3-6-0	Australia	1.8	1.8	Commonwealth Scientific and Industrial Research Organisation Mark 3.6.0	Queensland Climate Change Centre of Excellence and the Commonwealth Scientific and Industrial Research Organisation (CSIRO)
CanESM2	Canada	2.8	2.8	Second generation Canadian Earth System Model	Canadian Center for Climate Modelling and Analysis
GFDL-CM3	United States	2.0	2.5	Geophysical Fluid Dynamics Laboratory- Climate Model version 3	Geophysical Fluid Dynamics Laboratory
GFDL-ESM2G	United States	2.0	2.5	Geophysical Fluid Dynamics Laboratory Earth System Model with (GOLD) component	Geophysical Fluid Dynamics Laboratory
GFDL-ESM2M	United States	2.0	2.5	Geophysical Fluid Dynamics Laboratory Earth System Model with Modular Ocean Model (MOM), version 4 component	Geophysical Fluid Dynamics Laboratory

IPSL-CM5A-LR	France	1.8	3.75	L’Institut Pierre-Simon Laplace Coupled Model, version 5A, low resolution	Institut Pierre-Simon Laplace
IPSL-CM5A-MR	France	1.25	2.5	L’Institut Pierre-Simon Laplace Coupled Model, version 5A, mid resolution	Institut Pierre-Simon Laplace
MIROC-ESM	Japan	2.8	2.8	Model for Interdisciplinary Research on Climate, Earth System Model	Japan Agency for Marine-Earth Science and Technology, Atmosphere and Ocean Research Institute (The University of Tokyo), and National Institute for Environmental Studies
MIROC-ESM-CHEM	Japan	2.8	2.8	Model for Interdisciplinary Research on Climate, Earth System Model, Chemistry Coupled	Japan Agency for Marine-Earth Science and Technology, Atmosphere and Ocean Research Institute (The University of Tokyo), and National Institute for Environmental Studies
MIROC5	Japan	1.4	1.4	Model for Interdisciplinary Research on Climate, version 5	Japan Agency for Marine-Earth Science and Technology, Atmosphere and Ocean Research Institute (The University of

					Tokyo), and National Institute for Environmental Studies
MPI-ESM-LR	Germany	1.9	1.9	Max Planck Institute Earth System Model, low resolution	Max Planck Institute for Meteorology
MPI-ESM-MR	Germany	1.9	1.9	Max Planck Institute Earth System Model, medium resolution	Max Planck Institute for Meteorology
MRI-CGCM3	Japan	1.1	1.1	Meteorological Research Institute Coupled Atmosphere–Ocean General Circulation Model, version 3	Meteorological Research Institute
NorESM1-M	Norway	1.9	2.5	Norwegian Earth System Model 1-M	Norwegian Climate Centre
BCC-CSM1.1	China	2.8	2.8	Beijing Climate Center, Climate System Model, version 1.1	Beijing Climate Centre
INM-CM4	Russia	1.5	2.0	Institute of Numerical Mathematics Coupled Model, version 4	Russian Institute of Numerical Mathematics

Table 3.2 Thirteen CMIP6 models considered in the study

Model name	Country	Latitude resolution (degree)	Longitude resolution (degree)	Description	Institution/Agency
ACCESS-CM2	Australia	1.25	1.875	Australian Community Climate and Earth System Simulator Climate Model Version 2	Commonwealth Scientific and Industrial Research Organisation (CSIRO), Australian Research Council Centre of Excellence for Climate System Science (ARCCSS), and Bureau of Meteorology
ACCESS-ESM1-5	Australia	1.25	1.875	Australian Community Climate and Earth System Simulator Earth System Model Version 1.5	Commonwealth Scientific and Industrial Research Organisation (CSIRO)
BCC-CSM2-MR	China	1.1215	1.125		Beijing Climate Centre
CanESM5	Canada	2.7906	2.8125	Fifth generation Canadian Earth System Model	Canadian Centre for Climate Modelling and Analysis
EC-Earth3	Europe	0.7018	0.703125	EC-Earth Earth System Model Version 3	EC-Earth Consortium

EC-Earth3-Veg	Europe	0.7018	0.703125	EC-Earth Earth System Model Version 3 with Dynamic vegetation component	EC-Earth Consortium
INM-CM4-8	Russia	1.5	2	Institute of Numerical Mathematics Coupled Model, version 4.8	Russian Institute of Numerical Mathematics, Russian Academy of Science
INM-CM5-0	Russia	1.5	2	Institute of Numerical Mathematics Coupled Model, version 5	Russian Institute of Numerical Mathematics, Russian Academy of Science
MPI-ESM1-2-HR	Germany	0.9351	0.9375	Max Planck Institute for Meteorology Earth System Model version 1.2 higher resolution	Max Planck Institute for Meteorology
MPI-ESM1-2-LR	Germany	1.8653	1.875	Max Planck Institute for Meteorology Earth System Model version 1.2 low resolution	Max Planck Institute for Meteorology
MRI-ESM2-0	Japan	1.1215	1.125	Meteorological Research Institute Earth System Model Version 2.0	Meteorological Research Institute
NorESM2-LM	Norway	1.8947	2.5	Norwegian Earth System Model version 2 with low resolution atmosphere/land and medium resolution ocean/sea ice	Norwegian Climate Consortium (NCC)

NorESM2-MM	Norway	0.9424	1.25	Norwegian Earth System Model version 2 with medium resolution of both atmosphere/land and ocean/sea ice	Norwegian Climate Consortium (NCC)
------------	--------	--------	------	---	------------------------------------

3.1.5 Hydrological modelling

Table 3.3 shows the data products used as input to SWAT.

Table 3.3 Data Products used as input for SWAT model

Data	Time period	Source
Historical LULC maps	1990, 2000, 2010 and 2020	Landsat 5, 7 and 8 Path/Row: 145/51
Future LULC maps	2050, 2075 and 2100	Projected maps from TerrSet
DEM (Slope and Elevation)	-	ALOS World 3D-Japan Aerospace Exploration Agency (JAXA)
Soil	-	National Bureau of Soil Survey and Land Use Planning
Historical Meteorological Data	1990-2020	Indian Meteorological Department
Future Meteorological Data	2020-2100	MME's of NEX-GDDP and CMIP6 dataset

3.2 METHODOLOGY

The overall methodology for the proposed study is given in Figure 3.1. The methodology has three parts: a) preparation and analysis of climate data, b) land use land cover prediction, and c) hydrological modelling to analyse the impacts of LULC and climate change on streamflow.

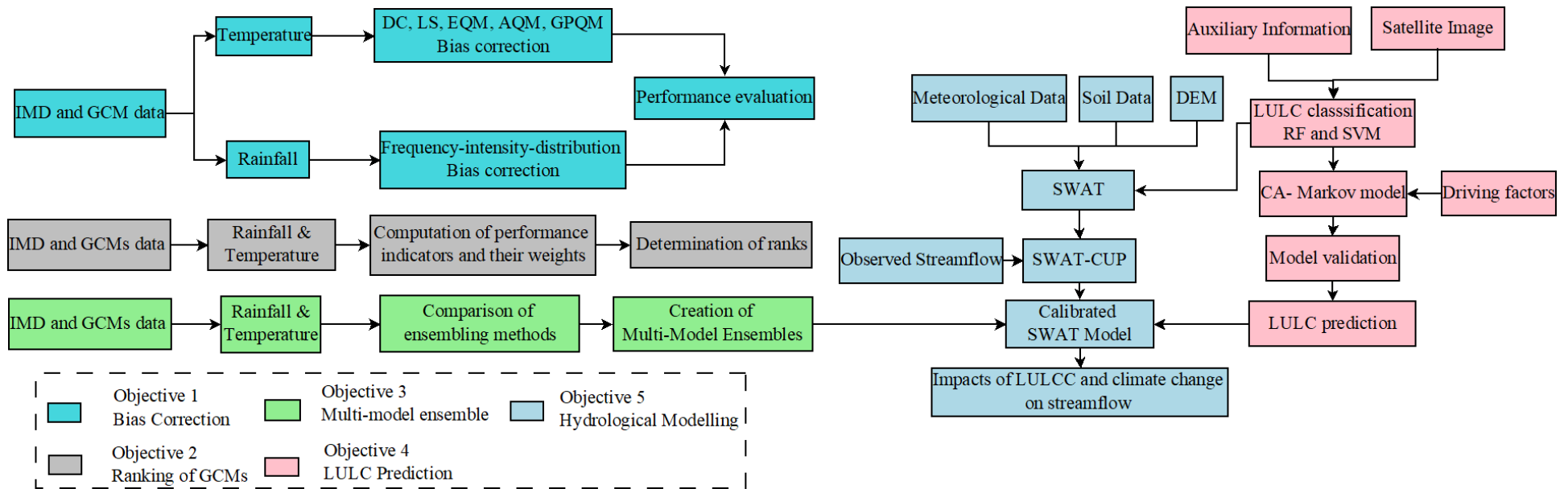


Figure 3.1 Methodology

3.2.1 Bias correction

3.2.1.1 Bias correction of rainfall

Several BC methods have been developed in the past in order to improve the RCM/GCM simulations. These include correcting the mean, both mean and variance, or mean and variance, along with quantile value adjustment (Maraun 2016; Teutschbein and Seibert 2012). Mudbhatkal and Mahesha (2018) did an evaluation of the performance of Linear Scaling (LS), Delta Change (DC) correction, Local Intensity (LI) Scaling, Power Transform (PT), and the Distribution Mapping (DM) methods. This study used GCM of CMIP5 downscaled by RCA4 over India's Western Ghats basins and found that the DC method performed the best. In light of this study, the authors initially performed BC of GCM using these methods but could not notice any improvement in the GCM simulated precipitation. This might be because of the fact that not only the study area but also the model under consideration affects the performance of the BC method. Therefore, to improve the simulations of our GCM, a new methodology combining different existing BC schemes targeting different characteristics of rainfall was adopted in this study. The steps for the same are as follows.

3.2.1.1.1 Data preprocessing

The gridded precipitation data from the GCM is obtained with a spatial resolution of about $0.1875^{\circ} \times 0.1875^{\circ}$. For the comparison of GCM data and station data, the GCM data was interpolated to station coordinates. Linear interpolation was used for this purpose, as few studies stated that it performed better than other methods like bilinear and cubic interpolations (Singh et al. 2019; Singh and Xiaosheng 2019).

3.2.1.1.2 Frequency correction

It is widely reported that RCMs/GCMs tend to simulate too frequent low intensity precipitation events interrupting longer dry spells (Berg et al. 2012; Olsson et al. 2015). This leads to an overestimation of wet days when compared to observed precipitation. This is often termed as the "drizzle effect". It is necessary to eliminate the drizzle effect

in original GCM/RCM simulations (Teutschbein and Seibert 2012). Thresholding is a common occurrence bias adjustment method which can handle the drizzle effect (Ines and Hansen 2006; Vrac et al. 2016). The simplest form of thresholding sets values in simulations below a certain threshold to zero. In this study, an advanced method of thresholding which is used by Switanek et al. (2017) and Velde et al. (2021) is adopted, in which the number of days below the threshold in observed and simulated time series is assumed to be the same.

The methodology adopted for the thresholding method of occurrence/frequency BC is as follows. For this, a day is considered as wet if the simulated precipitation is above 0.1 mm. First, the frequency of dry days is calculated for both simulated and observed data for every month. Then the difference in these frequencies (Δn), of observed and simulated data for each month is computed. The simulated wet days of each month are sorted in increasing order of precipitation amount, and the lowest Δn days of simulation data are set to 0. This monthly approach ensures that the realistic temporal structure is retained.

3.2.1.1.3 Intensity correction

Now that the frequency of wet days is corrected, the precipitation amount is to be corrected. For this, a method which corrects the precipitation intensity and systematic errors in simulated precipitation data as proposed by Mahmood and Babel (2013) is used. A correction factor is calculated for each month and is multiplied by simulated data to get the corrected precipitation amount. Equation 3.1 describes the process.

$$P_{corr} = P_{sim} \times \frac{\overline{P_{obs}}}{\overline{P_{cont}}} \quad (3.1)$$

where P_{corr} is the corrected daily time series of precipitation. P_{sim} represents the daily GCM simulated precipitation data. $\overline{P_{cont}}$ is the long- term mean monthly values of precipitation for the control period simulated by GCM. $\overline{P_{obs}}$ represents the long-term mean monthly observed values of precipitation.

3.2.1.1.4 Distribution mapping

The distribution mapping method corrects the distribution function of simulated GCM data based on the distribution of observed data rather than merely adjusting the mean and variance of model output (Wang and Chen 2014). This is achieved through the help of transfer functions. Many studies state that distribution mapping performed the best among other BC methods (Teutschbein and Seibert 2012; Yan et al. 2020).

The multiplicative version of distribution mapping, known as equiratio Cumulative Distribution Function (CDF) matching as proposed by Wang and Chen (2014), is used in this study for precipitation correction. Mathematically, it can be written as

$$P_i^{fc} = P_i^{fs} \times \frac{F_{P^{ho}}^{-1}(F_{P^{fs}}(P^{fs}))}{F_{P^{hs}}^{-1}(F_{P^{fs}}(P^{fs}))} \quad (3.2)$$

Where P^{fc} and P^{fs} are the corrected and raw daily future simulation. P^{hs} and P^{ho} are historical simulated and observed precipitation. F^{-1} and F indicate CDF and inverse CDF, respectively. To ensure the consistency of time series, many researchers have suggested the usage of the moving window technique (Smitha et al. 2018; Themeßl et al. 2011). Here, a 61-day moving window was selected as opted by Themeßl et al. (2011). Thus, 61 days of each year were used for calculating the empirical CDF and correction of each day. The input for distribution mapping was already corrected for frequency and intensity, as mentioned above. This distribution correction is applied only on days with precipitation greater than 0.1 mm.

3.2.1.1.5 Performance evaluation

Split-sample or cross-validation approach is commonly used to validate the results of BC methods (Maurer and Pierce 2014; Switanek et al. 2017; Wang and Chen 2014). For this, the BC is calibrated from 1971 to 2000 and is validated for 2001 to 2014. The performance evaluation in validation period was conducted by calculating the Nash–Sutcliffe efficiency (NSE), coefficient of determination (R^2), the root-mean-square error (RMSE), the mean absolute error (MAE), the percentage bias (PBIAS) and the correlation coefficient (r) which are extensively used by many researchers (Ayugi et al. 2020; Bhatti et al. 2016). Taylor diagram (Taylor 2001), which summarises the

performance of corrected and uncorrected monthly precipitation data in terms of root mean square deviation (RMSD), correlation coefficient (r) and standard deviation (SD) was used. Complementarily, a quantile-quantile plot (Q-Q plot) of daily precipitation was used to compare the uncorrected and bias-corrected rainfall against observations during the validation period.

3.2.1.2 Bias correction of temperature

Six BC methods were used to adjust the biases in maximum and minimum temperature simulated by the GCM over the Netravati basin. These BC methods are Delta Change (DC), Linear Scaling (LS), Empirical Quantile Mapping (EQM) method, Adjusted Quantile Mapping (AQM) method, Gamma-Pareto Quantile Mapping (GPQM) method and Quantile Delta Mapping (QDM). These methods cover the major types of existing BC methods. These bias correction methods can be classified into scaling-based and distributional-based methods. The scaling-based methods use an additive or multiplicative scaling factors (e.g., delta correction and linear scaling) to adjust the GCM simulations. However, distributional-based methods use quantile mapping techniques that modify empirically (e.g., EQM and AQM) or parametrically (e.g., GPQM) some features of the probability distribution function (PDF). All these methods try to improve the model agreement with the observations. All the BC methods except QDM were implemented on the minimum and maximum temperature values at each grid point using MeteoLab, which is an open-source MATLAB toolbox developed by Santander Meteorology Group. A trend preserving method (QDM) is also used to compare its ability in correcting the biases in the GCM data. All the BC methods are executed on the daily data independently for each grid cell in the study area. Bilinear interpolation is used to bring the GCM data to the grids of observed data. A brief description of each BC method is provided in the following section. All the calculations have been carried out independently for each grid cell and the results for one representative grid (12.5°N,75.5°E) in the basin are shown to simplify the presentation.

3.2.1.2.1 Delta correction method

The DC method is the simplest bias correction method. It is performed by adding the mean change signal to the observations. It uses observations as a basis and, hence, is

stable and robust enough to produce future climate variable dynamics similar to current conditions (Teutschbein and Seibert 2012). This method resembles the case of $g=1$ and $f=0$ in Amengual et al. (2012). Where 'g' is a factor that modulates the variation in the mean delta change, while 'f' calibrates the change in variability and shape expressed by the individual delta changes in the quantiles. Mathematically, the method is expressed as follows (Teutschbein and Seibert 2012):

$$T_{Cont}^{BC}(i) = T_{obs}(i) \quad (3.3)$$

$$T_{scen}^{BC}(i) = T_{obs}(i) + \mu_m(T_{scen}(i)) - \mu_m(T_{cont}(i)) \quad (3.4)$$

Where, $T_{Cont}^{BC}(d)$ and $T_{scen}^{BC}(d)$ are bias corrected historical and future daily temperature

$T_{obs}(d)$ is observed daily temperature

$T_{scen}(d)$ and $T_{cont}(d)$ are daily future and historical simulated temperature

μ_m is the monthly mean value

3.2.1.2.2 Linear scaling method

The LS method is similar to delta correction. However, in this method, the difference in the mean of observations and the simulations is added to get the bias corrected temperature values. More information on the method can be found in Lenderink et al. (2007) and Teutschbein and Seibert (2012). The method can be expressed as follows:

$$T_{cont}^{BC}(d) = T_{cont}(i) + \mu_m(T_{obs}(i)) - \mu_m(T_{cont}(i)) \quad (3.5)$$

$$T_{scen}^{BC}(d) = T_{scen}(i) + \mu_m(T_{obs}(i)) - \mu_m(T_{cont}(i)) \quad (3.6)$$

3.2.1.2.3 Empirical Quantile Mapping Method

The EQM method corrects the distribution of simulated data in order to match the distribution of the observation dataset (Déqué 2007). This is done with the help of the transfer function (TF). In MeteoLab, the method is implemented by following Déqué et al. (2017). That is, we obtain a TF for 99 percentiles and linearly interpolate between each of them. The new extremes are extrapolated. This method is equivalent to $f=g=1$ in Amengual et al. (2012). In EQM, the empirical non-parametric cumulative

distribution function (CDF) is used without any assumption on the temperature distribution. Mathematically, the EQM is performed using the following equation:

$$T_{BC} = F_{obs}^{-1}(F_{sim}(x)) \quad (3.7)$$

Where, T_{BC} is the bias corrected temperature simulation

F_{sim} is the CDF of simulated data

F_{obs}^{-1} is the inverse of the CDF of the observed data.

x is the simulated temperature value by the model

3.2.1.2.4 Gamma-Pareto quantile mapping method

The combination of a gamma distribution and a Generalised Pareto distribution (GPD) in quantile mapping is referred to as Gamma-Pareto quantile mapping (Gutjahr and Heinemann 2013). A better correction of higher percentiles is expected by using this method. This method was developed for precipitation. Hence, another version of the method available for gaussian variables like temperature is used here. In this case, a normal distribution is fitted for values between the 5th and 95th percentiles while the upper and lower 5% are assumed to follow the GPD. Thus, the function F in equation 5 is replaced by a combination of normal and GPD distribution. This can be mathematically expressed as follows:

$$T_{BC} = F_{obs,normal}^{-1} \left(F_{sim,normal}(x) \right) , \text{ if } x < 95^{\text{th}} \text{ percentile or } x > 5^{\text{th}} \text{ percentile} \quad (3.8)$$

$$T_{BC} = F_{obs,GPD}^{-1} \left(F_{sim,GPD}(x) \right) , \text{ if } x \geq 95^{\text{th}} \text{ percentile or } x \leq 5^{\text{th}} \text{ percentile} \quad (3.9)$$

Where, T_{BC} is the bias corrected temperature simulation

$F_{sim,normal}$ and $F_{sim,GPD}$ are the CDFs for simulated data assuming normal distribution and GPD distribution respectively

$F_{obs,normal}^{-1}$ and $F_{obs,GPD}^{-1}$ are the inverse of the CDF of the observed data assuming normal distribution and GPD distribution respectively

x is the simulated temperature value by the model

3.2.1.2.5 Adjusted quantile mapping method

The AQM method calculates the changes of each quantile in the CDFs of daily simulated data between the control or historical period and the future verification period. These changes are rescheduled based on the CDF of observed data for the same control period. The new CDFs are obtained to transmit the climate change signal by adding these observations in each quantile (Ezéchiel et al. 2016). More about AQM method can be found in Amengual et al. (2012). The mathematical translation of the method is as follows:

$$T_{BC}(i) = T_{obs}(i) + g\bar{\Delta} + f\hat{\Delta}_i \quad (3.10)$$

$$\Delta_i = S_{cont}(i) - S_{scen}(i) \quad (3.11)$$

$$\hat{\Delta}_i = \Delta_i - \bar{\Delta} \quad (3.12)$$

Where, $T_{BC}(i)$ are the corrected values

$T_{obs}(i)$ are the observed values

$S_{cont}(i)$ and $S_{scen}(i)$ are simulations for the control period and scenario or future period of the corresponding CDFs

$\bar{\Delta}$ is the mean of Δ_i

f is the ratio between the mean of observations and simulations in the control period

g is the ratio between standard deviations of observations and simulations in the control period

3.2.1.2.6 Quantile delta mapping

QDM was first proposed by Li et al. (2010), to preserve the trends in climate simulations and to take some non-stationarity into account. Cannon et al. (2015) made a comparison of QDM with other quantile mapping methods and found that QDM outperformed other methods in the case of preservation of trends. An additive version of this method is used in this paper, and it can be mathematically written as follows:

$$x_i^{fBC} = x_i^{fs} + F_{X^{ho}}^{-1} \left(F_{X^{fs}}(x_i^{fs}) \right) - F_{X^{hs}}^{-1} \left(F_{X^{fs}}(x_i^{fs}) \right) \quad (3.13)$$

Where, $F_{X^{fs}}$ the CDF of the simulated future temperature data

$F_{X^{ho}}^{-1}$ is the inverse CDF of the historical observed temperature data

$F_{X^{hs}}^{-1}$ is the inverse CDF of the historical model simulated temperature data

x_i^{fs} is the daily future temperature data simulated by the GCM

x_i^{fBC} is the daily bias corrected future simulations

3.2.1.2.7 Moving window technique

Usually, the whole data is used to calibrate the models. It is also possible to correct each day of the year independently using the moving window technique, which is used by Sahoo et al. (2019), Smitha et al. (2018), and Teutschbein and Seibert (2012). In this technique, a moving window centred on each day of the year is used to calibrate the correction. Hence, there would be a correction function for each day of the year rather than a single correction function for the whole period. The moving window was selected for the study after a trial-and-error procedure considering window sizes ranging from 11 to 91 days. The moving window technique is not used in GPQM, as it did not have enough data to fit the Generalised Pareto distribution for the extremes. Hence, this moving window was used for four bias correction methods except for GPQM. Table 3.4 shows the selection criteria for choosing the size of the moving window for QDM method. Similar results were obtained for other bias correction methods as well. Table 3.4 reveals that when the moving window size is 15 days, the performance of the bias correction is at its maximum. Hence, a moving window of size 15 was selected.

Table 3.4 Performance of QDM based on the size of the moving window used

Size of moving window (days)	NSE	MAE	r	PBIAS
Maximum temperature				
11	0.51	1.44	0.78	1.72
15	0.53	1.35	0.79	1.14
21	0.52	1.41	0.78	1.80
31	0.50	1.45	0.78	2.10
61	0.49	1.46	0.78	2.20
91	0.48	1.47	0.77	2.50
Minimum temperature				
11	0.41	1.31	0.69	-3.76
15	0.43	1.20	0.72	-3.75
21	0.41	1.30	0.69	-3.76
31	0.34	1.31	0.67	-3.77
61	0.31	1.31	0.65	-3.78
91	0.27	1.34	0.65	-3.76

3.2.1.2.8 Bias correction implementation and performance assessment

The two-sample cross-validation approach was used for the performance evaluation of each bias correction method (Maurer and Pierce 2014; Switanek et al. 2017; Wang and Chen 2014). The observational and simulated values of maximum and minimum temperature are divided into a 44-year calibration period (1951–1994) and a 20-years validation period (1994–2014). These periods were selected based on the observed and simulated datasets available. For the performance evaluation BC methods, the Nash–Sutcliffe efficiency (NSE), the Root-Mean Square Error (RMSE) or Root-Mean Square Deviation (RMSD), the Mean Absolute Error (MAE), the Percentage BIAS (PBIAS) and the correlation coefficient (r) were calculated for each BC method in the validation period (1994–2014). These performance indicators are widely used by many

researchers (Bhatti et al. 2016; Mendez et al. 2020). The mathematical formula of these indicators are as follows:

$$RMSE = \sqrt{\frac{1}{T} \sum_{i=1}^T (M_i - O_i)^2} \quad (3.14)$$

$$r = \frac{\sum_{i=1}^T (O_i - \bar{O})(M_i - \bar{M})}{(T-1)\sigma_o\sigma_m} \quad (3.15)$$

$$NSE = 1 - \frac{\sum_{i=1}^T (O_i - M_i)^2}{\sum_{i=1}^T (O_i - \bar{O})^2} \quad (3.16)$$

$$PBIAS = \frac{\sum_{i=1}^T (M_i - O_i)}{\sum_{i=1}^T O_i} \times 100 \quad (3.17)$$

$$MAE = \frac{\sum_{i=1}^T |M_i - O_i|}{T} \quad (3.18)$$

Where, M_i and O_i are the modelled/simulated and observed values, respectively.

T is the number of datasets.

\bar{O} and \bar{M} are averages of observed and simulated values

σ_o and σ_m are the standard deviation of GCM and observed data

The values of RMSE/RMSD range from 0 to $+\infty$. It is used to check the accuracy of modelled values when compared with observed values. An RMSE value close to 0 indicates a higher estimation accuracy. The correlation coefficient indicates the strength of the linear relationship between the GCM simulated and observed values. The r-value ranges from -1 to 1, and a value near 1.0 indicates a perfect positive correlation. The values of NSE range from $-\infty$ to 1 (Nash and Sutcliffe 1970). A model which simulates perfectly gives an NSE value of 1.0. A value of NSE less than zero ($NSE < 0$) indicates that the observed mean is a better predictor than the simulations. The MAE value varies between 0 to $+\infty$ and gives the absolute measure of bias. An MAE value close to 0 indicates an unbiased prediction. On the other hand, the PBIAS calculates the relative volume difference between predicted and observed data. A positive value indicates overestimation, whereas a negative value of PBIAS indicates underestimation. Taylor diagram, which summarises the performance of each BC method in terms of RMSD, r

and standard deviation (SD) is also used. Further, quantile-quantile plots (Q-Q plots) of daily temperature were plotted to compare the uncorrected (UC) and bias-corrected simulated values against observations during the validation period. Q-Q plots provide a useful comparison of simulated and observed CDFs. Daily temperature values are plotted for a year in the validation period to understand the daily and seasonal variation of observed and predicted temperature values. Results for one representative grid in the basin are given in Chapter 4.

3.2.2 Ranking of GCMs

The study is performed over the Netravati basin for a historical period from 1950 to 2005. The historical GCM data is compared with observed gridded data for this period. The GCMs which perform well in the historical period are expected to perform well in the future (Maximo et al. 2008). Performance indicators are used to measure the performance of GCMs. These performance indicators are then normalised and the weightage for each indicator is calculated. Then, using Multi-Criteria Decision Making (MCDM) techniques, the best GCMs are selected. Finally, a group decision-making procedure is applied to integrate the results of MCDM methods in order to create a single group preference. A schematic representation of the methodology followed in the study is given in Figure 3.2. The detailed methodology is as follows:

3.2.2.1 Performance indicators for evaluating GCMs

To ascertain the performance or simulating ability of GCMs, evaluation criteria or indicators are required. There are different ways to choose the indicators (Perkins et al. 2007). The indicators for this study were selected category-wise, i.e., one for error, one for correlation and one for skill score. The selected indicators were root-mean-square error (RMSE), skill score (SS), and correlation coefficient (r), respectively. SS is a robust measure of the relative similarity between the observed and simulated Probability Density Functions (PDFs) (Vafaei et al. 2018). The skill score varies between 0 and 1. Mathematically it can be represented as below

$$SS = \frac{1}{T} \sum_{i=1}^{nb} \min(f_m, f_o) \quad (3.19)$$

where: T is the number of datasets.

n_b is the number of bins used to calculate the PDF of the data.

f_m and f_o are the frequencies of values in the given bin from GCM and observed data.

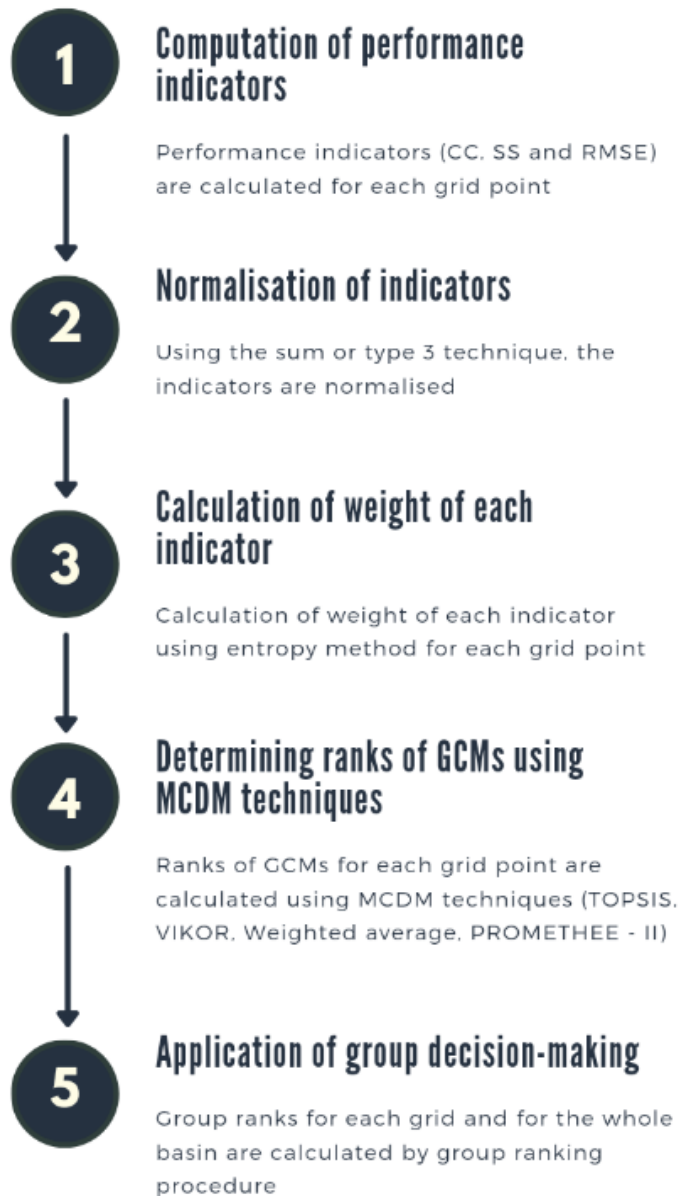


Figure 3.2 Methodology followed for ranking of GCMs

The temporal distribution of daily simulations of GCMs and gridded observed datasets does not coincide. Consequently, the GCMs are expected to simulate the monthly and seasonal values well. Therefore, the daily simulations of GCMs at each grid is

converted to a monthly scale to evaluate the RMSE and r of each GCM based on observed monthly data. However, the SS is calculated based on daily rainfall values, as suggested by Pomerol and Romero (2012), Raju and Kumar (2014a) and Vafaei et al. (2016). The six bins (nb = 6) for calculation of SS of rainfall are decided based on the daily rainfall classification of IMD. The classification by IMD is as follows: no rain (0), very light rain (0.1 mm – 2.4 mm), light rain (2.5 mm – 7.5 mm), moderate rain (7.6 mm – 35.5 mm), rather heavy rain (35.6 mm – 64.4 mm), heavy rain (64.5 mm – 124.4 mm), very heavy rain (124.5 mm – 244.4 mm) and exceptionally heavy rain (≥ 244.5 mm) (Bhatla et al. 2019). An appropriate bin width of 5°C is selected for temperature based on the range of values of minimum and maximum temperature. The bins for minimum temperature are: < 10°C, 10°C - 15°C, 15°C - 20°C, 20°C - 25°C and > 25°C. Similarly, the bins for maximum temperature are: <20°C, 20°C - 25°C, 25°C - 30°C, 30°C - 35°C and >35°C.

3.2.2.2 Normalization and weight computation of indicators

Normalization techniques are used to transform various non-commensurable performance indicators measured on different scales into a comparable scale (Pomerol and Romero 2012; Raju and Kumar 2014a). There are various normalization techniques like max, max-min, sum, vector and logarithmic normalization. More information about the normalization techniques can be found in Li et al. (2011). A simple and popular normalization technique known as the sum or type 3 normalization is used for the present study (Raju and Kumar 2014a; Sreelatha and Anand Raj 2019). The mathematical formula of normalised value (k_{aj}) is as follows:

$$k_{aj} = \frac{K_j(a)}{\sum_{a=1}^n K_j(a)} \quad (3.20)$$

where a is the index for GCM ($1 \leq a \leq 21$ or $1 \leq a \leq 13$);

j is the index of indicator ($1 \leq j \leq 3$);

$K_j(a)$ is the magnitude of indicator j for GCM a ;

n represents the number of GCMs ($n=21$ or $n=13$).

There are several methods for finding the weights of indicators (Raju and Kumar 2018). They can be subjective fixed weight methods or objective fixed weight methods. In the present study, instead of assuming some proportion or equal weights, an objective fixed weight method, known as the entropy method is used for determination of weights. This can match the results more with the facts and can eliminate man-made biases (Brans et al. 1986; Raju and Nandagiri 2017). The methodology followed for the determination of weights is as follows:

$$En_j = -\frac{1}{\ln(n)} \sum_{a=1}^n k_{aj} \ln(k_{aj}) \quad (3.21)$$

$$Dd_j = 1 - En_j \quad (3.22)$$

$$r_j = \frac{Dd_j}{\sum_{j=1}^J Dd_j} \quad (3.22)$$

where En_j is entropy for each indicator j ;

Dd_j is the degree of diversification;

r_j is the normalised weight of indicators;

J represents the number of performance indicators.

The weights thus obtained are subsequently used in MCDM computations as explained below.

3.2.2.3 Multicriteria decision-making techniques

MCDM techniques help in determining the most feasible or best solution according to established criteria or indicators (Opricovic and Tzeng 2004). There are many MCDM techniques which can be used for ranking the GCMs. More details about these techniques can be found in Raju and Kumar (2014b). However, in the present study, four popular MCDM techniques, namely VIKOR, TOPSIS, weighted average and PROMETHEE-2 are used. More about each of these methods is discussed below.

3.2.2.3.1 Weighted average

The weighted average technique is a simple and easy method for determining the ranks of GCMs according to their performance. It is superior to the simple average or arithmetic mean technique. It uses the relative importance of criteria or performance indicators while calculating the ranks of GCMs. The methodology followed is given below.

Weighted normalised value (V_{aj}) is calculated as:

$$V_{aj} = r_j k_{aj} \quad (3.23)$$

Utility value (V_a) of each GCM a is calculated as:

$$V_a = \sum_1^J V_{aj} \quad (3.24)$$

where J represents the number of performance indicators ($J = 3$). A higher value of V_a indicates a better GCM.

3.2.2.3.2 VIKOR

The VIKOR method, also known as the compromise ranking method, was developed by S. Opricovic (Opricovic 1998). This method decides the compromise solution for the conflicting attributes among the various alternatives. Each alternative is evaluated according to the criteria and the degree of “closeness to the ideal” is compared (Opricovic 1998). More about the method can be found in Opricovic and Tzeng (2004), Opricovic (1998) and Chatterjee and Chakraborty (2016). Following are the steps used for ranking using the VIKOR method. First, the weighted normalised matrix is calculated using equation 3.24. Then utility measure or overall benefit (S_a) and regret measure or maximum individual deviation (R_a) are calculated as follows:

$$S_a = \sum_{a=1}^n \frac{V_{ajmax} - V_{aj}}{V_{ajmax} - V_{ajmin}} \quad (\text{for positive attributes}) \quad (3.25)$$

$$S_a = \sum_{a=1}^n \frac{V_{aj} - V_{ajmin}}{V_{ajmax} - V_{ajmin}} \quad (\text{for negative attributes}) \quad (3.26)$$

$$R_a = \text{Max of } \left[\frac{V_{aj_{max}} - V_{aj}}{V_{aj_{max}} - V_{aj_{min}}} \right] a \quad (\text{for positive attributes}) \quad (3.27)$$

$$R_a = \text{Min of } \left[\frac{V_{aj_{max}} - V_{aj}}{V_{aj_{max}} - V_{aj_{min}}} \right] a \quad (\text{for positive attributes}) \quad (3.28)$$

Then the value of Q_a was computed with the following relation:

$$Q_a = v \left[\frac{S_a - S_{a_{min}}}{S_{aj_{max}} - S_{aj_{min}}} \right] + (1 - v) \left[\frac{R_a - R_{a_{min}}}{R_{aj_{max}} - R_{aj_{min}}} \right] \quad (3.29)$$

Where v is the balancing factor between group utility and individual regret. Here the magnitude of v is assumed as 0.5. However, v can range from 0 to 1. GCMs are ranked by sorting the values S , R and Q in decreasing order. A compromise solution and the results of the three ranking lists are decided based on two conditions, namely “acceptable advantage” and “acceptable stability in decision making”. More about the procedure can be found in Opricovic and Tzeng (2004).

3.2.2.3.3 TOPSIS

TOPSIS method was proposed by Hwang and Yoon (1981) to rank alternatives based on the distance from the ideal and anti-ideal solutions. The best choice must have the minimal distance from the former and maximal distance from the latter (Hwang and Yoon 1981; Yoon 1987). TOPSIS method is similar to VIKOR in considering the distances to ideal and anti-ideal solutions but does not take into account the relative importance of these distances (Opricovic and Tzeng 2004). The following steps are involved in ranking the GCMs by TOPSIS method (Hwang and Yoon 1981):

First, the ideal (V_j^*) and anti-ideal (V_j^{**}) value of each indicator is found from the normalised matrix. Then, the separation measures DS_a^+ from the ideal solution and DS_a^- from the anti-ideal solution are calculated using the following formulas.

$$DS_a^+ = \sqrt{\sum_{j=1}^J r_j (V_{aj} - V_j^*)^2} \quad (3.30)$$

$$DS_a^- = \sqrt{\sum_{j=1}^J r_j (V_{aj} - V_j^{**})^2} \quad (3.31)$$

Finally, the value of relative closeness CR_a is calculated. The higher value of relative closeness indicates that the GCM is better.

$$CR_a = \frac{DS_a^-}{DS_a^- + DS_a^+} \quad (3.32)$$

3.2.2.3.4 PROMETHEE-2

The PROMETHEE, which was developed in 1985 by Brans and Vincke (1985) has six different extensions. One of the six different extensions, known as PROMETHEE II, which uses complete ranking, was used in this study. The method is based on the concept of preference function (Pomerol and Romero 2012; Raju and Kumar 2018). The preference function depends on the chosen indicator function ($Pr_j(a,b)$) and the pairwise difference between two GCMs (a and b) for a given indicator (j). Out of six types of indicator functions, the usual indicator function was chosen for this study. Initially, the multi-indicator preference index (MIPI) is calculated. Then, outranking indices $\varphi^+(a)$ and $\varphi^-(a)$ are calculated. Finally, the net ranking ($\varphi(a)$) of each GCM is computed. A higher value of $\varphi(a)$ indicates suitable GCM. More about PROMETHEE-2 can be found in Brans et al. (1986). Mathematical expressions are given below.

$$\pi(a, b) = \frac{\sum_{j=1}^J r_j Pr_j(a,b)}{\sum_{j=1}^J r_j} \quad (3.33)$$

$$\varphi^+(a) = \frac{\sum_A \pi(a,b)}{n-1} \quad (3.34)$$

$$\varphi^-(a) = \frac{\sum_A \pi(b,a)}{n-1} \quad (3.35)$$

$$\varphi(a) = \varphi^+(a) - \varphi^-(a) \quad (3.36)$$

3.2.2.4 Group decision-making

To ascertain the similarity between ranks obtained from different MCDM techniques, the spearman rank correlation coefficient was calculated. Spearman correlation coefficient can measure the consistency in ranking pattern. It is calculated using the following formula

$$R = 1 - \frac{6 \sum_{a=1}^n e_a^2}{n(n^2-1)} \quad (3.37)$$

where e_a is the difference of ranks for the same GCM (a).

Group decision-making is a procedure of creating a single group preference by integrating the individual rankings given by various methods. In this study, the group rank for each grid is calculated by integrating the rankings given by 4 MCDM methods. Also, a final group rank for the whole basin is calculated from group ranks at each grid. The methodology followed is as follows.

First, the ranks are divided into two portions in descending order of ranks, namely the upper portion and the lower portion. The upper portion consists of the GCMs with rankings from 1 to X, where $X = n/2$ or $X = (n/2 + 1)$ respectively for even or odd number of GCMs. The GCMs with rankings from Y to n constitute the lower portion where $Y = X+1$. Later, the strength (ST_a) and weakness (WE_a) of each rank are calculated as given below.

$$ST_a = \sum_{k=1}^m \sum_z^X (X - z + 1) q_{az}^k \quad (3.38)$$

Where $q_{az}^k=1$, if GCM a is in the position z for the ranking technique k and 0 otherwise ($z=1, \dots, x$)

$$WE_a = \sum_{k=1}^m \sum_y^T (z - Y + 1) q_{az}^k \quad (3.39)$$

Where $q_{az}^k=1$, if GCM a is in the position z for the ranking technique k and 0 otherwise ($z=Y, \dots, n$)

Net strength of GCM a (NS_a) is calculated as given below:

$$NS_a = ST_a - WE_a \quad (3.40)$$

Suitable GCM gives a higher value of NS_a .

3.2.3 Creation of MMEs

There are many methods available for ensembling, like Bayesian approaches and ML approaches (Xu et al. 2018, 2020a). Six techniques were used for creating MMEs of P, Tmax and Tmin simulated by 21 NEX-GDDP and 13 CMIP6 GCMs in Netravati basin. These methods were mean, Multiple Linear Regression (MLR), SVM, Extra Tree Regressor (ETR), RF and long short-term memory (LSTM). These methods cover the major types of existing ML ensembling methods. These ensembling techniques can be

classified as simple statistical techniques (mean), regression models (i.e., SVM and MLR), ensemble learning models (i.e., ETR and RF), and deep learning time series model (i.e., multivariate LSTM). All these methods try to improve the GCM simulations with respect to the observation dataset in the historical time period. All the BC methods except LSTM were implemented for P, Tmin and Tmax using the scikit-learn library in Python (Pedregosa et al. 2011). The LSTM was implemented using Keras, which is one of the most popular deep learning libraries in Python (Chollet 2018). All the calculations have been carried out independently for each grid cell and the results for one representative grid in the basin is shown to simplify the presentation. More about data pre-processing and a brief description of each ensembling method is provided in the following sections.

3.2.3.1 Data Preparation

Each ensembling method was carried out at each grid point considering P, Tmax and Tmin separately. Bilinear interpolation was done in order to bring the GCM values to the corresponding observation grids in the basin. Ensemble mean was calculated by finding the mean of P, Tmax and Tmin simulated by all GCMs at each grid, respectively. The data was split into training and testing datasets for validation and comparison of each method of ensembling. The input to each ML model was preprocessed using Principal component analysis (PCA). More about PCA is described below.

3.2.3.2 Principal Component Analysis

Before applying any ML algorithm, it is vital to acquire only the relevant features in the training dataset. This way of reducing the feature space is termed as dimensionality reduction or feature selection (Jolliffe and Cadima 2016). In this study the features are the various GCMs in the ensemble. Ahmed et al. (2020) have mentioned that the choice of the number of the GCMs used in MME is a key decision in ensembling. In the present study, PCA was used for this purpose. It is a part of the exploratory data analysis in ML technique for predictive models (Hotelling 1933). It makes the model simple and efficient, which in turn reduces the run time of the model. PCA prevents overfitting and converts a group of correlated variables to uncorrelated variables through orthogonal

transformation (Ayar et al. 2016). A principal component (PC) is chosen such that it would describe most of the available variance (Benestad et al. 2017). Thus, it removes the risk of multicollinearity. In this study, the PCs of 21 GCMs of the NEX-GDDP dataset and 13 GCMs of downscaled CMIP6 dataset for each grid was calculated separately. The PC's which gave cumulative contribution rates greater than 95% were used as input to ML models.

3.2.3.3 Machine Learning Algorithms

MMEs were developed for P, Tmax and Tmin separately at each grid point in the basin using ML methods. The observed and simulated values of P, Tmax and Tmin were divided into a calibration period and validation period. The first 45-years (1951-1995) of overlapping observed and simulated data were used for calibrating the MMEs. The rest of the data were used for validating the MMEs. More about the methods adopted in the study are given in the following sections.

3.2.3.3.1 Multiple linear regression (MLR)

MLR is a common form of regression analysis. Multiple linear regression attempts to explain the relationship between one dependent variable and two or more independent variables by fitting a linear equation (Uyanik and Güler 2013). It has been widely used for climate studies for downscaling and impact analysis (Pang et al. 2017; Themeßl et al. 2011). In general, MLR can be mathematically written as:

$$y = \beta_0 + \beta_1 x_1 + \dots + \beta_n x_n + \varepsilon \quad (3.41)$$

Where, y is the dependent variable

x_i are independent variables

β_i are parameters

ε is the error

In this study, the ordinary linear least squares (LLS) regression which minimizes the residual sum of squares between the observed values and the ensemble values was used.

This was implemented using ‘sklearn.linear_model’ module in python (Pedregosa et al. 2011).

3.2.3.3.2 Support Vector Machine

SVM is based on Vapnik–Chervonenkis (VC) theory and the rule of structural risk minimization (Vapnik 1995). SVM is used for various climate change and hydrological applications (Hasan et al. 2020; Raghavendra and Deka 2014; Sachindra et al. 2018). Support Vector Regression (SVR) is the SVM that elucidates nonlinear regression problems by mapping the low-dimensional data to a high-dimensional feature space using kernel functions. Mathematically, SVR model can be represented as follows:

$$y = \sum_{i=1}^n (\alpha_i - \hat{\alpha}_i) \text{Kernel}(x_i, x) + b \quad (3.42)$$

Where $\text{Kernel}(x_i, x)$ represents the kernel function used;

α_i and $\hat{\alpha}_i$ denote the Lagrange multipliers;

x_i denote the vectors;

x represents the independent vector;

b represents the bias parameter.

SVR uses a symmetrical loss function, which equally penalizes high and low misestimates. Using Vapnik’s Open image in new window-insensitive approach, a flexible tube of the minimal radius is formed symmetrically around the estimated function, such that the absolute values of errors less than a certain threshold Open image in new window are ignored both above and below the estimate. In this manner, points outside the tube are penalized, but those within the tube, either above or below the function, receive no penalty. One of the main advantages of SVR is that its computational complexity does not depend on the dimensionality of the input space. Additionally, it has excellent generalization capability, with high prediction accuracy (Awad and Khanna 2015).

MMEs which used the polynomial kernel function performed better than the MMEs that used other kernel functions. Hence in this study polynomial kernel function was

put to use, similar to Sachindra et al. (2018) and Ahmed et al. (2020). The choice of hyperparameters plays a great role in ML methods. In the current study, the Bayesian hyperparameter optimization (BHO) was used to determine the hyperparameters for all ML algorithms. The “hyperopt” package in Python was used to implement BHO (Bergstra et al. 2015). The important hyper-parameters optimized in SVR are C, kernel function and epsilon.

3.2.3.3.3 Random Forest and Extra Tree Regressor

The RF and ETR models are ensemble ML techniques. RF is proposed by Breiman (2001) based on a combination of statistical learning theory and classification or regression methods. The multiple classification and regression decision tree included in the algorithm prevents over-fitting and adjusts different types of input variables. This algorithm generates many independent trees and generates a decision based on the characteristics of nonparametric statistical regression and randomness (Xu et al., 2019). A decision tree comprises of a root node, sub-node, and leaf node. A leaf node corresponds to a judgement level while a sub-node contains a judgement rule. The average of predicted values from all trees is the result of the algorithm. RF is internally cross-validated using Out Of Bag (OOB) score. ETR is a variation of that and adds a further level of randomness to the splitting of the trees (Geurts et al. 2006). It is an extension of RF with two major differences: 1) ETR does not apply bootstrapping, but each tree is trained with the whole of the training data, 2) ETR selects a random cut point instead of a locally optimum cut point. The split which gives the highest score is selected from the set of randomly generated splits. That is, k decision trees are generated, and m features are selected for each training sample. At each of the decision tree a random cut-point is selected. This helps to avoid overfitting to some extent. More about ETR can be found in Xu et al., (2020).

3.2.3.3.4 Long Short-Term Memory (LSTM) Deep Learning Models

Climate data is a time series data involving a sequence of observations over regularly spaced intervals with the trend (upward, downward, or absent), seasonality (periodic fluctuation within a certain period), cyclic variations (rises and falls) and irregular or random components (Bouktif et al. 2020; Mudelsee 2019). Meteorological predictions

of GCMs can be seen as multivariate sequential data. Hence the LSTM model which belongs to the family of deep recurrent neural networks, could be used for creating MMEs of climate data. The current prediction of LSTMs is influenced by the feed network activations from the previous time steps. Hence, this connection develops a memory of previous events in the LSTM network. The architecture of an LSTM cell is given in Figure 3.3 where f_t , i_t and o_t are forget, input, and output gates, respectively. X_t , S_t and C_t are input, hidden and cell state at time step t , respectively. S_{t-1} and C_{t-1} are the hidden and cell state at time step $t - 1$, respectively. \otimes , \oplus and σ are pointwise multiplication, pointwise addition and sigmoid activation, respectively.

The network has three inputs: X_t - input at the current time step, S_{t-1} is the output from the previous LSTM unit, and C_{t-1} is the memory of the previous unit. As for outputs, S_t - the output of the current network, and C_t is the memory of the current unit. The LSTM model has input i_t , output o_t , and forget f_t learnable gates that modulate the flow of information and maintains an explicit hidden state that is recursively carried forward and updated as each element of the sequential data is passed through the network. The input gate decides what information to add from the present input to the cell state, the forget gate decides what must be removed from the S_{t-1} state, thus keeping only relevant information, and the output gate decides what information to output from the current cell state. More information on LSTM can be found in Bouktif et al. (2020) and Sagheer and Kotb (2019). In this study, the LSTM was optimised for learning rate, batch size, units, layers and window.

3.2.3.4 Performance Evaluation

The observed and simulated values of P, Tmax and Tmin used for developing MMEs are divided into calibration and validation datasets. The first 45 years (1951-1995) of overlapping observed and simulated data were used for calibrating the ML models. The rest of the data were used for validating the MMEs developed using each method. Performance evaluation on validation data on a daily basis was done in terms of Root-Mean Square Error (RMSE) or Root-Mean Square Deviation (RMSD) and correlation coefficient (r). These performance indicators are widely used by many researchers (Bhatti et al. 2016; Mendez et al. 2020). Further, the daily data were converted into

monthly data for performance evaluation. Scatter plots and Taylor diagrams are used for the evaluation of performance on a monthly basis. The scatter plots, along with the coefficient of determination (R^2) provided a useful comparison of observed and MME values. Taylor diagram summarised the performance of each MME in terms of RMSD, r and standard deviation (SD). The procedure was repeated explicitly for MME's of precipitation for the monsoon season to study their ability to simulate rainfall magnitudes.

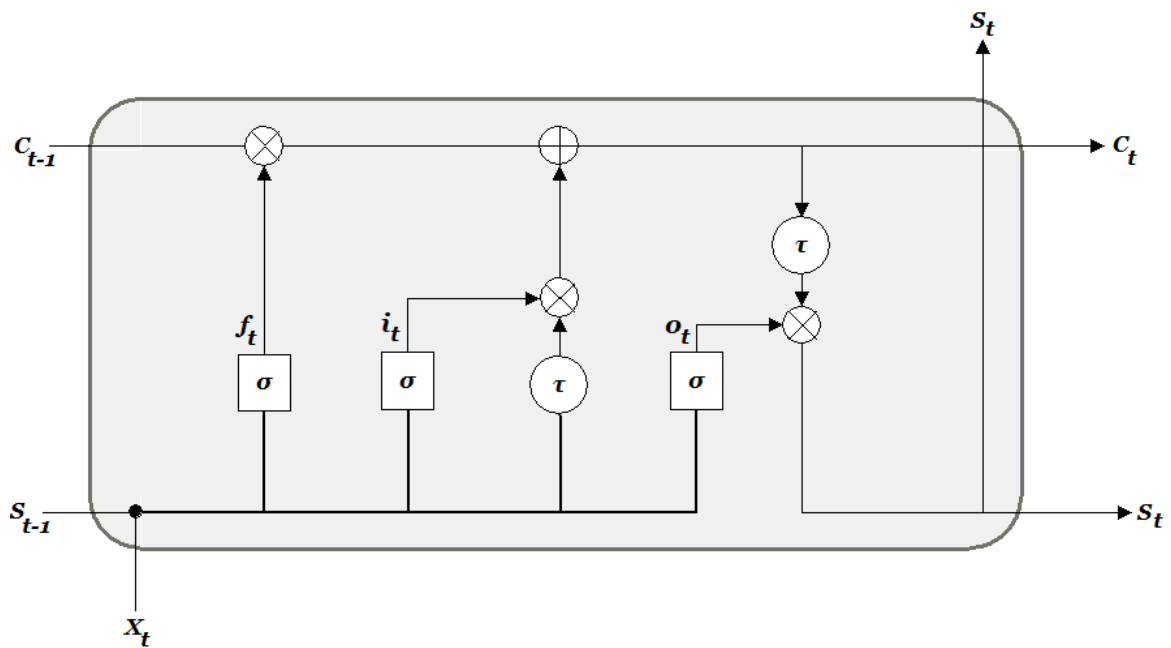


Figure 3.3 Architecture of a LSTM cell

3.2.4 LULC change detection and prediction

3.2.4.1 Data processing

Satellite images with cloud coverage of less than 10% from December to March months were used in the study. The median function, which removes noisy, very dark and bright pixels was also applied (Ghorbanian et al. 2020). Later, several spectral indices, namely Normalized Difference Vegetation Index (NDVI), Normalized Difference Built-up Index (NDBI), Modified Normalized Difference Water Index (MNDWI) and Bare Soil Index (BSI) were calculated. The formulae for each of these indices are given in Table 3.5.

Table 3.5 Spectral indices and formula

Name	Formula	Reference
NDVI	$\frac{(NIR - Red)}{(NIR + Red)}$	(Rouse et al. 1974)
NDBI	$\frac{(SWIR1 - NIR)}{(SWIR1 + NIR)}$	(Zha et al. 2003)
MNDWI	$\frac{(Green - SWIR1)}{(Green + SWIR1)}$	(Xu 2006)
BSI	$\frac{((Red + SWIR) - (NIR + Blue))}{(Red + SWIR) - (NIR + Blue)}$	(Rikimaru et al. 2002)

NDVI is widely used for identifying greenery or biomass. Its value varies from -1 to 1. A higher value of NDVI indicates dense vegetation. NDBI is used for the analysis of built-up areas. A higher value of NDBI indicates built-up areas. NDVI along with NDBI is effective in discriminating built-up from vegetation (Zha et al. 2003). MNDWI helps to identify water bodies from other features (Xu 2006). BSI helps in discriminating bare soil from other land cover types (Nguyen et al. 2021). Furthermore, “ALOS World 3D-30m” (AW3D30) dataset which was released by the Japan Aerospace Exploration Agency (JAXA), was used to generate topographic information, namely, elevation and slope. The effects of these elevation products and spectral indices on the accuracy of classification were investigated.

3.2.4.2 LULC classification

Image classification can be done in two ways: 1) supervised classification and 2) unsupervised classification. Supervised classification is preferred when enough training samples are available. Based on their data distribution assumptions, classification methods can be parametric or non-parametric (Sheykhmousa et al. 2020). The Maximum Likelihood Classifier (MLC), a parametric supervised classification method, is the most common classification method. Non-parametric ML classifiers like SVM

and RF are less commonly used but give accurate results (Yu et al. 2014). Hence, in this study SVM and RF was used for LULC classification. More about these classifiers are given below.

SVM is a kernel based ML algorithm introduced by Vapnik (1995) which is commonly used for classification applications. This method formulates an optimal hyperplane from the training data, which can separate different classes (Sheykhmousa et al. 2020). The optimum kernel function and regularisation parameter was found using a trial and error procedure. The RF classifier is a decision tree based, which was first proposed by Breiman (2001). The two important parameters which were optimised are the number of trees and the number of variables available for splitting at each tree node. More about SVM and RF can be found in Thamilselvan (2015), Hassan et al. (2020) and Sheykhmousa et al. (2020).

3.2.4.3 Selection of the best classification scenario

To study the effect of auxiliary data on LULC accuracy, four different scenarios were considered. Along with spectral reflectance values (Blue, Green, Red, NIR, SWIR1 and SWIR2), four spectral indices (NDVI, NDBI, MNDWI and BSI) and two topographic features (slope and elevation) were used in the classification process. The four scenarios are as follows:

- (1) Scenario 1: Spectral reflectance values
- (2) Scenario 2: Spectral reflectance values + spectral indices
- (3) Scenario 3: Spectral reflectance values + topographic features
- (4) Scenario 4: Spectral reflectance values + spectral indices + topographic features

These four scenarios were used for SVM and RF classifiers to identify the best classification scenario and the best classifier. Thus, eight classification models were set up.

3.2.4.4 Training and validation

Five LULC classes were considered for the study. They are water, forest, barren land, agriculture/grassland and built-up. Since ground truth data was not available, training and validation data were created through visual interpretation and with reference to

google earth images of the corresponding years. To analyse the accuracy of each LULC classification, kappa coefficient and overall accuracy (OA) were calculated.

3.2.4.5 LULC prediction

Once the best classification scenario and classification was identified for the year 2020 based on accuracy assessment, the procedure was repeated for the years 1990, 2000, 2010. The Land change modeler (LCM) module of TerrSet software was used for the creation of projected future LULC maps. This was done as a two-step process. First, the LULC of 2020 was projected using the LULC of 2000 and 2010. The projected map was compared to the actual map for validation. Later the LULC of 2010 and 2020 were used for creating the projected LULC map for 2050, 2075 and 2100. The Markov transition matrix and cellular automata are employed for creating future maps.

3.2.5 Hydrological modelling using SWAT

For the effective management of water resources at a local level, the knowledge of the impact of human activities and climate on local streamflow is vital. The soil and Water Assessment Tool (SWAT) model was used for studying the impacts of LULC and climate change on streamflow. Inputs required for the SWAT model are the DEM, digital LULC, and soil and climate data. The data products used in this study are given in Table 3.3. The SWAT model application can be divided into six steps: (1) data preparation, (2) sub-basin discretization, (3) Hydrologic Response Unit (HRU) definition, (4) parameter sensitivity analysis, (5) calibration and validation, and (6) uncertainty analysis. The methodology for SWAT simulation is given in Figure 3.4.

Sequential Uncertainty Fitting ver.2 (SUFI-2) algorithm in SWAT Calibration and Uncertainty Programs (CUP) was used for the calibration, validation and sensitivity analysis using historical LULC and climate data. The historical baseline period considered was 1990 to 2020. Hence, the meteorological data from 1990 to 2020 was used for calibration and validation of the model. The 2020 LULC map generated using the RF classifier was used as the baseline LULC map for calibration and validation. The performance of the calibrated SWAT model was evaluated NSE and R^2 .

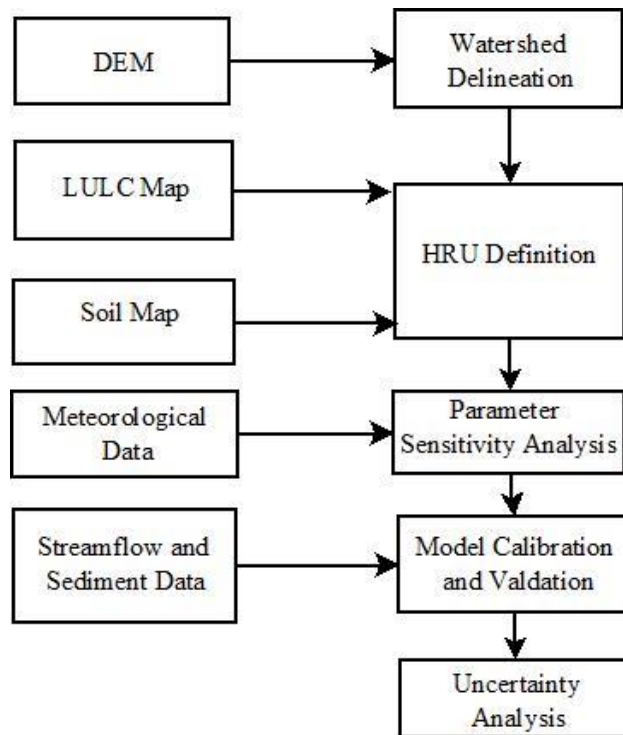


Figure 3.4 Representation of SWAT methodology

The LULC maps obtained from TerrSet model have been used for predicting the impacts of future LULC on streamflow in the calibrated SWAT model. The future climate impacts according to 2 Representative Concentration Pathways (RCPs), namely, RCP 4.5 and RCP 8.5 of CMIP5 MME and 4 Shared Socioeconomic Pathways (SSPs), namely, SSP126, SSP245, SSP370 and SSP585 of CMIP6 MME has also been evaluated using SWAT. These impacts of LULC and climate change studies are translated into three scenarios wherein the first two scenarios quantify the independent effects of LULC and climate on streamflow under their invariant counterparts; i.e., climate and LULC respectively are kept constant. The third scenario deals with concurrent changes in LULC and climate. Thus, from the scenario analysis, the effects of historical and future LULC and climate change on streamflow can be evaluated.

The hydrological part of the study was done in three scenarios:

Scenario 1: Impact of future LULC on streamflow

Scenario 2: Impact of future climate on streamflow

Scenario 3: Integrated impact of future climate and LULC on streamflow

CHAPTER 4

RESULTS AND DISCUSSION

4.1 INTRODUCTION

The results of the analysis along with discussion is included in this chapter. The results and discussion for each objective are given under the corresponding section headings. Firstly, the results and discussion of bias correction is given. It is followed by the results of ranking of GCMs and creation of MMEs. Later the results of LULC change and prediction is presented. Finally, the results and discussion of SWAT modelling is given.

4.2 BIAS CORRECTION

4.2.1 Bias correction of rainfall

Netravati basin is having tropical humid climate which is marked by heavy rainfall, high humidity, and harsh weather in the hot season. The basin has many gauging stations. Among which consistent and continuous daily rainfall data were available at nine stations in and around the basin from the year 1971 to 2014. These stations are shown in Figure 4.1. These locations are Mangalore, Buntwal, Mani, Sulya, Koila, Puttur, Subramanya, Dharmasthala and Belthangady. The rainfall data from these stations are used for the bias correction of the MRI-AGCM-2-S model. This model is referred to as GCM in the sections 4.2 and 5.1.1.

4.2.1.1 Distribution of rainfall in the basin

Rainfall is among the important climate variables for water resource planning. Figure 4.2 shows the 44 years (1971-2014) average station-wise monthly variation of rainfall in the Netravati basin. The monthly variation of rainfall is quite uniform in all the rain gauge stations indicating spatial homogeneity in monthly rainfall variability over the basin. Hence, basin averaged rainfall is considered for the trend analysis. The peak rainfall occurs in July, which is part of the south-west monsoon season. Rainfall is

minimum during December, January and February months. The south-west monsoon (June - September) is the major contributor to the annual rainfall in the basin.

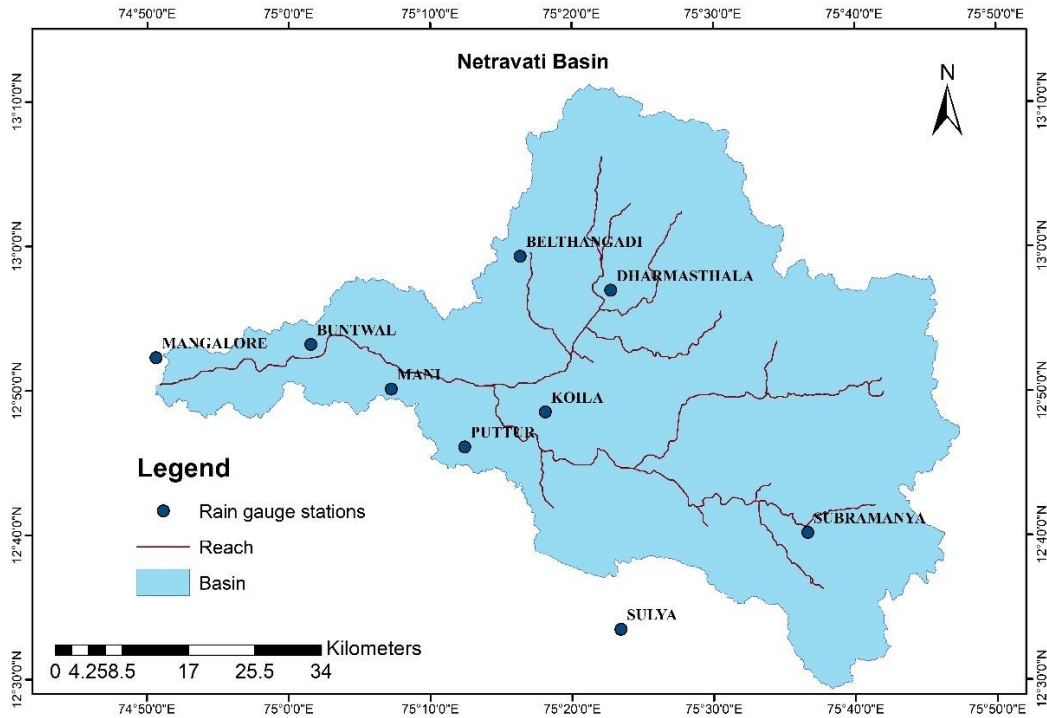


Figure 4.1 Location of Raingauge Stations

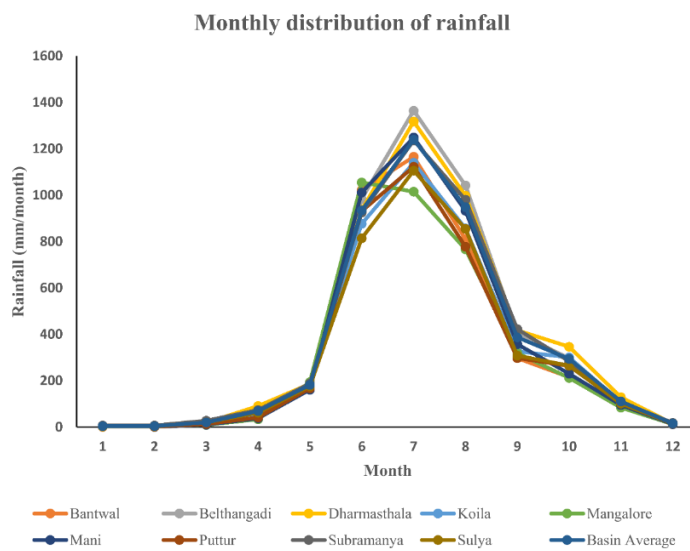


Figure 4.2 Station-wise monthly distribution of rainfall during the period 1971–2014

Figure 4.3 depicts the annual rainfall of each station along with the spatially averaged trend of rainfall in the basin from 1971 to 2014. The variability of annual rainfall among the rain gauge stations was more when compared to the monthly variations. A declining trend is seen in the annual rainfall in the basin during the period. This decline in annual rainfall was due to the decrease in monsoon rainfall. Peaks in the annual rainfall indicate flooding conditions in the basin.

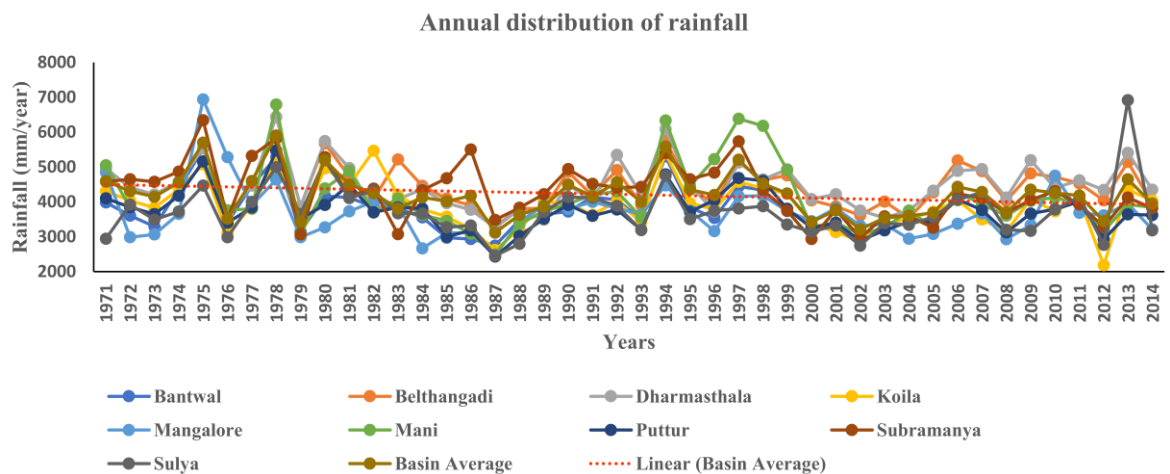


Figure 4.3 Station-wise trend of annual rainfall during 1971 and 2014

4.2.1.2 Evaluation of simulated data

A decreasing trend in annual rainfall and an increasing trend in rainy days indicate droughts may become more recurrent. Increasing rainfall and decreasing rainy days, which implies that floods may become more intense. (Kumar and Jain 2011). Also, more number of less-intense rainy days will result in reduced streamflow in the catchments (Mudbhatkal et al. 2017). Hence the correct simulation of number of rainy days is necessary.

The number of rainy days with rainfall magnitude equal to or greater than 2.4 mm (definition of a rainy day as per IMD) during each month before BC is compared with observed rainfall data from 1971 to 2014 to assess the performance of the GCM (Figure 4.4). The analysis indicates that the total number of rainy days in a year is reasonably well simulated by the GCM. However, a slight overestimation of rainy days is found for almost all months, which is anticipated to be because of the drizzle effect problem of the GCM. The overestimation is found to be more in the summer and post-monsoon

months. Nevertheless, the seasonal pattern of rainy days is well simulated by the GCM. Hence, a month-wise correction of the frequency of rainy days is necessary for the improvement of GCM simulated precipitation.

The spatially averaged mean monthly precipitation over Netravati basin (Figure 4.5) is quite well simulated by the GCM. Though the number of rainy days in the monsoon season is simulated well, there is an underestimation in the quantity of monsoon rainfall simulated by the GCM in the basin. However, the peak monsoonal occurrence is well simulated by the GCM. The biases in GCM simulations are different for each month, and hence, the degree of correction to be applied is also different.

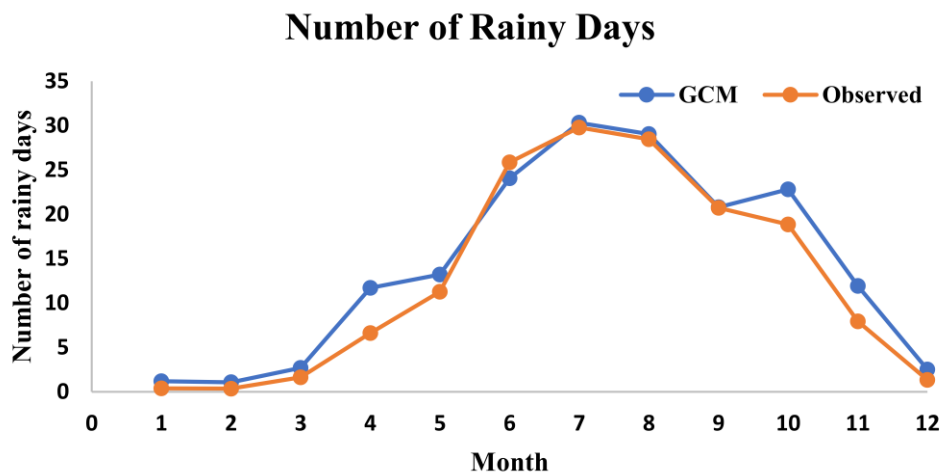


Figure 4.4 Average rainy days during the period 1971–2014

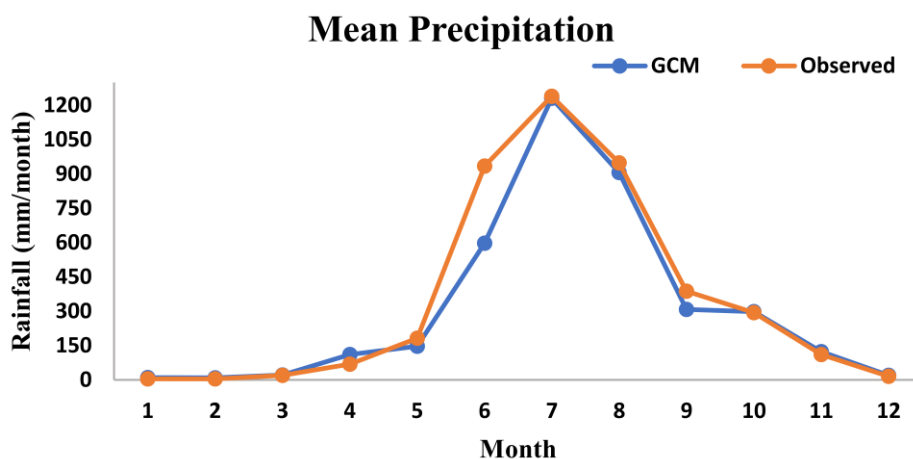


Figure 4.5 Average annual cycle of precipitation during the period 1971–2014

In short, the GCM could capture the peak rainfall and number of rainy days during south-west monsoon season. But an underestimation in the total amount of monsoon rainfall is observed. And an overestimation in the number of rainy days is observed in summer and post-monsoon season. This overestimation might be perhaps due to the drizzle effect. These ambiguities can be resolved by a suitable BC method which targets these issues.

4.2.1.3 Evaluation of Bias Correction method

Q-Q plots provide useful comparison of rainfall distribution across various rainfall values. To evaluate the overall performance of BC method on daily rainfall, Q-Q plot of observed and uncorrected/bias corrected GCM simulations were made. The rainfall data from all the rain gauges are used for calculating the spatially averaged daily rainfall data using the Thiessen polygon method.

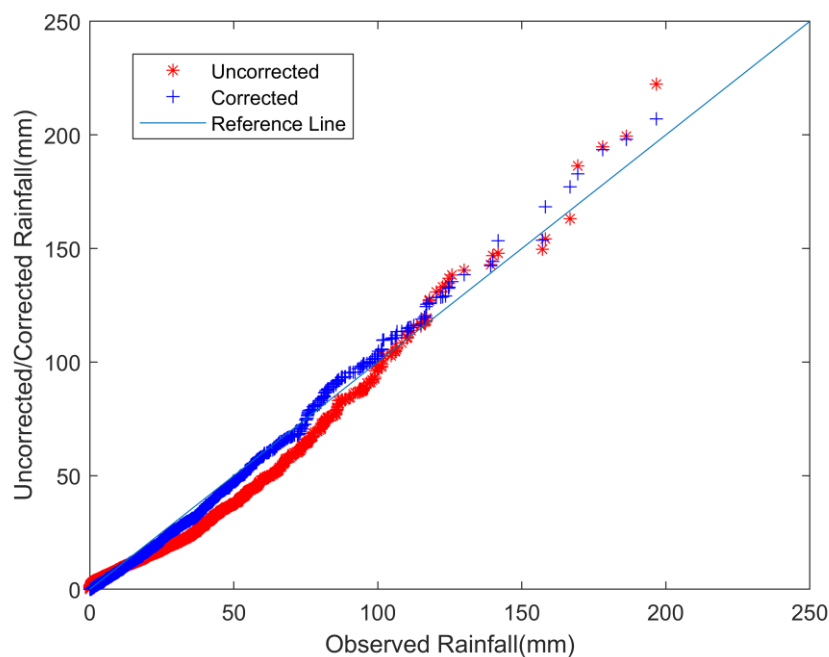


Figure 4.6 Spatially averaged daily precipitation Q-Q plot of observed and corrected/uncorrected simulated precipitation for the validation period (2001–2014)

Figure 4.6 shows the Q-Q plot of spatially averaged daily observed and bias-corrected/uncorrected model simulated precipitation data for the validation period. The bias-corrected data matches well with the observed data than the uncorrected/raw

simulated data. One can also observe that the corrected model data is overestimating the precipitation at very high precipitation values. Low and moderate precipitations are better estimated when the correction is applied. In summary, the Q-Q plot shows that bias corrected quantiles are closer to observed values than their uncorrected counterparts.

Additionally, SD, r and RMSD were also used to check the performance of BC method mainly with Taylor diagram. Figure 4.7 shows the Taylor diagram, which summarises the better performance of bias-corrected monthly precipitation when compared to uncorrected simulated data during the validation period. The r-value of corrected model precipitation is higher than the uncorrected one indicating a high correlation between the bias corrected data and the observed data. The RMSE value has substantially reduced when the correction is applied. The SD of corrected data is closer to that of observed data than raw simulated data. Hence, the Taylor diagram (Figure 4.7) summarizes that BC of GCM has considerably improved simulated precipitation values.

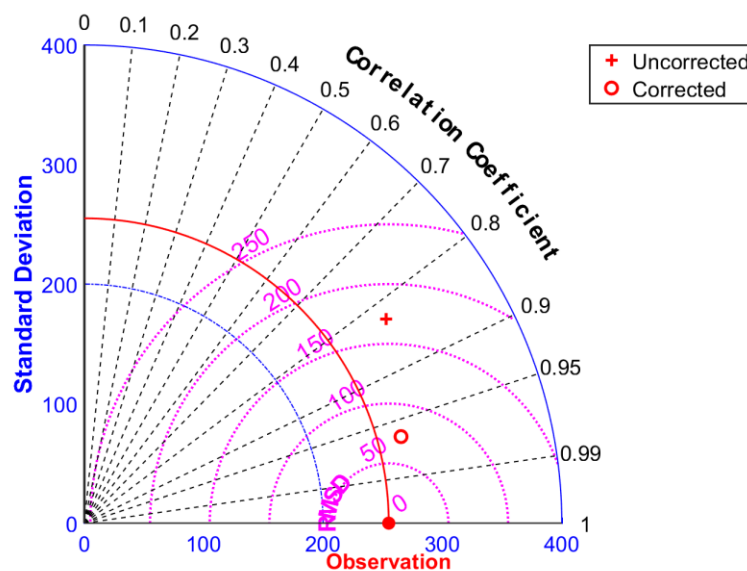


Figure 4.7 Taylor diagram of spatially averaged observed, uncorrected and bias-corrected monthly precipitation during the period 2001– 2014

Statistical evaluation of BC method was carried out for monthly precipitation during the validation period using performance measures like NSE, R^2 , MAE and PBIAS.

Table 4.1 shows the performance of corrected and uncorrected model simulated precipitation data when compared to observed precipitation in terms of NSE, R^2 , MAE and PBIAS. The uncorrected GCM data has an acceptable NSE value of greater than 0.6. However, the higher NSE value (0.75) for corrected data, when compared to raw GCM precipitation, indicates that BC can improve the performance of the model. The R^2 value (0.69) of uncorrected GCM is acceptable but lesser than the corrected one (0.79), suggesting that the bias-corrected data can better represent the precipitation patterns in the basin. The value of MAE ranges from 0 to $+\infty$. An MAE value closer to zero indicates an unbiased prediction. Thus, a lower value of MAE for bias-corrected data reflects better performance and agreement between the bias-corrected and observed data. The PBIAS calculates the relative difference between modelled and observed precipitation. A negative value of PBIAS is seen in both corrected and uncorrected GCM data, indicating an under-prediction of rainfall. However, a notable reduction in terms of PBIAS from 15.42 % to 6 % is observed in the bias corrected precipitation data when compared to the raw GCM simulation.

Table 4.1 Performance of bias correction methods in correcting monthly precipitation time series (2001-2014)

Description	NSE	R^2	MAE	PBIAS
Uncorrected Data	0.66	0.69	138.62	-15.42
Corrected Data	0.75	0.79	59.62	-6.61

4.2.2 Bias correction of temperature

4.2.2.1 Evaluation of bias correction methods

To compare the performance of each bias correction method in correcting simulated maximum and minimum temperature values, The results for one representative grid (12.5°N,75.5°E) in the basin are presented in this section. Q-Q plot of observed and uncorrected/bias corrected GCM simulations were made. Figure 4.8 shows the Q-Q plot of the daily observed and bias-corrected/uncorrected model simulated maximum temperature for the validation period. The bias-corrected data matches better with the observed data than the uncorrected/raw GCM data. One can also observe an underestimation of lower values and an overestimation of higher values of temperature

in the case of simulated maximum daily temperature. DC, EQM, AQM, GPQM and QDM methods correct the temperature values well, while the LS method overestimates the higher values of maximum temperature. Figure 4.9 shows the Q-Q plot of daily observed and bias-corrected/uncorrected simulated minimum temperature for the validation period. In general, the GCM has underestimated the values of minimum temperature. Like the case of maximum temperature, DC, EQM, AQM, GPQM and QDM performed well in the case of minimum temperature correction. The LS method slightly underestimated the lower values and overestimated the higher values in the case of minimum temperature. In summary, the Q-Q plot shows that bias corrected quantiles are nearer to reference values than their uncorrected counterparts.

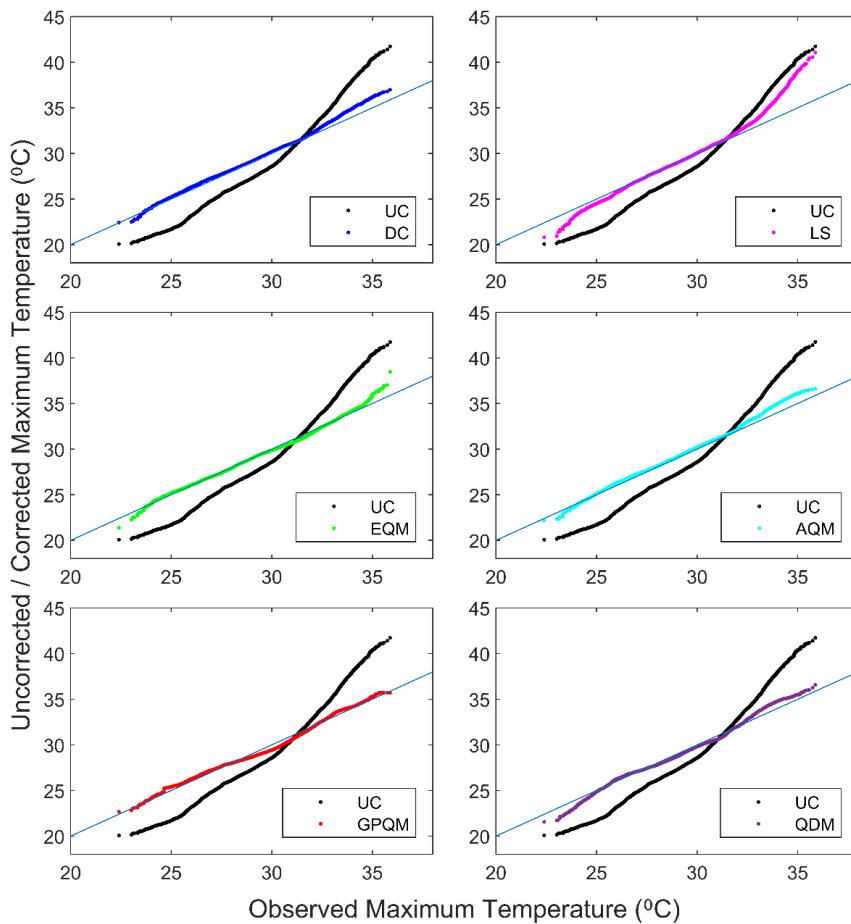


Figure 4.8 Q-Q plots comparing the observed and bias corrected/uncorrected simulated maximum temperature of an example grid cell during the validation period 1995–2014.

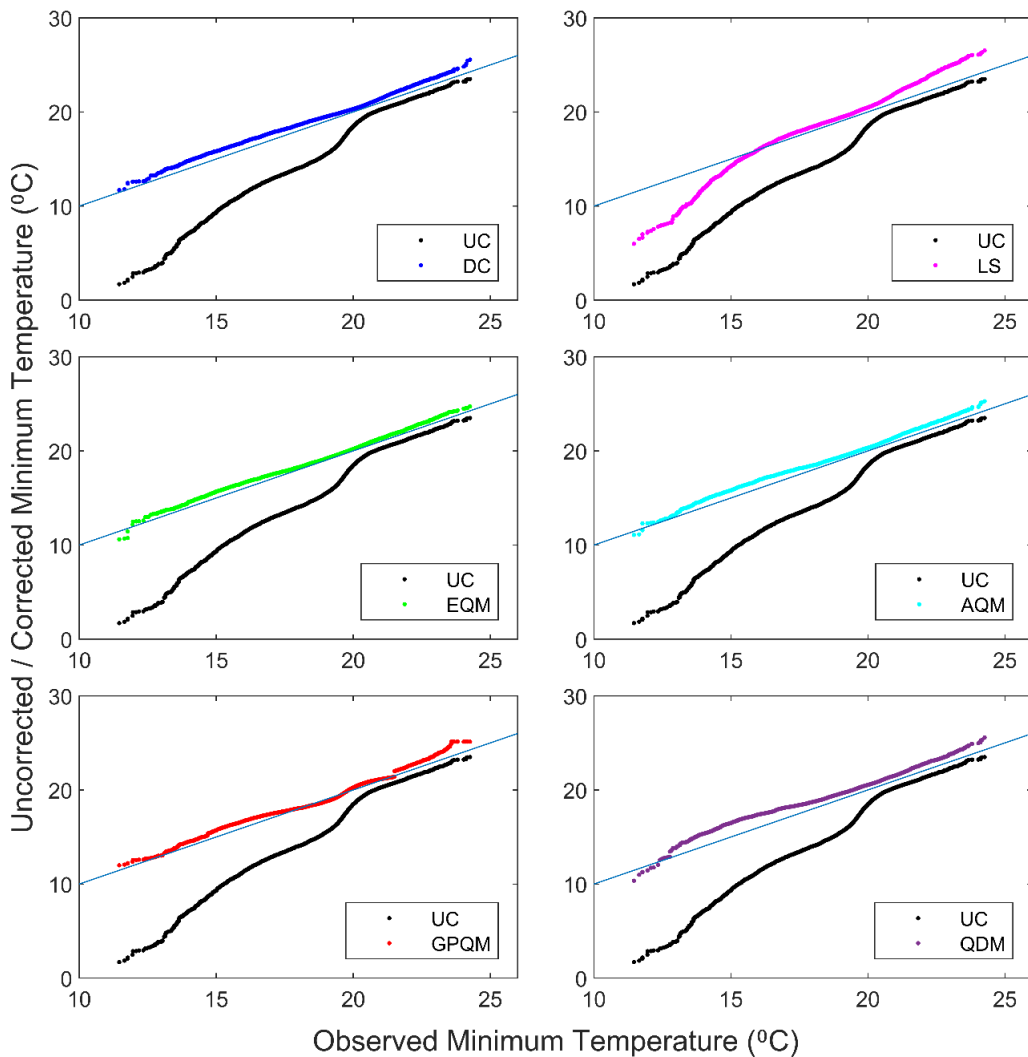


Figure 4.9 Q-Q plots comparing the observed and bias corrected/uncorrected simulated minimum temperature of an example grid cell during the validation period 1995–2014

Additionally, SD, r and RMSD were used mainly through the Taylor diagram to check the performance of BC method. Figure 4.10 shows the Taylor diagram, which summarises the better performance of bias-corrected maximum temperature when compared to uncorrected simulated data during the validation period. Even after DC, EQM, AQM, GPQM and QDM, the r values did not show a significant improvement when compared to uncorrected simulations. Further, the LS method showed a decrease in r value, indicating that the uncorrected maximum temperature has a better correlation with the observation. This might be because LS tries to correct only the difference in

means of observed and simulated data. However, the LS method was able to give lower RMSD and an SD closer to observed than the uncorrected data. DC, EQM, AQM, GPQM and QDM gave SD very close to the observed series and have reduced the magnitude of RMSD. Figure 4.11 shows the Taylor diagram, which summarises the better performance of minimum temperature simulated by BC methods when compared to uncorrected simulated data during the validation period. The DC, EQM, AQM, GPQM and QDM methods gave lesser RMSD than uncorrected simulation. These methods also gave SD closer to observations. Like the case of maximum temperature, the LS method showed an improvement in terms of SD and RMSD but a decline in r value when compared with UC data. Nevertheless, the Taylor diagrams summarise that bias correction of GCM has considerably improved simulated temperature values.

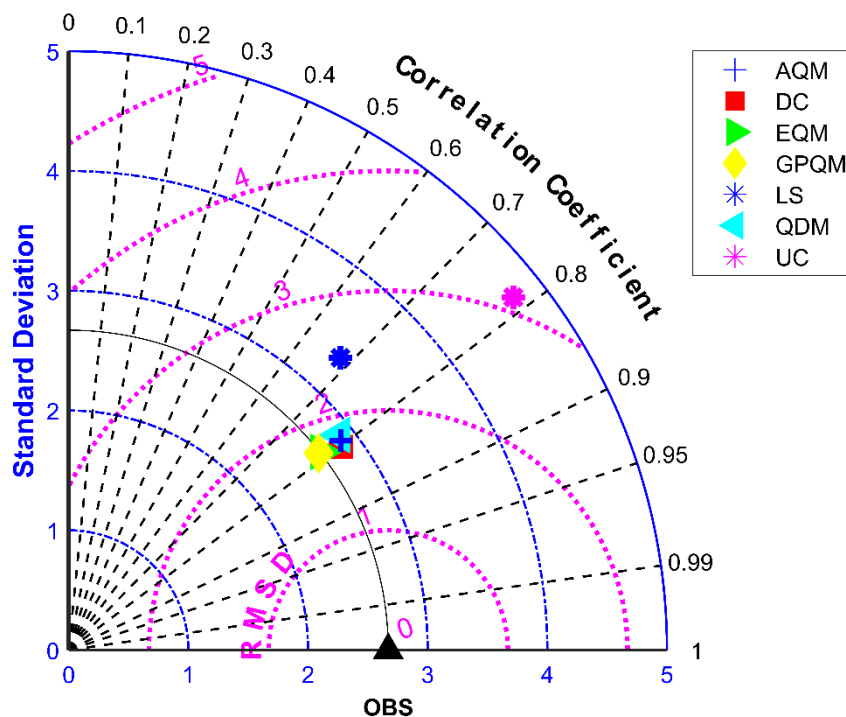


Figure 4.10 Taylor diagram of observed, uncorrected and bias-corrected maximum temperature of an example grid cell during the validation period 1995–2014.

Figure 4.12 shows the distribution of bias corrected maximum temperature values along with observed and uncorrected maximum temperature values for a year in the validation period. It shows that all bias correction methods could improve the simulated

temperature pretty well when compared to raw simulations. This figure also shows the r and RMSE values of the bias corrected data for the year. The DC and EQM methods show a higher r value (0.85) followed by AQM, GPQM and QDM (0.84). The DC, EQM, AQM, GPQM and QDM methods gave RMSE values of 1.6, 1.49, 1.64, 1.5 and 1.61, respectively. The r and RMSE values for LS are 0.76 and 2.26, respectively. This reveals that all models perform equally well in terms of r and RMSE except the LS method.

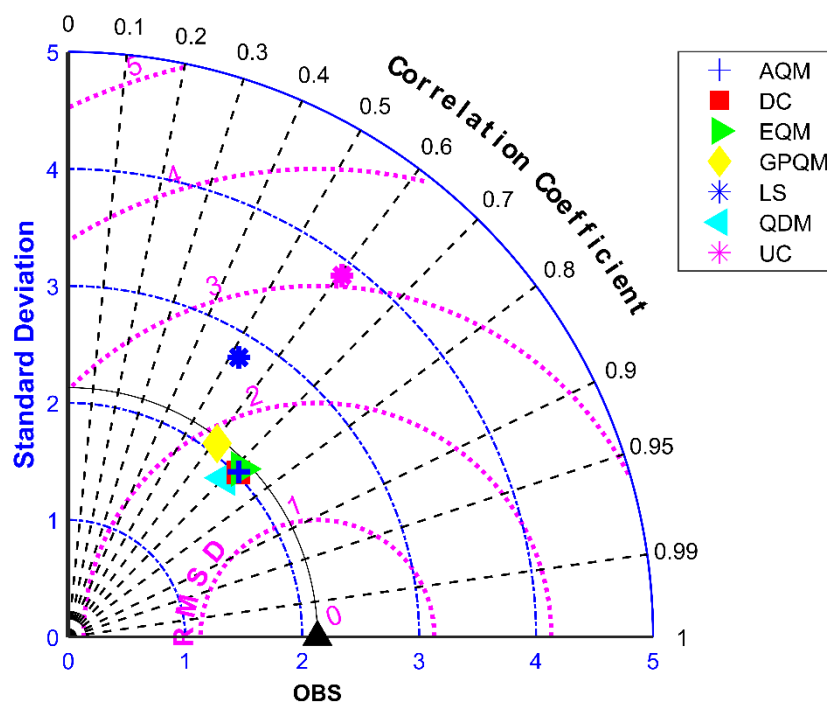


Figure 4.11 Taylor diagram of observed, uncorrected and bias-corrected minimum temperature of an example grid cell during the validation period 1995–2014.

Figure 4.13 shows the distribution of bias corrected minimum temperature values along with observed and uncorrected minimum temperature values. Improvement in the distribution is shown by all the BC methods. However, DC, EQM, AQM and QDM methods perform better than LS and GPQM methods in terms of r and RMSE. The DC, EQM, AQM and QDM methods gave r values equal to 0.8, while LS and GPQM gave r value equal to 0.6. Yet, an overall improvement in the distribution is visible in Figure 4.12 and Figure 4.13.

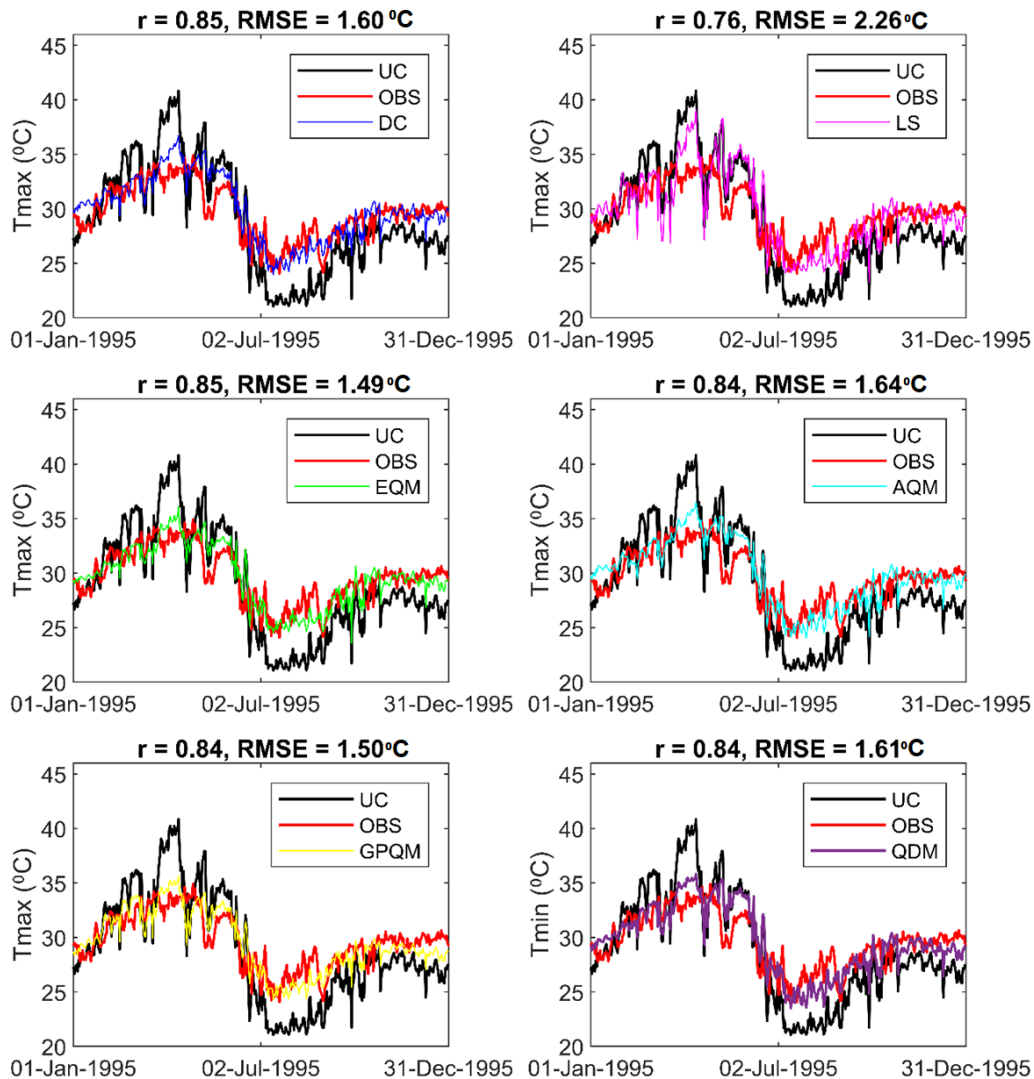


Figure 4.12 Annual distribution of bias corrected maximum temperature values along with observed and uncorrected maximum temperature values for one year
 The results of the evaluation and comparison of each bias correction method in terms of various performance indicators are given in Table 4.2 and Table 4.3. A significant improvement in NSE is seen in both maximum and minimum temperature values when BC is applied. The values of MAE and PBIAS also showed a significant reduction when BC is done. But the LS method did not show any improvement in terms of r values. However, all the other BC methods showed an improvement. The analysis also revealed that the performance of a simple bias correction method, like the DC method, could reach par with sophisticated quantile mapping methods. The superior performance of

DC was also observed by LaFond et al. (2014), Mudbhatkal and Mahesha (2018) and Mendez et al. (2020). This supports the finding by Shrestha et al. (2017) that simple bias correction methods can still be useful. But the LS method did not perform well, unlike the other BC methods considered in the study, similar to Mendez et al. (2020). The poor performance of LS prevents its use in the Netravati basin. Hence, comparison and performance evaluation are necessary while selecting a bias correction method for a specific study. However, all BC methods used in the study have improved the distribution and magnitude of GCM simulated temperature.

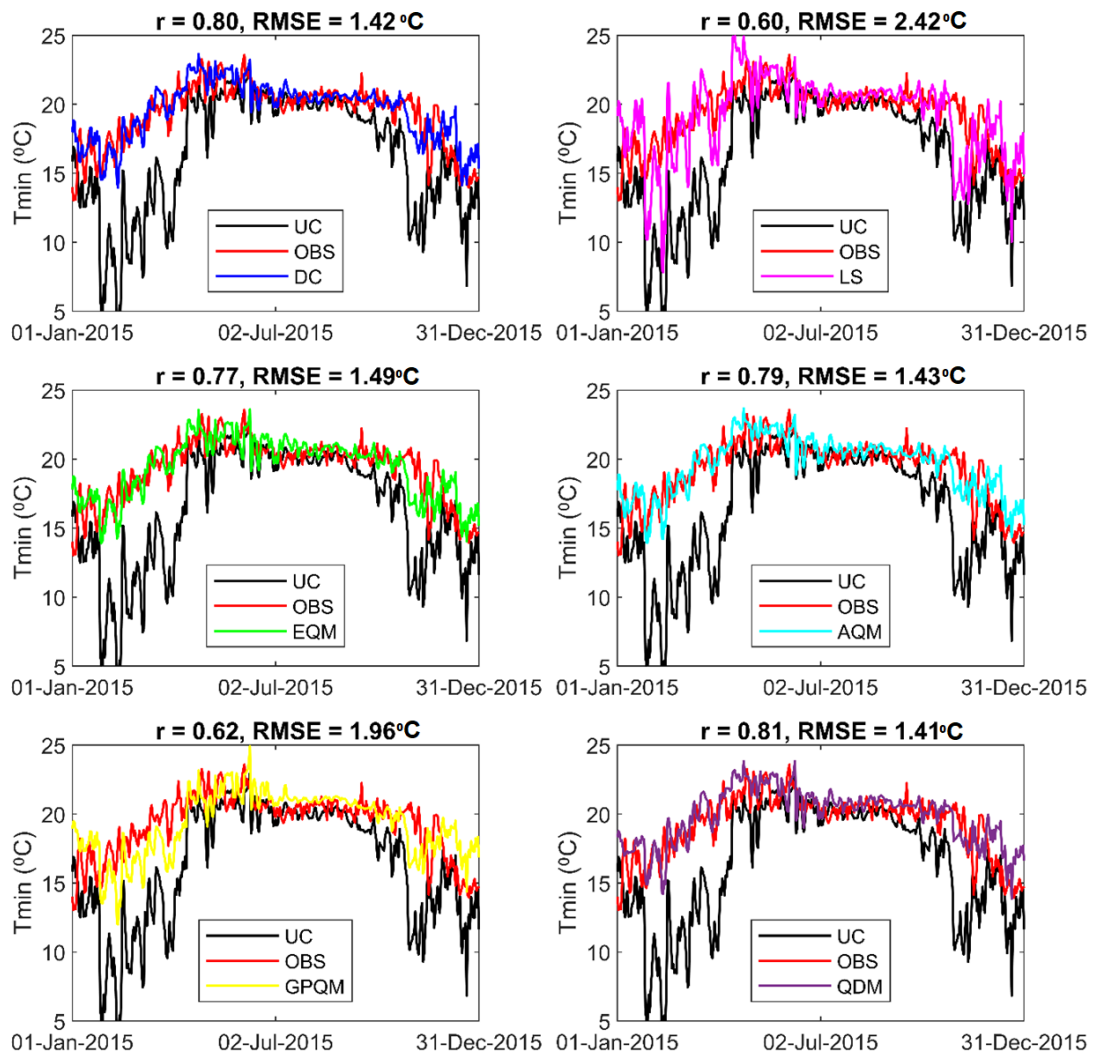


Figure 4.13 Annual distribution of bias corrected minimum temperature values along with observed and uncorrected minimum temperature values for one year

Table 4.2 Performance of bias correction methods in correcting maximum temperature daily time series (1995-2014)

Description	NSE	MAE	r	PBIAS
Uncorrected Data	-0.42	2.63	0.78	7.92
DC	0.56	1.37	0.80	-4.06
LS	0.13	1.91	0.68	-3.89
EQM	0.57	1.32	0.79	0.63
AQM	0.54	1.40	0.79	-3.91
GPQM	0.57	1.36	0.79	1.01
QDM	0.53	1.35	0.79	1.14

Table 4.3 Performance of bias correction methods in correcting minimum temperature daily time series (1995-2014)

Description	NSE	MAE	r	PBIAS
Uncorrected Data	-2.37	2.70	0.60	31.76
DC	0.41	1.20	0.72	-6.67
LS	-0.41	1.82	0.52	-6.53
EQM	0.43	1.20	0.72	-4.33
AQM	0.41	1.22	0.72	-6.50
GPQM	0.22	1.41	0.61	-3.39
QDM	0.43	1.20	0.72	-3.75

4.3 RANKING OF GCMS

The values of precipitation (12 grid points), maximum temperature (3 grid points) and minimum temperature (3 grid points) simulated by GCMs (NEX-GDDP and CMIP6 dataset) are evaluated grid-wise with respect to IMD gridded data using three performance indicators (RMSE, r and SS). The weight of each indicator is computed using the entropy method. With reference to the three indicators, individual GCMs are ranked for each grid point using 4 MCDM techniques (TOPSIS, VICOR, weighted average and PROMETHEE-II). The group decision-making method is employed to aggregate the rankings obtained from the four methods and all grid points for the whole

basin (Morais and Almeida 2012). The results thus obtained are given in the following sections.

4.3.1 Performance indicators and weights

Performance indicators give the measure of how efficiently the observations are simulated by GCMs. The values of RMSE, r and SS were calculated using equations 3.14, 3.15 and 3.19. RMSE and r were calculated on a monthly basis for each grid point. They ranged from 111.31mm to 452.64 mm and 0.50 to 0.87 respectively for precipitation of the NEX-GDDP dataset. SS quantifies the overlap between GCM-based PDF and observed PDF. The SS calculated for daily rainfall of the NEX-GDDP dataset ranged from 0.78 to 0.98, indicating good similarity between PDFs. For maximum temperature, the values of RMSE, r and SS ranged from 2.03°C to 2.46°C, 0.81 to 0.98 and 0.64 to 0.85, respectively for the NEX-GDDP dataset. While for minimum temperature, the values of RMSE, r and SS varied from 1.62°C to 4.48°C, 0.56 to 0.92 and 0.57 to 0.65, respectively.

For the CMIP6 dataset, RMSE and r ranged from 193.28 mm to 463.31 mm and 0.62 to 0.88, respectively for precipitation. The SS calculated for daily rainfall ranged from 0.87 to 0.97. For maximum temperature, the values of RMSE, r and SS ranged from 1.1°C to 3.07°C, 0.71 to 0.90 and 0.64 to 0.98, respectively. While for minimum temperature, the values of RMSE, r and SS varied from 0.93°C to 2.93°C, 0.64 to 0.86 and 0.63 to 0.96, respectively. This indicates that the performance of the CMIP6 dataset is more or less similar to that of the NEX-GDDP dataset. For demonstration, RMSE, r and SS values at the grid with latitude 12.5° and longitude 75.5° is given in Table 4.4 for precipitation simulations of the NEX-GDDP dataset. All the indicators are later normalised by using equation 3.20 to avoid the domination of one indicator over the other because of its larger range. The weights of the indicators after normalization for the grid with latitude 12.5° and longitude 75.5° are 0.51, 0.36 and 0.13 for normalised RMSE, r and SS, respectively in the case of precipitation for the NEX-GDDP dataset. This procedure is repeated for all the grids in the basin for precipitation, minimum temperature and maximum temperature simulations of NEX-GDDP and CMIP6 datasets.

Table 4.4 Performance indicators for precipitation simulated by the NEX-GDDP dataset at the the grid with latitude 12.5° and longitude 75.5°

Sl. No.	GCMs	RMSE	r	SS
1	ACCESS1-0	314.04	0.71	0.85
2	BNU-ESM	287.82	0.77	0.82
3	CCSM4	286.92	0.77	0.89
4	CESM1-BGC	284.13	0.77	0.90
5	CNRM-CM5	301.00	0.74	0.91
6	CSIRO-Mk3-6-0	326.54	0.70	0.88
7	CanESM2	296.75	0.75	0.82
8	GFDL-CM3	292.22	0.75	0.84
9	GFDL-ESM2G	297.55	0.75	0.81
10	GFDL-ESM2M	312.02	0.71	0.83
11	IPSL-CM5A-LR	318.76	0.70	0.86
12	IPSL-CM5A-MR	325.97	0.69	0.85
13	MIROC-ESM	258.67	0.84	0.83
14	MIROC-ESM-CHEM	261.75	0.83	0.83
15	MIROC5	291.75	0.76	0.91
16	MPI-ESM-LR	284.96	0.77	0.89
17	MPI-ESM-MR	275.76	0.79	0.89
18	MRI-CGCM3	339.02	0.66	0.90
19	NorESM1-M	279.78	0.78	0.86
20	BCC-CSM1-1	272.51	0.81	0.81
21	INMCM4	314.08	0.72	0.87

4.3.2 Ranking of the GCMs by different MCDM techniques and their comparison

The ranks of GCMs were calculated for precipitation, maximum temperature and minimum temperature at each grid point using TOPSIS, VIKOR, weighted average and PROMETHEE-II techniques as given in section 3.2.2.3. Table 4.5 and Table 4.6 shows the GCMs which were ranked in the first position for precipitation by the four methods at each grid point. It is observed that the best GCM found by each method at every grid point was the same. The best GCMs for precipitation are MIROC-ESM-CHEM, MIROC-ESM and MIROC5 in the case of the NEX-GDDP dataset. It is to be noted that these GCMs are developed by the same modelling centre in Japan. While BCC-

CSM2-MR, NorESM2-MM and NorESM2-LM are the best among 13 GCMs of the CMIP6 dataset. Again, two GCMs (NorESM2-MM and NorESM2-LM from Norway) from the same modelling centre performed well. Figure 4.14 and Figure 4.15 pictorially represent the best GCMs at each grid point in the basin for NEX-GDDP and CMIP6 dataset, respectively.

Table 4.5 Selected GCMs (first rank) for precipitation at different grid points in the basin for the NEX-GDDP dataset using different methods

Sl. No.	Latitude	Longitude	VIKOR	TOPSIS	Weighted Average	PROMETH EE-II	Group decision
1	12.5	75.5	MIROC-ESM	MIROC-ESM	MIROC-ESM	MIROC-ESM	MIROC-ESM
2	12.5	75.75	MIROC-ESM-CHEM	MIROC-ESM-CHEM	MIROC-ESM-CHEM	MIROC-ESM-CHEM	MIROC-ESM-CHEM
3	12.75	75.00	MIROC-ESM	MIROC-ESM	MIROC-ESM	MIROC-ESM	MIROC-ESM
4	12.75	75.25	MIROC-ESM-CHEM	MIROC-ESM-CHEM	MIROC-ESM-CHEM	MIROC-ESM-CHEM	MIROC-ESM-CHEM
5	12.75	75.50	MIROC5	MIROC5	MIROC5	MIROC5	MIROC5
6	12.75	75.75	MIROC-ESM-CHEM	MIROC-ESM-CHEM	MIROC-ESM-CHEM	MIROC-ESM-CHEM	MIROC-ESM-CHEM
7	13.00	75.00	MIROC-ESM	MIROC-ESM	MIROC-ESM	MIROC-ESM	MIROC-ESM
8	13.00	75.25	MIROC-ESM-CHEM	MIROC-ESM-CHEM	MIROC-ESM-CHEM	MIROC-ESM-CHEM	MIROC-ESM-CHEM
9	13.00	75.50	MIROC-ESM-CHEM	MIROC-ESM-CHEM	MIROC-ESM-CHEM	MIROC-ESM-CHEM	MIROC-ESM-CHEM
10	13.00	75.75	MIROC-ESM-CHEM	MIROC-ESM-CHEM	MIROC-ESM-CHEM	MIROC-ESM-CHEM	MIROC-ESM-CHEM
11	13.25	75.25	MIROC-ESM	MIROC-ESM	MIROC-ESM	MIROC-ESM	MIROC-ESM
12	13.25	75.50	MIROC-ESM	MIROC-ESM	MIROC-ESM	MIROC-ESM	MIROC-ESM

Table 4.6 Selected GCMs (first rank) for precipitation at different grid points in the basin for the CMIP6 dataset using different methods

Sl. No.	Latitude	Longitude	VIKOR	TOPSIS	Weighted Average	PROMET HEE-II	Group decision
1	12.5	75.5	NorESM2-LM	NorESM2-LM	NorESM2-LM	NorESM2-LM	NorESM2-LM
2	12.5	75.75	BCC-CSM2-MR	BCC-CSM2-MR	BCC-CSM2-MR	BCC-CSM2-MR	BCC-CSM2-MR
3	12.75	75.00	BCC-CSM2-MR	BCC-CSM2-MR	BCC-CSM2-MR	BCC-CSM2-MR	BCC-CSM2-MR
4	12.75	75.25	BCC-CSM2-MR	BCC-CSM2-MR	BCC-CSM2-MR	BCC-CSM2-MR	BCC-CSM2-MR
5	12.75	75.50	NorESM2-LM	NorESM2-LM	NorESM2-LM	NorESM2-LM	NorESM2-LM
6	12.75	75.75	BCC-CSM2-MR	BCC-CSM2-MR	BCC-CSM2-MR	NorESM2-MM	BCC-CSM2-MR
7	13.00	75.00	BCC-CSM2-MR	BCC-CSM2-MR	BCC-CSM2-MR	BCC-CSM2-MR	BCC-CSM2-MR
8	13.00	75.25	BCC-CSM2-MR	BCC-CSM2-MR	BCC-CSM2-MR	BCC-CSM2-MR	BCC-CSM2-MR
9	13.00	75.50	BCC-CSM2-MR	BCC-CSM2-MR	BCC-CSM2-MR	BCC-CSM2-MR	BCC-CSM2-MR
10	13.00	75.75	BCC-CSM2-MR	BCC-CSM2-MR	BCC-CSM2-MR	NorESM2-MM	BCC-CSM2-MR
11	13.25	75.25	NorESM2-MM	NorESM2-MM	NorESM2-MM	NorESM2-MM	NorESM2-MM
12	13.25	75.50	NorESM2-LM	NorESM2-LM	NorESM2-LM	NorESM2-LM	NorESM2-LM

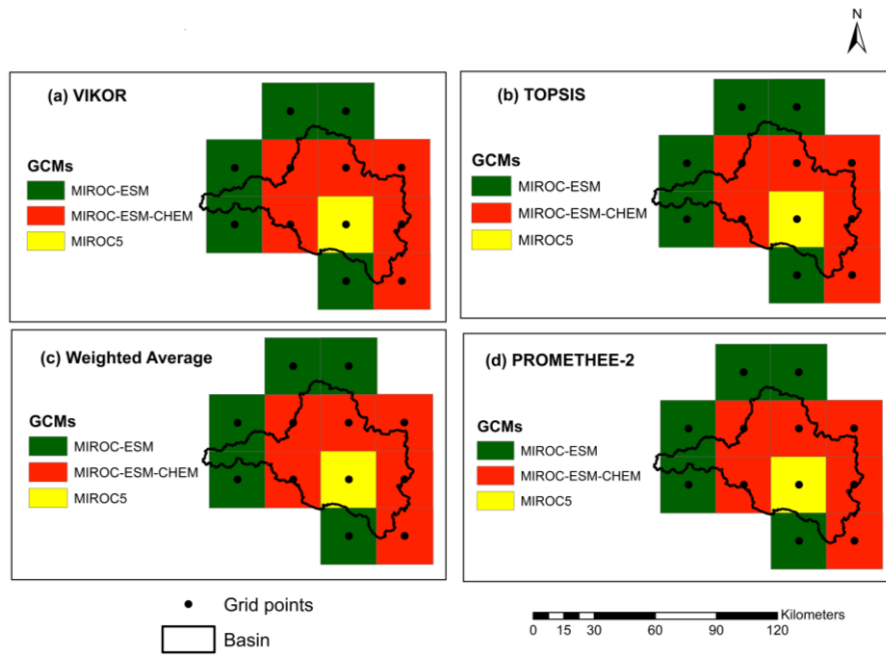


Figure 4.14 GCMs occupying first positions by a) VIKOR, b) TOPSIS, c) weighted average and d) PROMETHEE-II methods in the case of precipitation for NEX-GDDP dataset

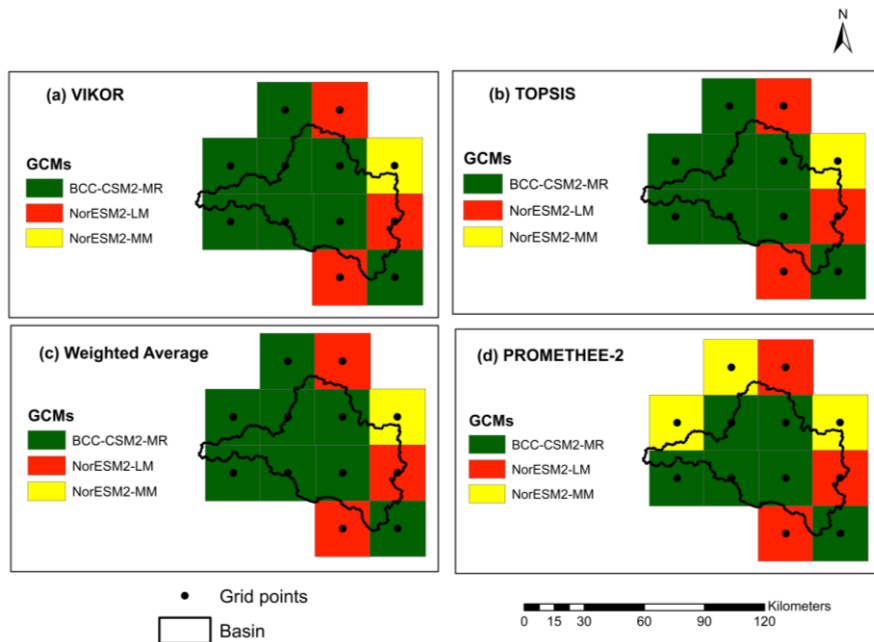


Figure 4.15 GCMs occupying first positions by a) VIKOR, b) TOPSIS, c) weighted average and d) PROMETHEE-II methods in the case of precipitation for CMIP6 dataset

Table 4.7 and Table 4.8 gives the list of best GCMs for temperature simulations at each grid point for NEX-GDDP and CMIP6 datasets. CNRM-CM5, BCC-CSM1-1 and IPSL-CM5A-MR are found to be the best GCMs for maximum temperature simulations of the NEX-GDDP dataset. While MIROC-ESM, MRI-CGCM3 and IPSL-CM5A-LR performed well in the case of minimum temperature. MPI-ESM1-2-HR was found to be the best model at every grid point for maximum temperature simulations of the CMIP6 dataset. While INM-CM5-0 and CanESM5 simulated minimum temperature well in the basin. Figure 4.16 and Figure 4.17 show the best GCMs of the NEX-GDDP dataset which simulates the temperature at each grid point. Figure 4.18 and Figure 4.19 give a better understanding of the spatial distribution of GCMs with the first rank for temperature in the case of the CMIP6 dataset.

Table 4.7 Selected GCMs (first rank) for maximum and minimum temperature at different grid points in the basin for NEX-GDDP dataset using different methods

Sl. No.	Latitude	Longitude	VIKOR	TOPSIS	Weighted Average	PROMETHEE-II	Group decision
Maximum Temperature							
1	12.50	75.50	CNRM-CM5	CNRM-CM5	CNRM-CM5	BCC-CSM1-1	CNRM-CM5
2	13.50	75.50	BCC-CSM1-1	BCC-CSM1-1	BCC-CSM1-1	BCC-CSM1-1	BCC-CSM1-1
3	12.50	74.50	CCSM4	IPSL-CM5A-MR	IPSL-CM5A-MR	IPSL-CM5A-MR	IPSL-CM5A-MR
Minimum Temperature							
1	12.50	75.50	MIROC-ESM	MIROC-ESM-CHEM	MIROC-ESM	MIROC-ESM	MIROC-ESM
2	13.50	75.50	MRI-CGCM3	MRI-CGCM3	MRI-CGCM3	MRI-CGCM3	MRI-CGCM3
3	12.50	74.50	IPSL-CM5A-LR	IPSL-CM5A-LR	IPSL-CM5A-LR	IPSL-CM5A-LR	IPSL-CM5A-LR

Table 4.8 Selected GCMs (first rank) for maximum and minimum temperature at different grid points in the basin for CMIP6 dataset using different methods

Sl. No.	Latitude	Longitude	VIKOR	TOPSIS	Weighted Average	PROMETHEE-II	Group decision
Maximum Temperature							
1	12.50	75.50	MPI-ESM1-2-HR	MPI-ESM1-2-HR	MPI-ESM1-2-HR	MPI-ESM1-2-HR	MPI-ESM1-2-HR
2	13.50	75.50	MPI-ESM1-2-HR	MPI-ESM1-2-HR	MPI-ESM1-2-HR	MPI-ESM1-2-HR	MPI-ESM1-2-HR
3	12.50	74.50	MPI-ESM1-2-HR	MPI-ESM1-2-HR	MPI-ESM1-2-HR	MPI-ESM1-2-HR	MPI-ESM1-2-HR
Minimum Temperature							
1	12.50	75.50	INM-CM5-0	INM-CM5-0	INM-CM5-0	INM-CM5-0	INM-CM5-0
2	13.50	75.50	INM-CM5-0	INM-CM5-0	INM-CM5-0	INM-CM5-0	INM-CM5-0
3	12.50	74.50	CanESM5	CanESM5	CanESM5	CanESM5	CanESM5

4.3.3 Group ranking of GCMs

Group decision-making is a procedure in which ranking pattern with reference to individual ranking techniques are integrated to form a single group preference (Raju and Kumar 2018). Also, in a situation when a large number of grid points are involved an unsatisfactory inference may be made. In such a case, group decision making can be employed, to form a single preference (Raju et al. 2017). Group ranking procedure also nullifies the errors which may else come in because of the limitations of an individual ranking method. Thus, a group ranking procedure is adopted for the study considering 4 ranking methods.

The correlation between ranks obtained from the four methods was calculated to see the similarity in the rankings. The Spearman correlation coefficient, thus obtained, is given in Table 4.9 and Table 4.10. The correlation of ranking by different MCDM methods was more than 0.94 for precipitation and maximum temperature in the case of the NEX-GDDP dataset. However, for minimum temperature, the correlation coefficient was above 0.81. The correlation coefficient was above 0.98 in all the cases of the CMIP6 dataset. By considering the ranking given by 4 MCDM techniques, the

group ranks were calculated as described in Section 4.4. Table 4.5, Table 4.6, Table 4.7 and Table 4.8 provide the list of GCMs which came first after performing the group ranking procedure at each grid point. Figure 4.20, Figure 4.21 and Figure 4.22 give the spatial distribution of GCMs, which came in the first, second, third and fourth positions for precipitation, minimum temperature and maximum temperature for the NEX-GDDP dataset after group decision making. Figure 4.23, Figure 4.24 and Figure 4.25 give the top 4 GCMs for precipitation, maximum temperature and minimum temperature for the CMIP6 dataset by group decision making procedure.

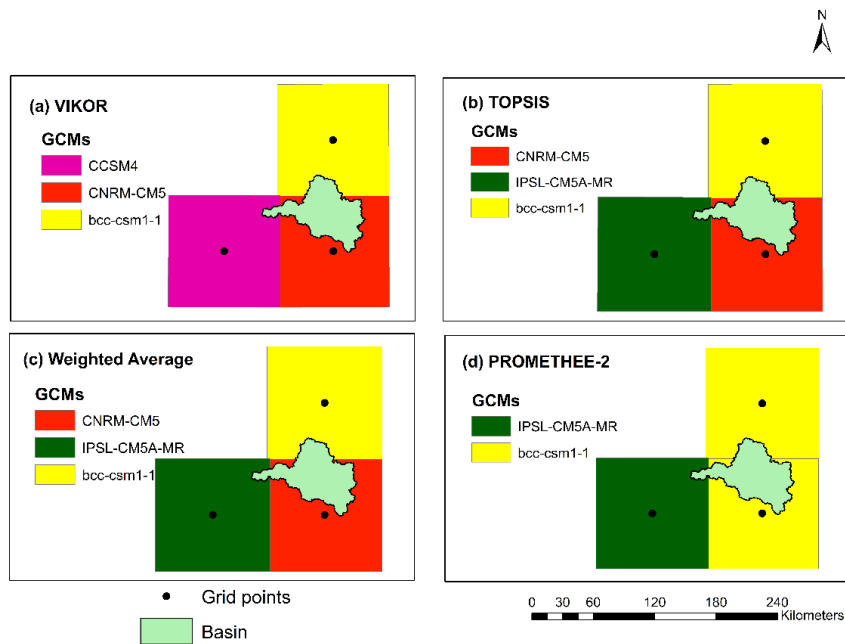


Figure 4.16 GCMs occupying first positions by a) VIKOR, b) TOPSIS, c) Weighted Average and d) PROMETHEE-II methods in the case of maximum temperature for NEX-GDDP dataset

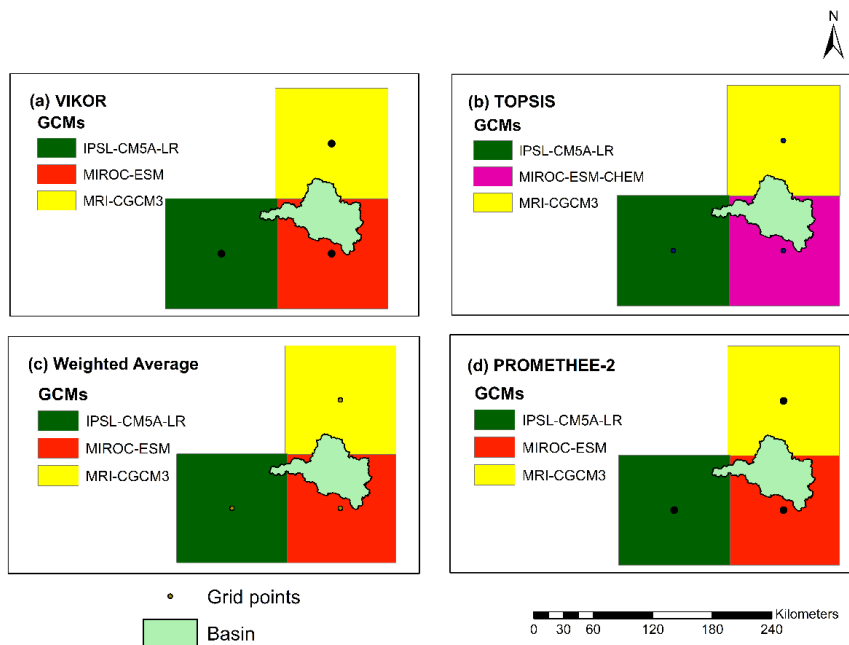


Figure 4.17 GCMs occupying first positions by a) VIKOR, b) TOPSIS, c) Weighted Average and d) PROMETHEE-II methods in the case of minimum temperature for NEX-GDDP dataset

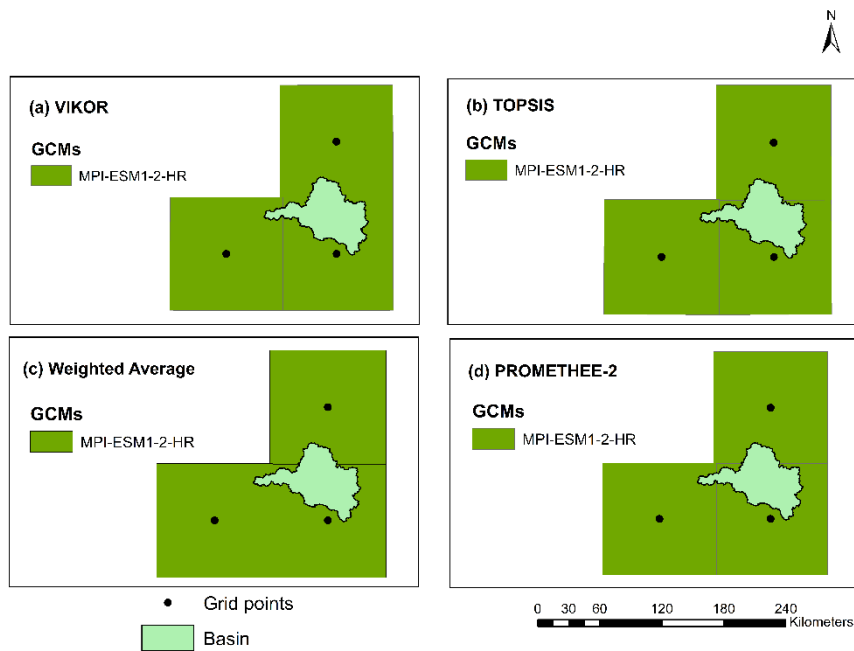


Figure 4.18 GCMs occupying first positions by a) VIKOR, b) TOPSIS, c) Weighted Average and d) PROMETHEE-II methods in the case of maximum temperature for CMIP6 dataset

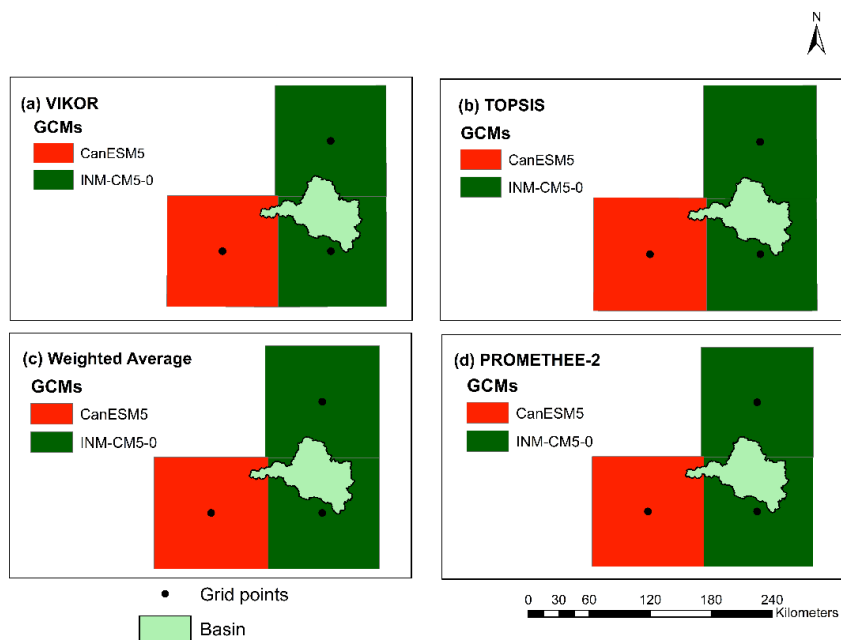


Figure 4.19 GCMs occupying first positions by a) VIKOR, b) TOPSIS, c) Weighted Average and d) PROMETHEE-II methods in the case of minimum temperature for CMIP6 dataset

Table 4.9 Correlation between ranks obtained from different MCDM techniques for the NEX-GDDP dataset

	TOPSIS and VIKOR	TOPSIS and weighted average	Weighted average and PROMETHEE-II	VIKOR and weighted average	VIKOR and PROMETHEE-II	TOPSIS and PROMETHEE-II
Precipitation	0.970	0.957	0.948	0.952	0.966	0.962
Maximum Temperature	0.969	0.992	0.966	0.975	0.969	0.964
Minimum Temperature	0.832	0.967	0.880	0.845	0.818	0.892

Table 4.10 Correlation between ranks obtained from different MCDM techniques for the CMIP6 dataset

	TOPSIS and VIKOR	TOPSIS and weighted average	Weighted average and PROMETHEE-II	VIKOR and weighted average	VIKOR and PROMETHEE-II	TOPSIS and PROMETHEE-II
Precipitation	0.998	0.997	0.991	0.995	0.989	0.991
Maximum Temperature	1	1	1	1	1	1
Minimum Temperature	0.998	1	0.996	0.998	0.998	0.996

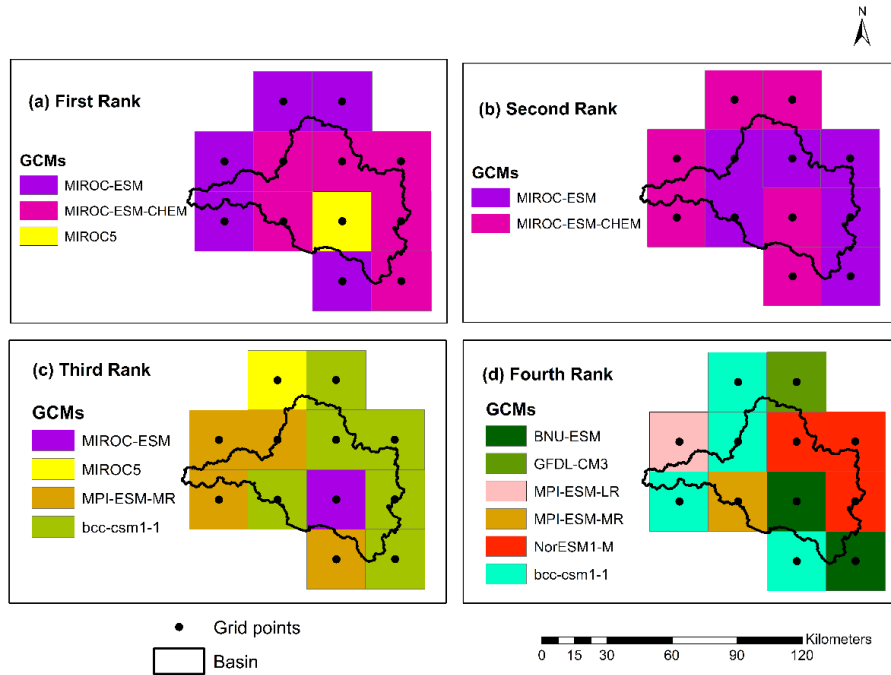


Figure 4.20 GCMs occupying first four positions after group decision-making technique in the case of precipitation for NEX-GDDP dataset

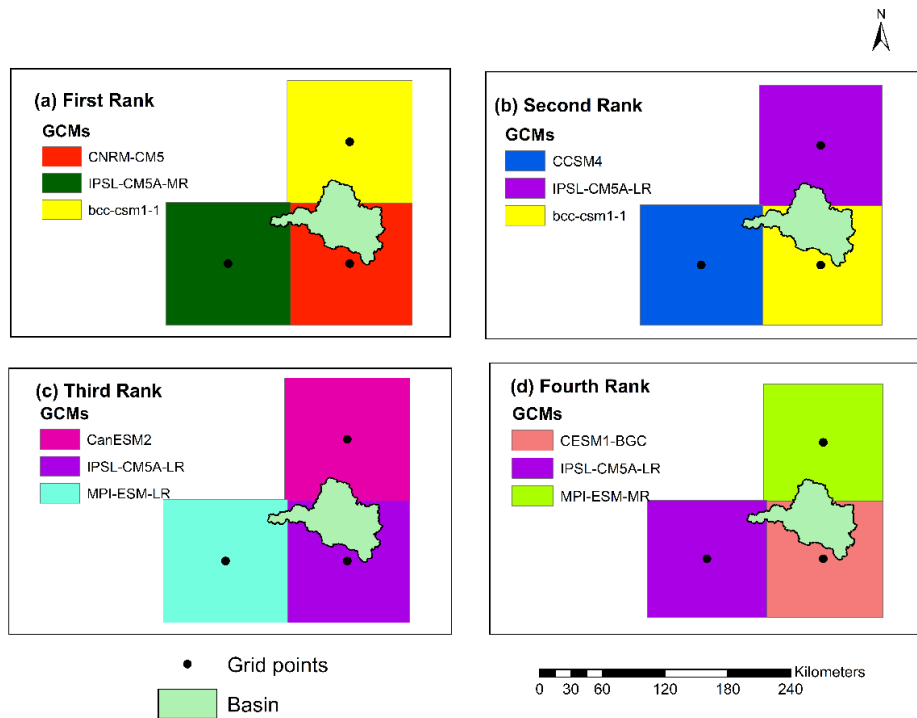


Figure 4.21 GCMs occupying first four positions after group decision-making technique in case the of maximum temperature for NEX-GDDP dataset

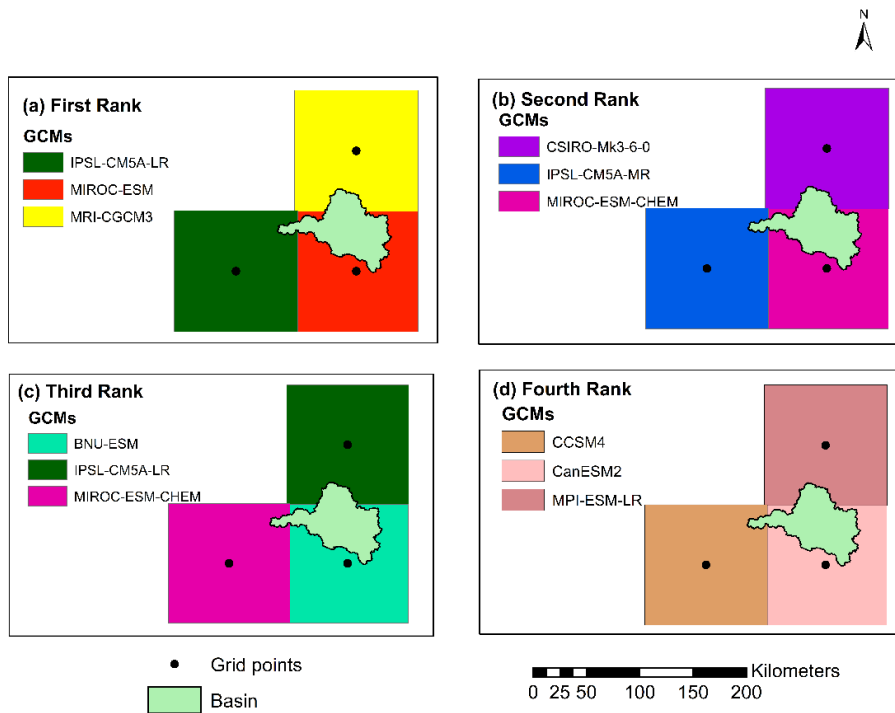


Figure 4.22 GCMs occupying first four positions after group decision-making technique in the case of minimum temperature for NEX-GDDP dataset

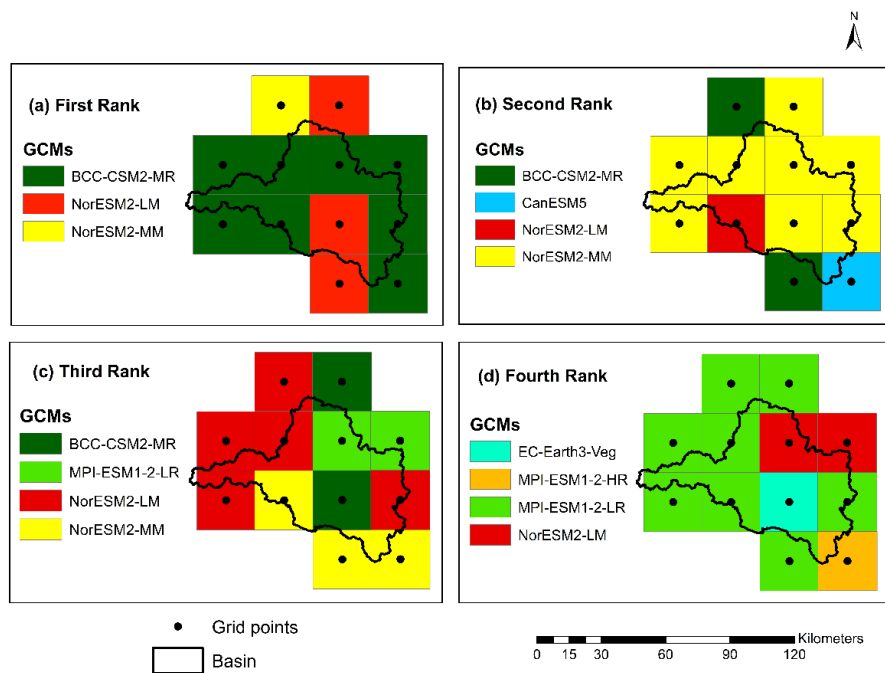


Figure 4.23 GCMs occupying first four positions after group decision-making technique in the case of precipitation for CMIP6 dataset

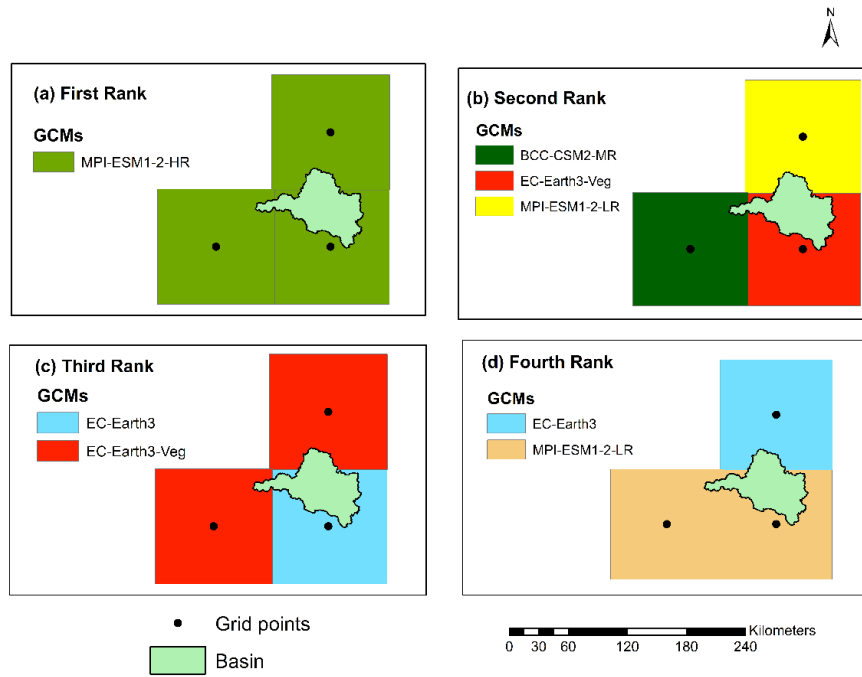


Figure 4.24 GCMs occupying first four positions after group decision-making technique in case the of maximum temperature for CMIP6 dataset

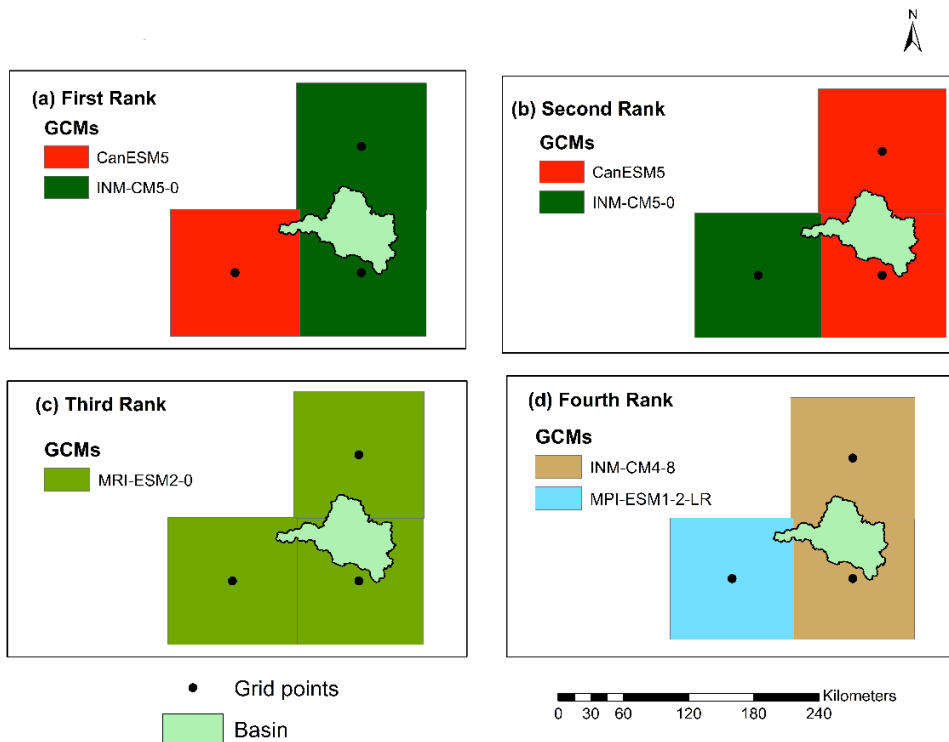


Figure 4.25 GCMs occupying first four positions after group decision-making technique in the case of minimum temperature for CMIP6 dataset

Further, an attempt was made to find the best GCMs by group decision making for the whole basin in case of precipitation, maximum and minimum temperatures. Table 4.11 shows the result of group decision making for NEX-GDDP GCMs in the basin. MIROC-ESM-CHEM was seen as the best GCM for precipitation, while IPSL-CM5A-LR was found to be the best for minimum and maximum temperature in the basin for the NEX-GDDP dataset.

Table 4.12 shows ranking of CMIP6 GCMs for the basin. BCC-CSM2-MR was seen as the best GCM for precipitation, while INM-CM5-0 and MPI-ESM1-2-HR were found to be the best for minimum and maximum temperature in the basin for the CMIP6 dataset.

Table 4.11 Ranking of NEX-GDDP dataset for the basin

Sl. No.	GCMs	Precipitation	Maximum Temperature	Minimum Temperature
1	ACCESS1-0	11	16	15
2	BNU-ESM	8	15	6
3	CCSM4	12	2	12
4	CESM1-BGC	19	4	18
5	CNRM-CM5	20	9	8
6	CSIRO-Mk3-6-0	14	20	14
7	CanESM2	18	10	10
8	GFDL-CM3	17	21	16
9	GFDL-ESM2G	21	12	21
10	GFDL-ESM2M	16	11	20
11	IPSL-CM5A-LR	15	1	1
12	IPSL-CM5A-MR	10	8	4
13	MIROC-ESM	2	17	3
14	MIROC-ESM-CHEM	1	13	2
15	MIROC5	9	19	11
16	MPI-ESM-LR	5	6	7
17	MPI-ESM-MR	6	5	17
18	MRI-CGCM3	7	18	5
19	NorESM1-M	4	3	13
20	BCC-CSM1-1	3	7	19
21	INMCM4	13	14	9

Table 4.12 Ranking of CMIP6 dataset GCMs for the basin

Sl. No.	GCMs	Precipitation	Maximum Temperature	Minimum Temperature
1	ACCESS-CM2	10	9	5
2	ACCESS-ESM1-5	11	6	13
3	BCC-CSM2-MR	1	4	9
4	CanESM5	7	11	2
5	EC-Earth3	6	5	10
6	EC-Earth3-Veg	5	2	7
7	INM-CM4-8	13	13	4
8	INM-CM5-0	12	7	1
9	MPI-ESM1-2-HR	8	1	8
10	MPI-ESM1-2-LR	4	3	6
11	MRI-ESM2-0	9	12	3
12	NorESM2-LM	3	10	12
13	NorESM2-MM	2	8	11

4.3.4 Discussion

The ranges of RMSE, r and SS indicate that there is a huge difference in the performance of various GCMs. It was observed that a GCM might perform well for one performance indicator but poorly for another at the same time. It is also noted that, generally, SS is higher for precipitation and r is higher for temperature. Thus, rather than assuming equal weights, an opportunity to differentiate the weights of each indicator based on their characteristics is provided by using the entropy method. This method gave high importance to normalised RMSE than r and SS. The same was observed by Raju et al. (2017). The results obtained after performance evaluation show that NEX-GDDP and CMIP6 datasets have more or less the same performance in terms of SS, r and RMSE. Hence, one can use any of these datasets according to their convenience. For further clarification, performance evaluation on seasonal/extreme values may be done in the future.

The best GCMs for precipitation in the NEX-GDDP dataset were MIROC-ESM-CHEM, MIROC-ESM and MIROC5, developed by the same modelling centre in Japan. While BCC-CSM2-MR, NorESM2-LM and NorESM2-MM performed the best among 13 GCMs of the CMIP6 dataset of which two are from Norway. The correlations of rankings by four

methods were higher for precipitation and maximum temperature than the minimum temperature in the case of the NEX-GDDP dataset. However, for the CMIP6 dataset, maximum temperature shows the highest correlation between the rankings provided by each method. Unlike in the case of precipitation, the GCMs which were ranked first by each MCDM method at every grid was not always the same in the case of temperature. This might be because of the inherent differences in each MCDM method. The GCMs which simulate maximum temperature well are not the ones which simulate the minimum temperature well. In summary, the 4 MCDM methods showed high correlation or similarity in their results.

The GCMs of the CMIP5 dataset selected in the study were different from those found by Raju and Kumar (2014a) and Raju and Kumar (2015). This is because of the fact that the GCMs selected are based on a different gridded dataset and at a different resolution. The same was also concluded by Khan et al. (2018). It is also noted that the knack of each GCM to mimic temperature and precipitation is different in the basin. Hence, for each climate variable, the performance of GCM should be evaluated individually. In light of previous studies, it has been highlighted that a model performing the best in a particular region might not be the best in other regions. This must be because of the differences in climatic conditions in each region (Errasti et al. 2011; Zamani and Berndtsson 2019). In order to get robust and reliable rankings, the performance evaluation of GCMs should be done using different indicators and methods. But this does not give the assurance that this approach would result in the selection of the best predictor of future climate (Reichler and Kim 2008). The general idea is that the GCM which performs better in the past would give reliable results in the future (Errasti et al. 2011). Acknowledging these assumptions, the outcomes of this study may be utilized in future studies.

4.4 CREATION OF MMES

The performance evaluation of each ensembling method for simulating P, T_{min} and T_{max} is done grid-wise on daily and monthly scales for NEX-GDDP and CMIP6 datasets separately. The performance evaluation on the daily scale is done using *r* and RMSE. Results of this evaluation during the validation period are given in Table 4.13. Further, scatter plots and Taylor diagrams are used to evaluate the performance on a monthly basis. The performance of each ML method was more or less the same at each grid. Hence, the

results obtained for one representative grid in the basin are shown and discussed for simplification of the presentation.

Table 4.13 Performance of various MMEs in simulating daily P, Tmin and Tmax

Methods	Precipitation		Minimum temperature		Maximum Temperature	
	r	RMSE (mm)	r	RMSE (°C)	r	RMSE (°C)
NEX-GDDP dataset						
Mean	0.519	19.03	0.522	1.78	0.484	2.33
MLR	0.552	18.55	0.828	1.15	0.838	1.45
SVM	0.565	18.37	0.835	1.15	0.832	1.47
ETR	0.567	18.33	0.836	1.15	0.860	1.35
RF	0.572	18.25	0.838	1.14	0.872	1.30
LSTM	0.736	14.59	0.872	1.30	0.868	1.32
CMIP6 dataset						
Mean	0.539	18.22	0.453	2.44	0.485	2.33
MLR	0.549	18.10	0.754	1.39	0.844	1.44
SVM	0.556	17.99	0.756	1.39	0.861	1.36
ETR	0.567	17.83	0.780	1.33	0.864	1.35
RF	0.577	17.68	0.781	1.33	0.864	1.35
LSTM	0.728	14.56	0.801	1.27	0.869	1.33

4.4.1 Performance Evaluation of MMEs in the case of precipitation

4.4.1.1 Performance evaluation of MMEs for daily rainfall

The results of performance evaluation on daily precipitation given in Table 4.13 indicate that the ML approaches have improved the performance of MMEs when compared with the mean ensemble approach. However, the improvements are not very significant for all ML methods except for LSTM. The MME developed using LSTM for the NEX-GDDP dataset could significantly improve the r value from 0.52 to 0.74 when compared to the mean ensemble technique. Similarly, a reduction in RMSE from 19.03 to 14.59 is also achieved by using LSTM for ensembling when compared to mean ensembling. Thus, the MMEs made using LSTM is performing significantly better for NEX-GDDP and CMIP6 datasets. The same is observed in the scatterplots of monthly precipitation given in Figure 4.26 and Figure 4.27 for NEX-GDDP and CMIP6 datasets respectively. The R^2 value

increased from 0.82 to 0.94 and 0.78 to 0.92 for LSTM ensemble when compared to mean ensemble for NEX-GDDP and CMIP6 datasets, respectively. Figure 4.28 and Figure 4.29 show the Taylor diagrams of observed and MME simulated monthly precipitation of NEX-GDDP and CMIP6 datasets, respectively for the validation period. These figures demonstrate that MME developed using the LSTM method match better with the observed data than MMEs developed using other methods.

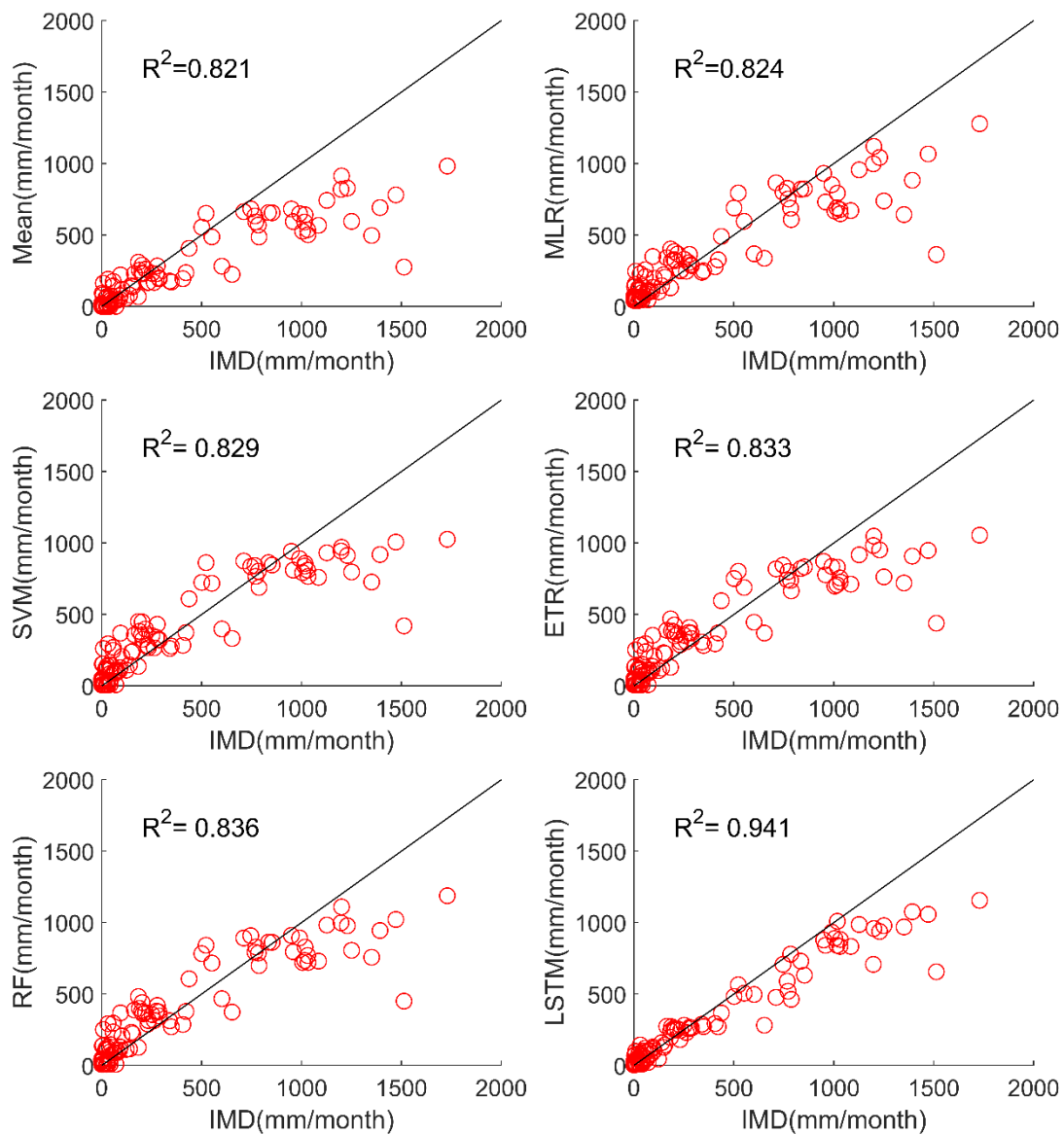


Figure 4.26 Scatter plot of observed and MME simulated monthly precipitation for NEX-GDDP dataset

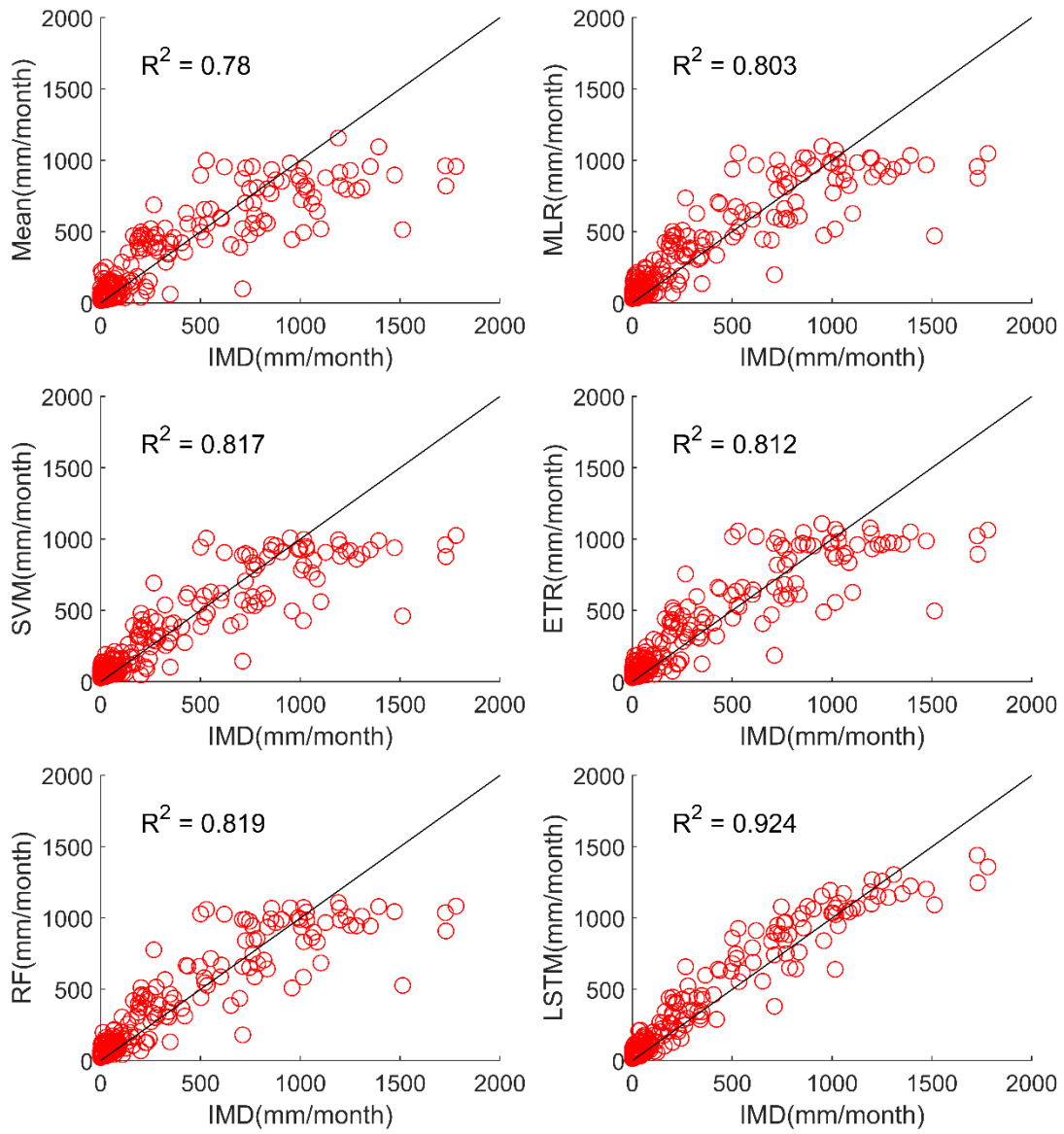


Figure 4.27 Scatter plot of observed and MME simulated monthly precipitation for CMIP6 dataset

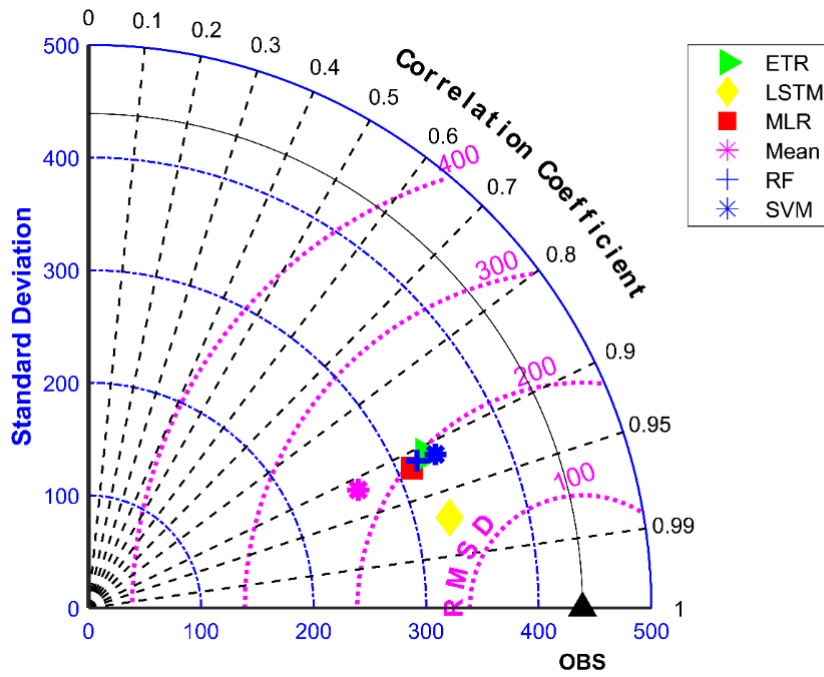


Figure 4.28 Taylor diagram of observed and MME simulated monthly precipitation of NEX-GDDP dataset during the validation period

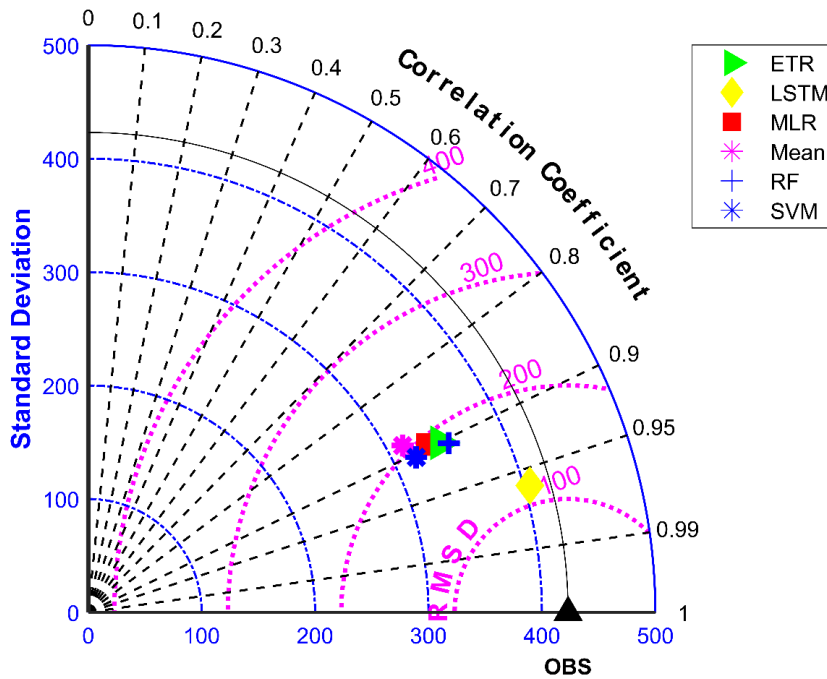


Figure 4.29 Taylor diagram of observed and MME simulated monthly precipitation of CMIP6 dataset during the validation period

4.4.1.2 Performance Evaluation of MMEs for monsoon season

The results of performance evaluation on daily precipitation of monsoon months (June to September) are given in Table 4.14. These results indicate that the ML approaches, namely, MLR, SVM, ETR and RF have shown very slight and insignificant improvement in the performance of MMEs when compared with the mean ensemble approach in the case of daily precipitation in monsoon months of NEX-GDDP and CMIP6 datasets. However, MME made using LSTM has shown significant improvement in the performance of daily monsoon rainfall in terms of r and RMSE. The MME developed using LSTM for the NEX-GDDP dataset could improve the r value from 0.038 to 0.386 when compared to mean ensemble technique. Similarly, a reduction in RMSE from 31.49 to 23.35 is also achieved by using the LSTM model. Similar improvements in r (0.031 to 0.357) and RMSE (29.26 to 23.33) were seen in the case of the CMIP6 dataset. Thus, the MMEs of monsoon precipitation made using LSTM are performing significantly better for NEX-GDDP and CMIP6 datasets. The same is observed in the scatterplots of monthly precipitation given in Figure 4.30 and Figure 4.31 for NEX-GDDP and CMIP6 datasets, respectively. The R^2 value increased from 0.506 to 0.81 and 0.366 to 0.788 for the LSTM ensemble when compared to the mean ensemble for NEX-GDDP and CMIP6 datasets, respectively. Figure 4.32 and Figure 4.33 show the Taylor diagrams of observed and MME simulated monthly monsoon precipitation of NEX-GDDP and CMIP6 datasets, respectively for the validation period. These figures demonstrate that MME of monsoon precipitation developed using the LSTM method match better with the observed data than MMEs developed using other methods.

Table 4.14 Performance of various MMEs in simulating monsoon P

Methods	Precipitation	
	r	RMSE (mm)
NEX-GDDP dataset		
Mean	0.038	31.49
MLR	0.042	30.25
SVM	0.053	30.08
ETR	0.065	29.89
RF	0.069	29.82
LSTM	0.386	23.35
CMIP6 dataset		
Mean	0.031	29.26
MLR	0.043	29.08
SVM	0.053	28.93
ETR	0.061	28.81
RF	0.061	28.82
LSTM	0.357	23.33

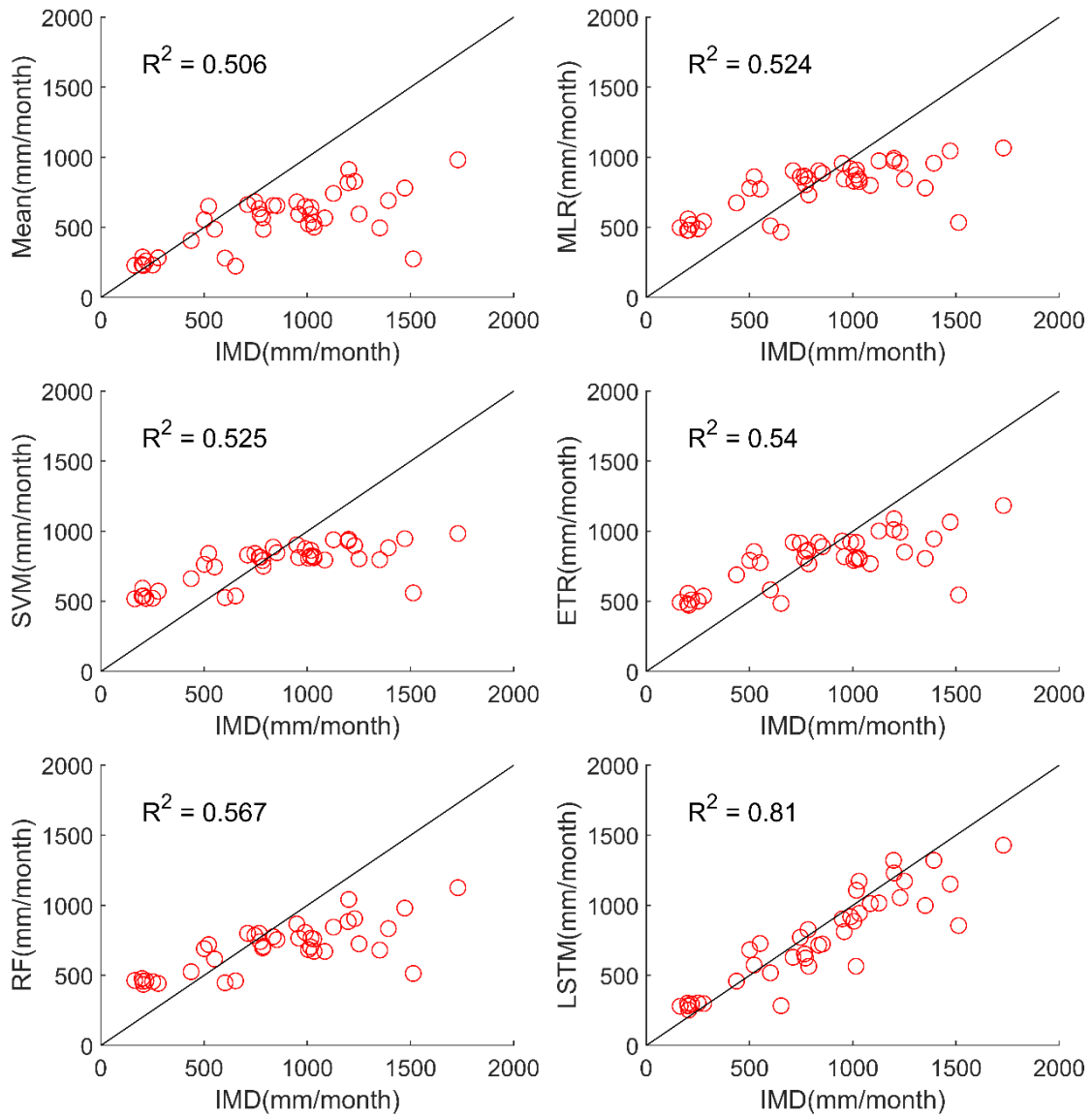


Figure 4.30 Scatter plot of observed and MME simulated monthly monsoon precipitation for NEX-GDDP dataset

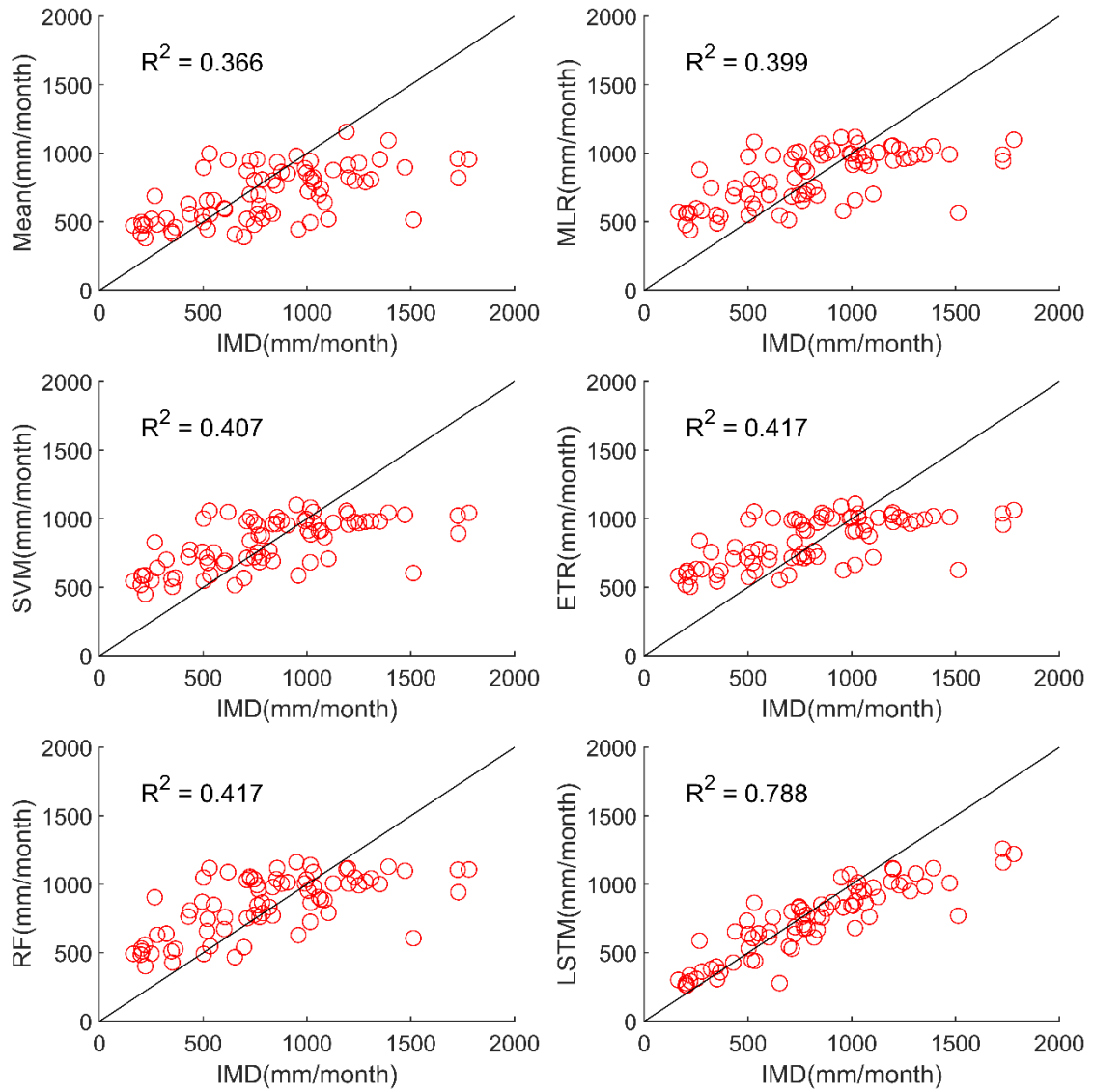


Figure 4.31 Scatter plot of observed and MME simulated monthly monsoon precipitation for CMIP6 dataset

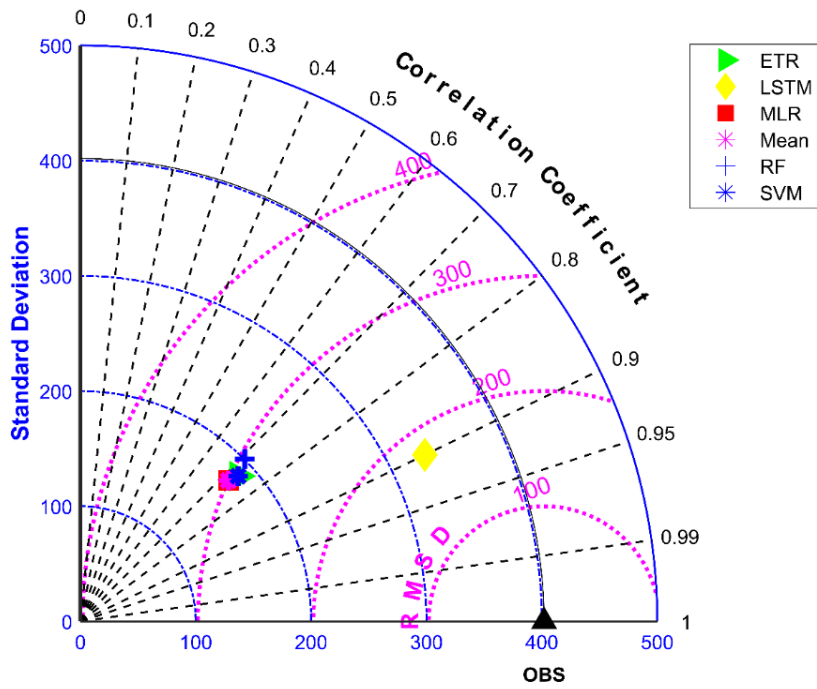


Figure 4.32 Taylor diagram of observed and MME simulated monthly monsoon precipitation of NEX-GDDP dataset during the validation period

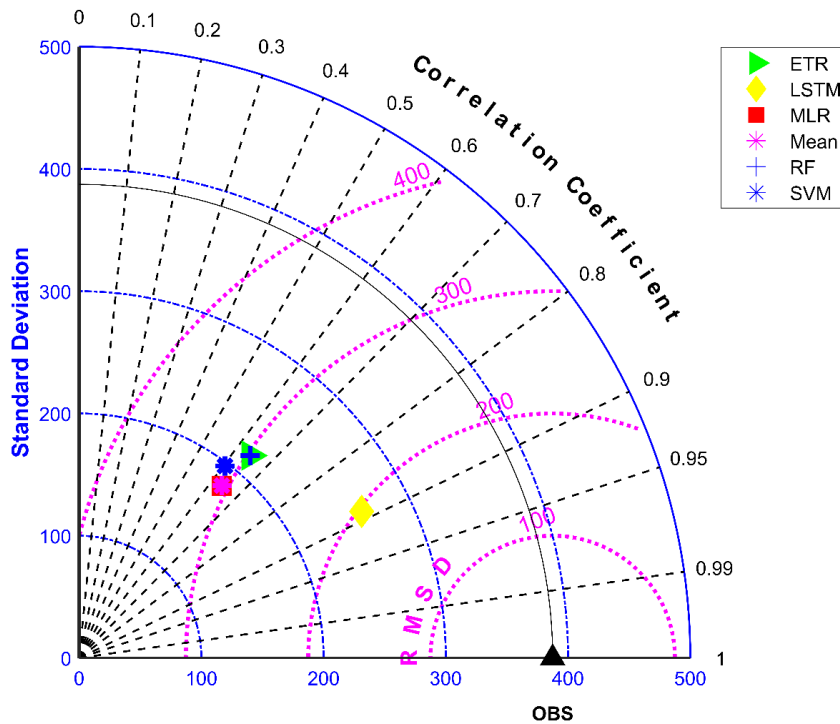


Figure 4.33 Taylor diagram of observed and MME simulated monthly monsoon precipitation of CMIP6 dataset during the validation period

4.4.2 Performance evaluation of MMEs in the case of maximum temperature

Table 4.13 reveals that all ML methods performed significantly better in simulating daily maximum temperature when compared to the ensemble mean approach. The MMEs developed for the NEX-GDDP dataset using MLR, SVM, ETR, RF and LSTM gave r values of 0.838, 0.832, 0.86, 0.872 and 0.868, respectively, while the mean ensemble gave a r value of 0.484. The MMEs made using LSTM and RF methods performed the best with RF slightly outperforming LSTM. Further, the MLR method slightly outperformed the SVM method. Figure 4.34 and Figure 4.35 shows the Taylor diagram and scatter plot of average monthly maximum temperature simulations of MMEs developed by different ensembling approaches against the reference dataset. These figures show the performance of MMEs developed by all ensembling methods is more or less the same on a monthly basis. In the case of the CMIP6 dataset, significant improvement is seen in the MMEs developed by ML methods when compared to the mean ensemble approach on a daily and monthly case. MME developed by the LSTM method performed the best with r value of 0.869 in the case of daily maximum temperature. The scatterplot (Figure 4.36) and Taylor diagram (Figure 4.37) show the better performance of all ML methods when compared to the mean ensemble approach.

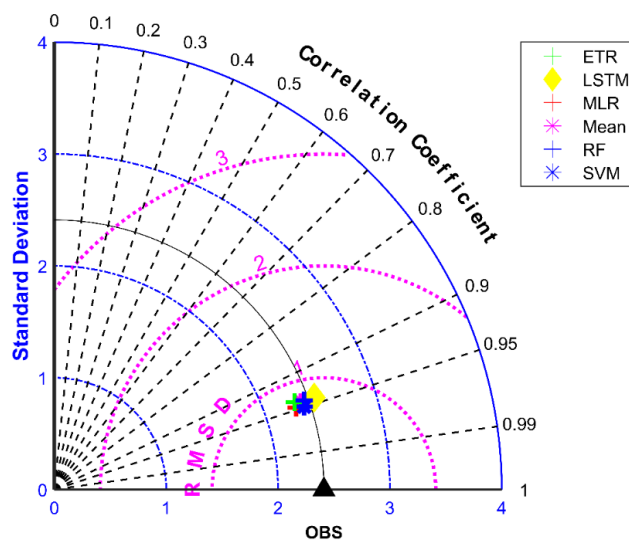


Figure 4.34 Taylor diagram of observed and MME simulated average monthly maximum temperature of NEX-GDDP dataset during the validation period

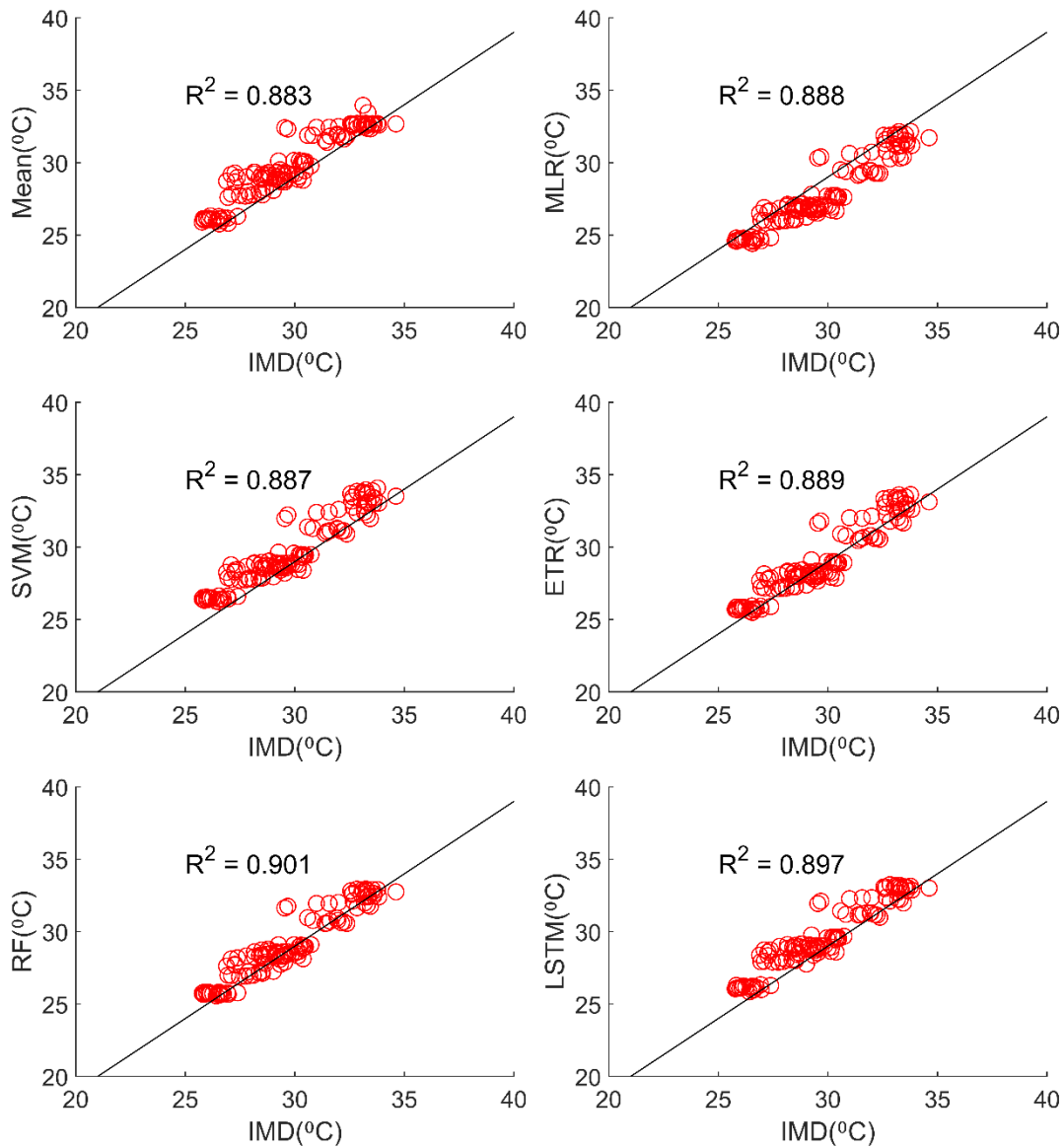


Figure 4.35 Scatter plot of observed and MME simulated average monthly maximum temperature for NEX-GDDP dataset

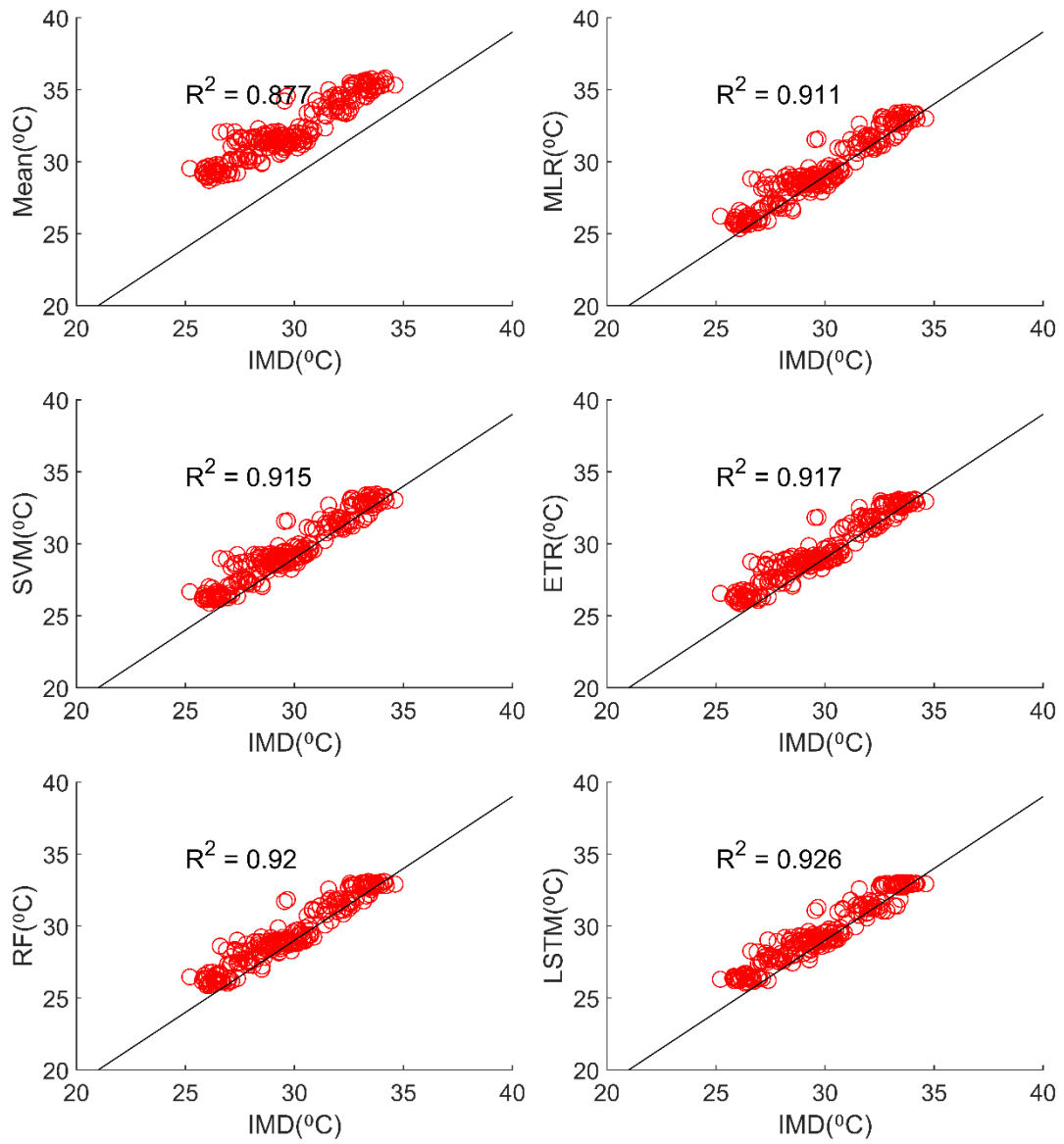


Figure 4.36 Scatter plot of observed and MME simulated average monthly maximum temperature for CMIP6 dataset

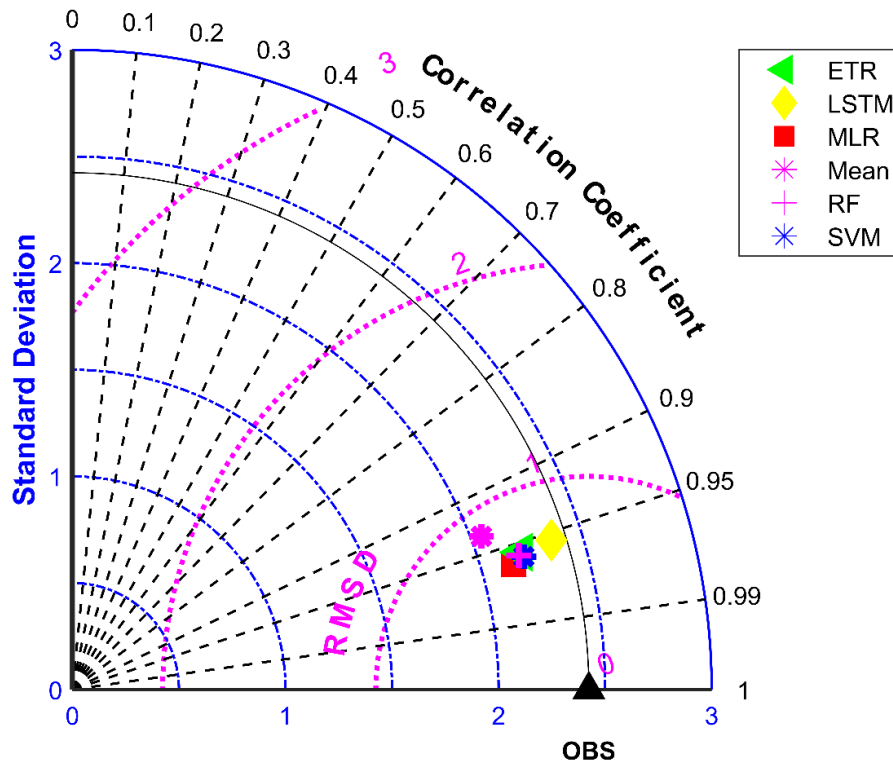


Figure 4.37 Taylor diagram of observed and MME simulated average monthly maximum temperature of CMIP6 dataset during the validation period

4.4.3 Performance evaluation of MMEs in the case of minimum temperature

All ML methods performed significantly better than mean ensembling methods in the case of minimum temperature in the case of NEX-GDDP and CMIP6 datasets. In the case of the NEX-GDDP dataset the r value improved from 0.522 to 0.872 when ML methods were used. A similar increase in r value was also observed for the CMIP6 dataset. When it came to the evaluation of the average monthly minimum temperature, no significant improvement is observed. This can be observed in the scatter plots and Taylor diagrams. Figure 4.38 and Figure 4.39 show the scatter plots of different MMEs of average monthly minimum temperature against the reference dataset for NEX-GDDP and CMIP6 datasets, respectively. Figure 4.40 and Figure 4.41 show the Taylor diagrams of various MMEs developed for average monthly minimum temperature. However, LSTM remained to be the best performing model in the case of minimum temperature, with r values of 0.872 and 0.801 for NEX-GDDP and CMIP6 datasets.

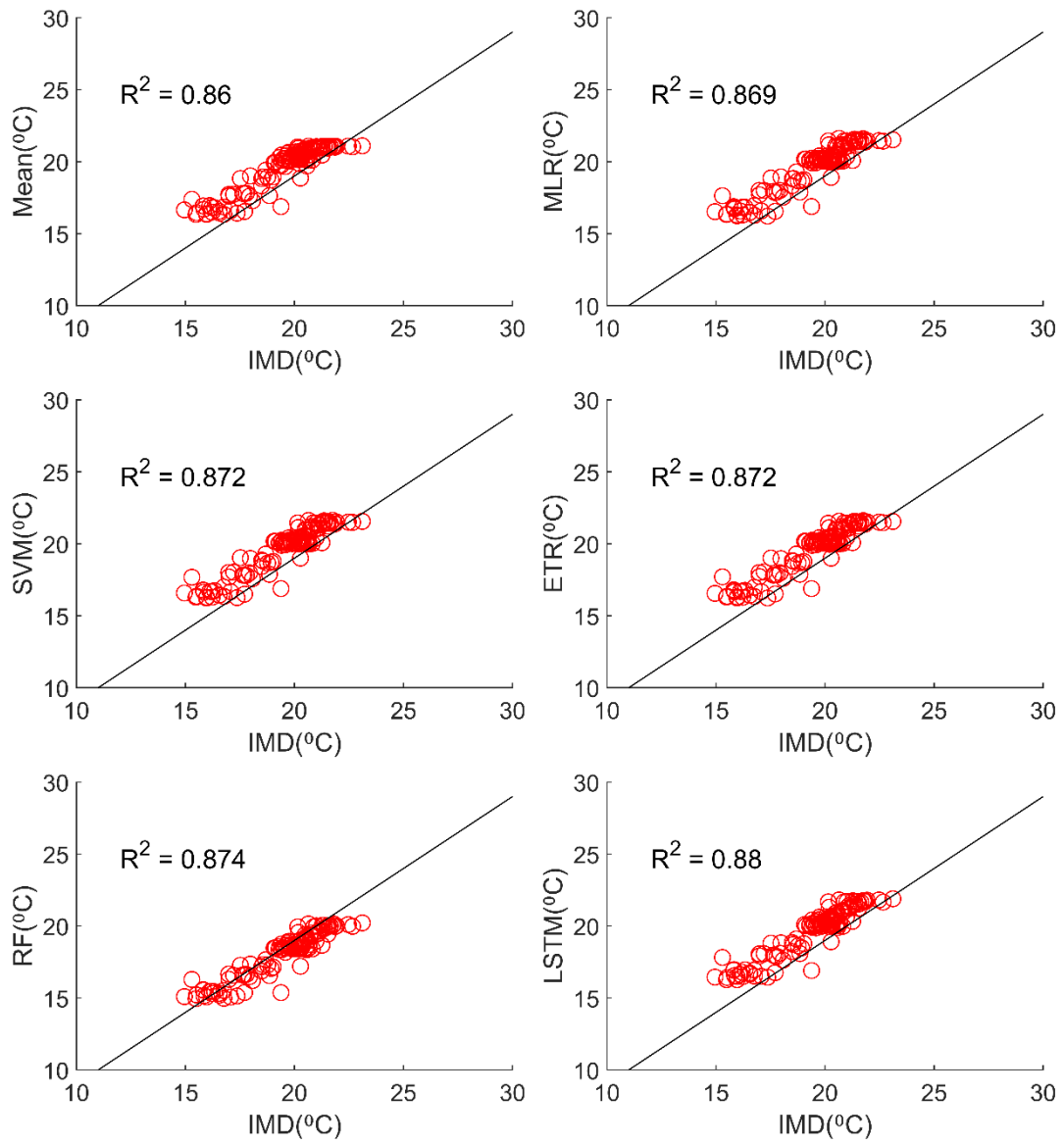


Figure 4.38 Scatter plot observed and MME simulated average monthly minimum temperature for NEX-GDDP dataset

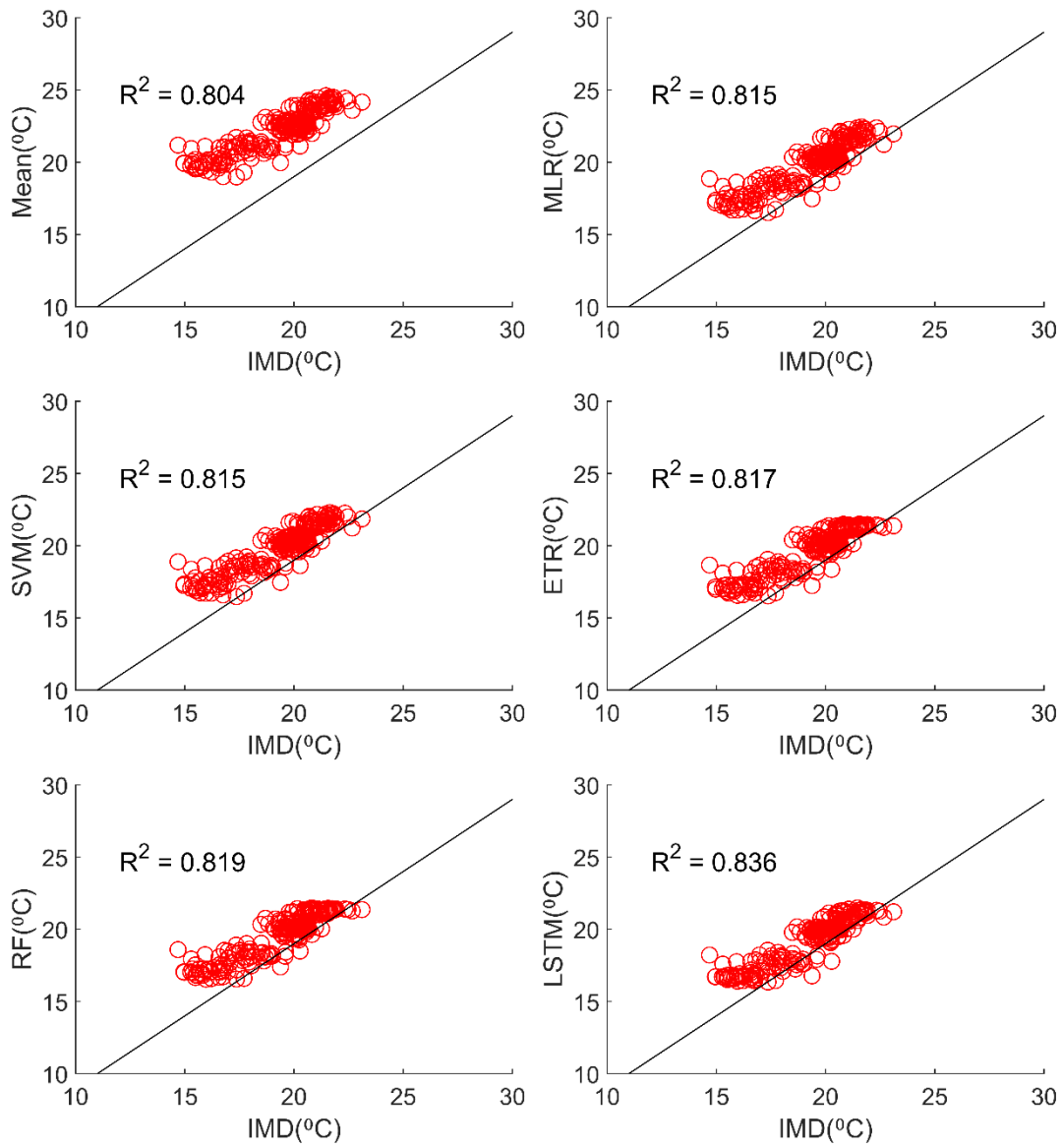


Figure 4.39 Scatter plot of observed and MME simulated average monthly minimum temperature for CMIP6 dataset

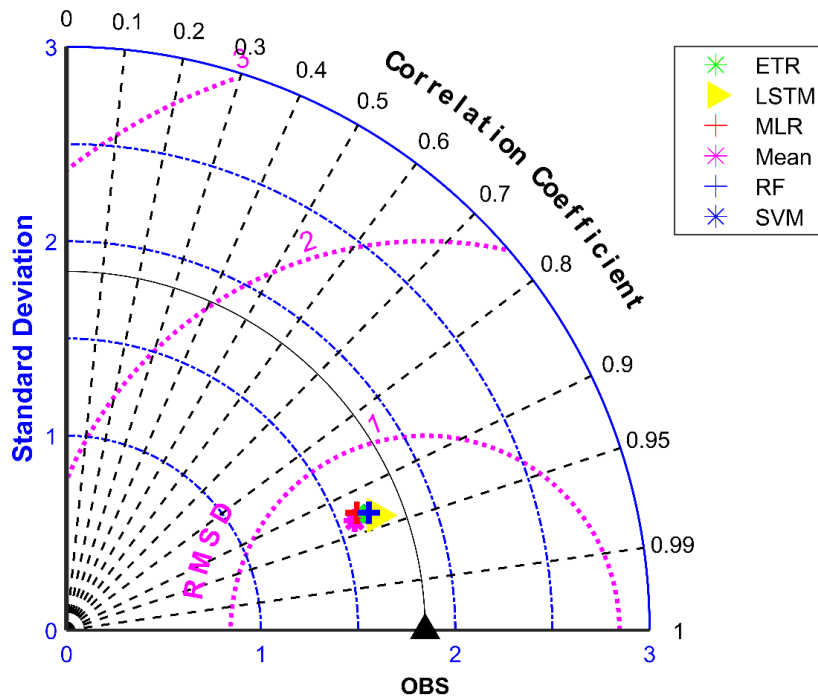


Figure 4.40 Taylor diagram of observed and MME simulated average monthly minimum temperature of NEX-GDDP dataset during the validation period

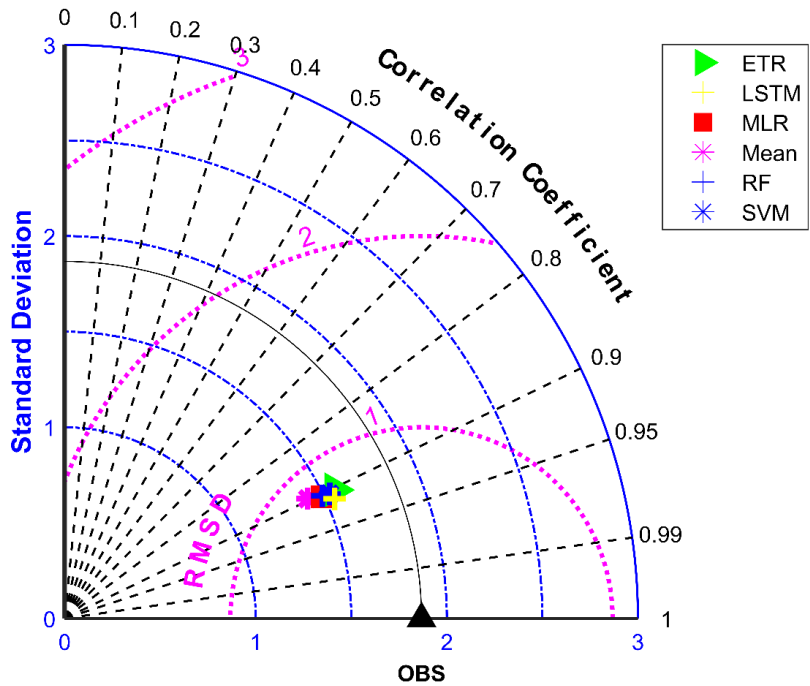


Figure 4.41 Taylor diagram of observed and MME simulated average monthly minimum temperature of CMIP6 dataset during the validation period

4.4.4 Inter-comparisons of performance of different MMEs

Different approaches like mean, regression models (i.e., SVM and MLR), ensemble learning models (i.e., ETR and RF), and deep learning time series model (i.e., multivariate LSTM) are used to create MMEs for 21 NEX-GDDP models and 13 CMIP6 models outputs for P, T_{min} and T_{max}. In the case of precipitation, LSTM significantly outperformed all the other MME approaches with r values of 0.74 and 0.73 for NEX-GDDP and CMIP6 datasets, respectively. The performance of all the other MME approaches was more or less the same, with r values in the range of 0.519 to 0.577. Similarly, MMEs of LSTM gave R² of 0.94 and 0.92 in the case of NEX-GDDP and CMIP6 datasets for monthly precipitation. The study done explicitly for monsoon rainfall shows that all methods except LSTM failed in giving a good performance of MMEs. This shows that the LSTM method to an extent is successful in predicting rainfall magnitude in monsoon months. Hence, this study reveals the superiority of LSTM compared to other methods in ensembling monsoon precipitation.

However, in the case of temperature, all ML approaches performed equally good when compared to the mean ensembling approach. All ML methods could improve the r value from 0.5 to a range of 0.8 in the case of temperature. In the case of the maximum temperature of the NEX-GDDP dataset, the MME made with RF (r=0.872) slightly outperformed LSTM (r=0.868). In all the other cases, all ML methods performed equally well, with LSTM showing a slightly increased performance. The same pattern was observed in all the grid points in the basin. Ensemble learning models like RF and ETR also performed well in the basin in the case of maximum and minimum temperature. They outperformed MLR and SVM in all the cases. Hence, MMEs developed through LSTM, RF and ETR algorithms are recommended for creating MMEs in the basin. In general, all ML methods performed better than the mean ensemble approach. This is seen in other studies like that of Ahmed et al. (2020).

4.5 LULC CHANGE DETECTION AND PREDICTION

4.5.1 Classification in GEE

In order to investigate the effect of auxiliary data on LULC accuracy, four different scenarios were considered. These four scenarios were used for SVM and RF classifiers to identify the best classification scenario and the best classifier. Thus, eight classification models were set up. The results of these models for the year 2020 are shown in Table 4.15 in terms of Kappa coefficient (κ) and overall accuracy (OA). Scenario 4 was identified as

the best classification scenario. Thus, this scenario was used for the classification for all the other years. The addition of topographic features to classification has shown significant improvement in accuracy indicating its importance as a feature in classification. This could be because the Netravati basin is dominated by forest areas at high elevations and slopes, while lower elevations are dominant with built-up and agriculture. Many other studies have also observed topographic features as an important auxiliary variable (Hurskainen et al. 2019). The inclusion of spectral indices enhances and differentiates different LULC classes during the classification process, thus improving the classification accuracy. The same was observed by Kobayashi et al. (2020) and Parthasarathy and Deka (2021).

Table 4.15 Accuracy results for each modelling scenario

Year: 2020	RF		SVM	
	OA	κ	OA	κ
Scenario 1 (Spectral reflectance values)	86.03	83.9	81.27	79.77
Scenario 2 (Spectral reflectance values + spectral indices)	86.67	84.1	81.95	76.14
Scenario 3 (Spectral reflectance values + topographic features)	88.73	84.63	82.01	78.11
Scenario 4 (Spectral reflectance values + spectral indices + topographic features)	89.87	86.51	84.43	79.65

The LULC for 1990, 2000, 2010 and 2020 were classified using RF and SVM in GEE. In spectral categories that are almost equal, like barren land and urban areas, the RF performed better than the SVM. As a result, further analysis was performed using the RF algorithm-based classification maps. Table 4.16 displays the RF and SVM algorithm's overall accuracy (OA) and Kappa coefficient (κ) results for each year.

Table 4.16 Comparison of κ and OA for SVM and RF

Year	SVM		RF	
	OA	κ	OA	κ
1990	86.25	81.57	89.74	86.1
2000	78.42	71.24	88.42	84.7
2010	82.6	77.41	89.12	85.1
2020	84.43	79.65	89.87	86.51

Figure 4.42 shows the percentage change in areas under each class over the historical period. The results of the analysis show a decreasing trend in forest and barren areas. In contrast, an increasing trend is seen in the case of built-up areas. According to the analysis, between 1990 and 2020, the amount of forest (56% to 51.22%) and barren land (6.8% to 4.99%) decreased. In contrast, the agricultural and urban area has shown an increasing pattern with the percentage increase from 32.42% and 3.29% to 37% and 5.07%, respectively. The area of water remained moreover the same. The significant changes in the basin are the increase in agricultural and urban developments and the decrease in forests. This suggests that there has been extensive deforestation of the basin's natural vegetation. There have been numerous reports of urban settlements following the conversion of forests to grasslands and agricultural regions in the Western Ghats (Kale et al. 2016; Sinha and Eldho 2018). Figure 4.43 shows the LULC maps generated using RF on using scenario 4 for the historical period.

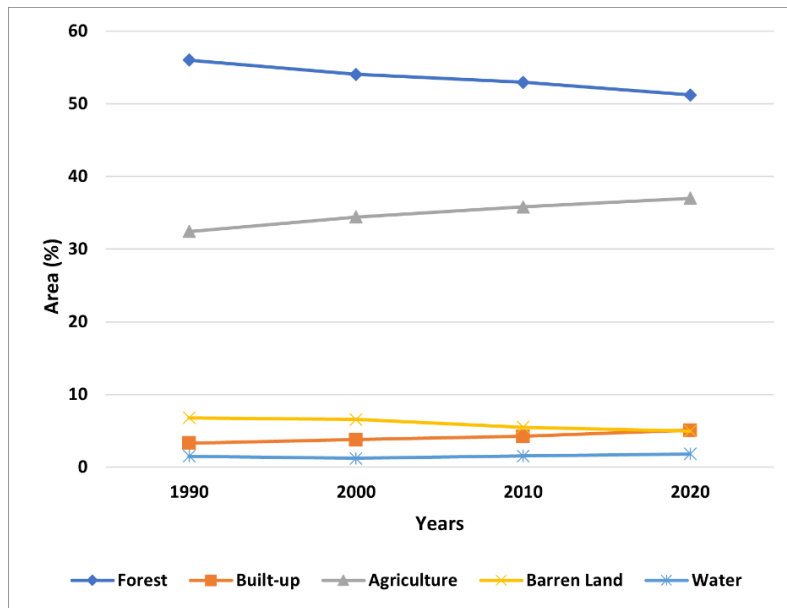


Figure 4.42 Graphical representation of percentage change in the LULC classes from 1990 to 2020

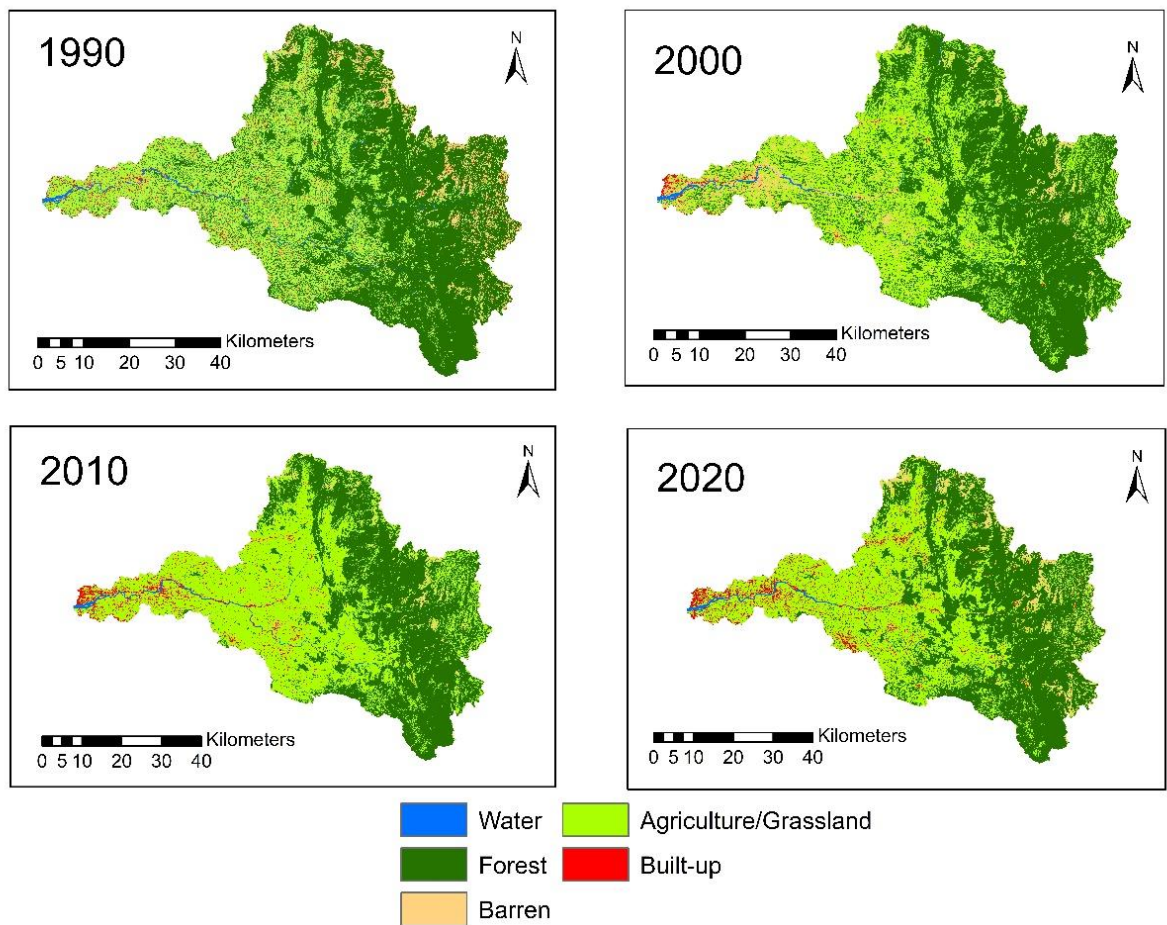


Figure 4.43 LULC classification using RF

4.5.2 Prediction of future LULC using TerrSet

The classified maps based on the RF algorithm are then utilised to predict the LULC change in 2050, 2075, and 2100 using CA–Markov analysis in LCM. The drivers utilised for LULC prediction included distance to road, distance to forest, distance to river, distance to built-up area, slope, and DEM (Figure 4.44). When utilised with transition potential maps, Cramer's V for distance to built-up and road distance is greater than 0.6, confirming the strong dependability of two layers. Distance to built-up and road distance are directly related to the LULC change. The topographic elements, elevation and slope have impact on LULC change. The extent to which forests and barren land are converted to agricultural land and cities, are all influenced by topography. Additionally, it is also seen that deforestation is inversely proportional to slope. Other elements that influence land use change include distance from rivers, inhabited areas, and roads since they make it easier for people to get essentials.

Table 4.17 Cramer's V for each driver variable

Driver Variables	Cramer's V
Slope	0.3895
DEM	0.5726
Distance to river	0.5632
Distance to road	0.6128
Distance to built-up	0.6236
Distance to forest	0.3875

The LULC of 2020 was projected using the LULC of 2000 and 2010. The projected map for the year 2020 was compared to the actual map for validation. With a κ of 84.89 percent, it was seen that the projected and classified images of 2020 are in good agreement. Figure 4.45 shows the graphical distribution of changes in areas in each LULC class in percentages. Figure 4.46 shows the LULC maps predicted using TerrSet. The area of built-up is expected to increase to 16.8% by the year 2100. In contrast, a drop in forest and barren land is expected. The urban area would expand at the cost of forest and agriculture/grassland in the future. Table 4.18 shows the percentage change in the LULC classes from 1990 to 2100 (historical and projected changes). Hence a study on the effect of LULC changes over the basin in terms of surface runoff is essential. The results of such a study are given in the next section.

Table 4.18 Area (%) of each LULC class

Years→									
LULC class↓	1990	2000	2010	2020	2030	2040	2050	2075	2100
Forest	56	54.05	52.96	51.22	49.01	47.22	46.27	43.17	39.9
Built-up	3.29	3.77	4.24	5.07	6.96	8.14	9.3	13.92	16.8
Agriculture	32.42	34.43	35.8	37	37.3	37.8	38.1	36.4	36.7
Barren Land	6.8	6.54	5.48	4.99	4.75	4.64	4.32	4.2	3.9
Water	1.49	1.21	1.52	1.81	1.98	2.19	2.21	2.31	2.7

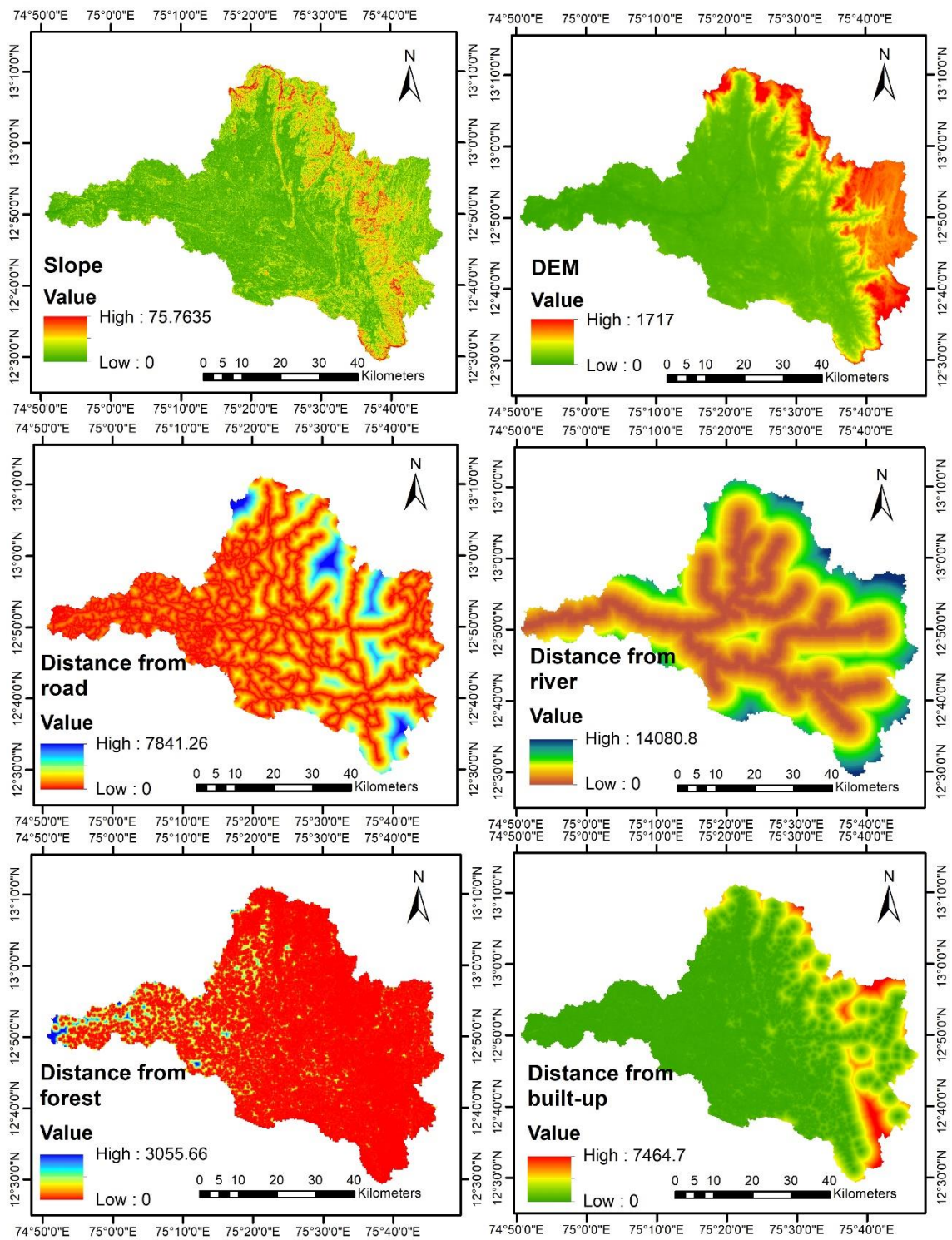


Figure 4.44 Driver variables for the CA-Markov model

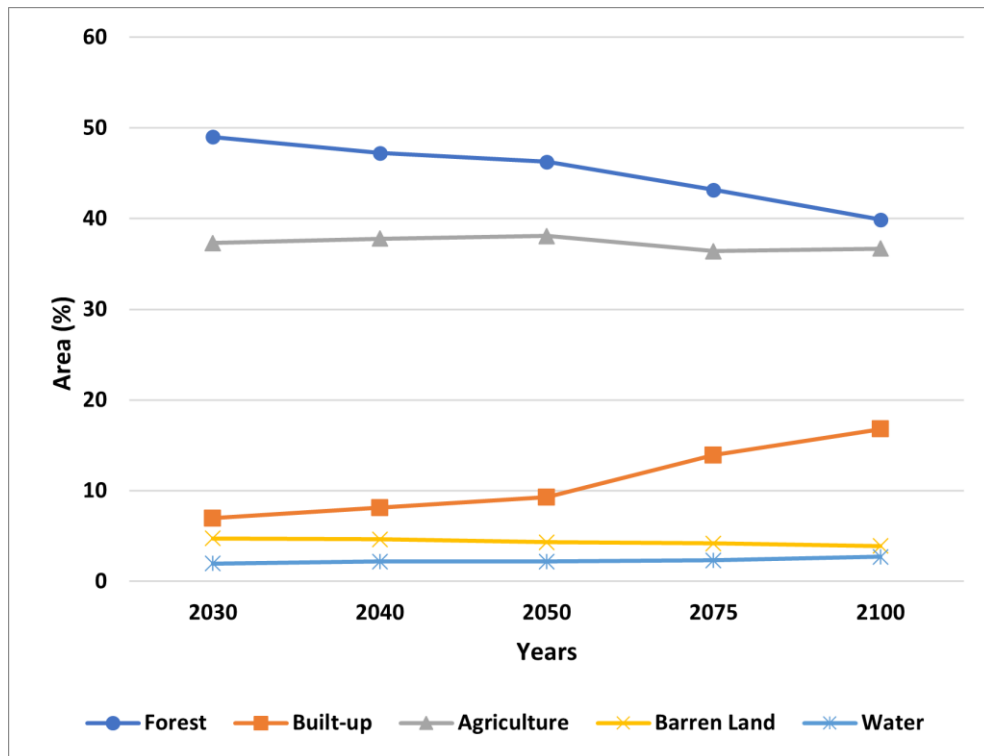


Figure 4.45 Graphical representation of percentage change in the LULC classes from 2020 to 2100

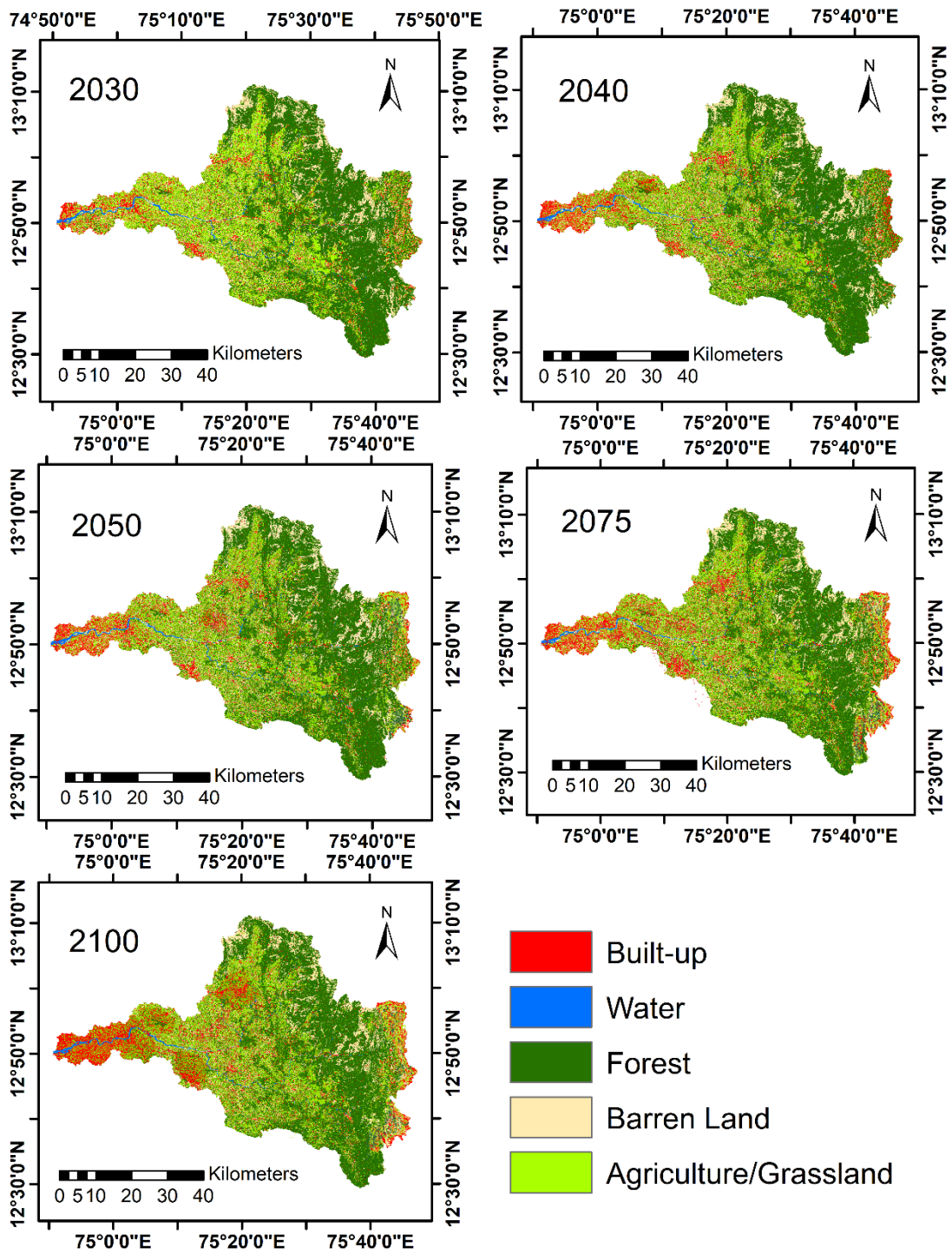


Figure 4.46 Predicted LULC for the years 2030, 2040, 2050, 2075 and 2100

4.5.3 Discussion

In this work, we investigated the impact of two GEE auxiliary features on LULC classification accuracy. This demonstrated that auxiliary information, such as topographic characteristics and various remote sensing indices, can enhance classification accuracy. In the year 2020, the OA of the RF method improved from 86.03 percent to 89.87 percent.

GEE offers a robust scripting language that functions in conjunction with its user-friendly Application Programming Interface (API) and cloud architecture. It helped with the effective study of the ML-based classification. According to the analysis, the RF algorithm performed more accurately than the SVM model. This shows that the RF method outperforms the other model when dealing with multi-class classification.

The LCM module of the CA-Markov model of the Idrisi TerrSet software uses the ML application to analyse the spatio-temporal change prediction of the LULC. With a κ value of 84.89 percent, it is seen that the anticipated map of 2020 and the classification image of 2019 correspond quite well. The magnitudes and directions of LULC conversion are mainly for forest to grassland/agriculture, grassland to agriculture/urban, and agriculture to the urban area at the river basin scale. The expected percentage change of the forest and grassland is decreasing while built-up is expected to increase. This indicates that agriculture and urban area are expanding, while forest/grassland is declining and the same trend may continue in future also.

4.6 HYDROLOGICAL MODELLING USING SWAT

The SWAT model was calibrated and validated for the historical period and the most sensitive parameters were obtained from SWAT-CUP. The model was run from 1990 to 2010 and was used as calibration period and the rest was used as validation period. The validated model gave NSE and R^2 values of 0.78 and 0.77, respectively. Figure 4.47 shows the plot of observed and simulated streamflow during the validation period. Table 4.19 shows the results of the sensitivity analysis. Soil Conservation Service (SCS) runoff curve number and baseflow alpha factor were ranked as the most sensitive parameters. The same was observed by Sinha and Eldho (2018). The impact of LULC and climate change was then evaluated using this calibrated model.

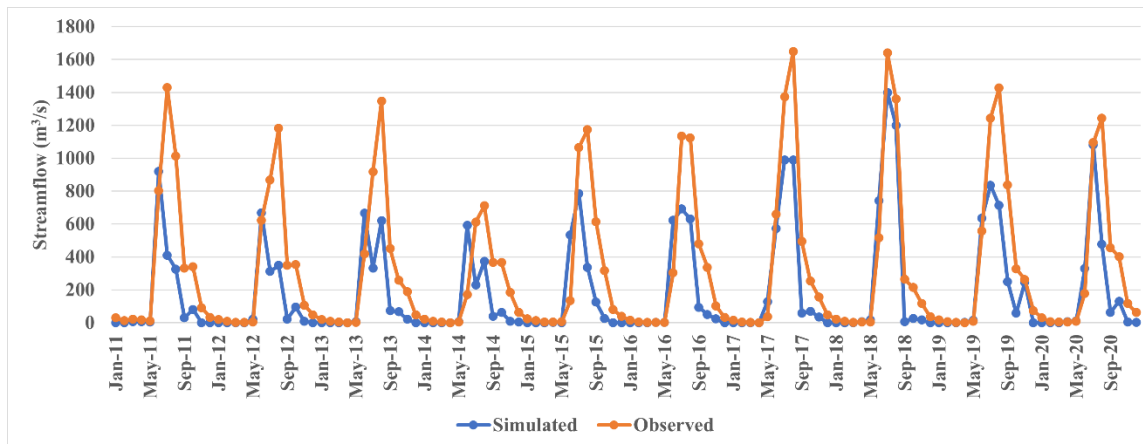


Figure 4.47 Observed and simulated monthly streamflow in the validation period at Bantwal gauging station

Table 4.19 Parameters and ranges used in the sensitivity analysis and ranking

Rank	Parameter Definition	Fitted Value	Minimum Value	Maximum Value
1	SCS runoff curve number for moisture condition II*	0.07 (r)	0.07	0.09
2	Baseflow alpha factor (days)	0.32 (v)	0.30	0.50
3	Groundwater delay (days)	31.12 (v)	30.00	32.00
4	Threshold depth of water in the shallow aquifer for return flow to occur (mm)	2.65 (v)	2.60	2.80
5	Available water capacity (mm/mm soil)	0.26 (v)	0.10	0.30
6	Plant evaporation compensation factor	0.20 (v)	0.20	0.30
7	Plant uptake compensation factor	0.28 (v)	0.20	0.30
8	Groundwater “revap” coefficient	0.07 (v)	0.07	0.08
9	Surface runoff lag coefficient	0.20 (v)	0.19	0.21
10	Groundwater recharge to deep aquifer (fraction)	0.60 (v)	0.59	0.64

(r) : Existing value to be multiplied, (v) : Existing value to be replaced by given value

Percentage change in annual streamflow by keeping LULC constant and climate varied for near, mid and far future period compared to the baseline period (1990-2020) is shown in Table 4.20. The results show a decrease in annual streamflow for all climate scenarios

when compared to the baseline. For instance, in the case of RCP 4.5, a decrease of 14.28% of streamflow is expected from 2075 to 2100 when compared to the historical period 1990 to 2020. The change is more prominent in the near future than far future. This is due to the increasing trend in rainfall from near to far future scenarios. This is observed in all the six scenarios considered.

Table 4.20 Percentage change in streamflow due to climate change

Scenario (LULC:2020)	Near (2020-2050)	Mid (2050-2075)	Far (2075-2100)
RCP 4.5	-17.75	-15.33	-14.28
RCP 8.5	-22.32	-20.16	-17.38
SSP126	-16.71	-13.06	-9.18
SSP245	-18.76	-16.99	-14.31
SSP370	-20.01	-19.9	-18.67
SSP585	-21.33	-20.06	-16.32

The expected impact of future LULC by keeping the climate constant at baseline is given in Table 4.21. In contrast to the climate change effect, an increase in streamflow is seen in predicted LULC scenarios when compared to the baseline. An increase of 13.41% is expected due to LULC change by the year 2100 when compared to the year 2020. This is attributed to the increase in built-up and decrease of forest in the basin. Hence, due to the increased runoff and decreased percolation, higher streamflow is expected.

Table 4.21 Percentage change in streamflow due to LULC change

Scenario (Climate:1990 to 2020)	2050	2075	2100
Streamflow (% increase)	5.03	9.22	13.41

The effect of climate change on streamflow is more compared to LULC change is observed in this study. Due to the increase in temperature due to increase in GHG concentration, higher evapotranspiration is expected. Hence, a reduction in streamflow is expected due to temperature increase. However, the rainfall pattern can be erratic with heavy downpours causing floods and scarce rainfall causing droughts may be expected even without much change in average annual precipitation.

The combined impacts of LULC and climate change on streamflow when compared to the baseline are given in Table 4.22. As the time progresses and reaches 2075 to 2100, the streamflow reduction is nullified due to the increase in streamflow due to the LULC change. The extreme scenarios RCP 8.5 and SSP585 show a 17.34% and 16.35% reduction in the near future when combined with LULC of 2050. The idealised scenario, i.e., SSP126, shows a reduction of 11.73% in the near future and an increase of 3.92% in the far future with LULC of 2050 and 2100, respectively. Intermediate scenarios also show a reduction in streamflow when combined with projected LULC maps. Hence, an overall reduction in streamflow is expected, especially in the near future. Similar results were observed by Sinha et al. (2020) in the Kadalundi river basin, Western Ghats.

Table 4.22 Percentage change in streamflow due to LULC change and climate change

Scenarios	Near LULC:2050	Mid LULC:2075	Far LULC:2100
RCP 4.5	-12.77	-6.21	-1.18
RCP 8.5	-17.34	-11.04	-4.28
SSP126	-11.73	-3.94	3.92
SSP245	-13.78	-7.87	-1.21
SSP370	-15.03	-10.78	-5.57
SSP585	-16.35	-10.94	-3.22

SUMMARY AND CONCLUSIONS

5.1 SUMMARY AND CONCLUSIONS

5.1.1 Bias correction

5.1.1.1 Bias correction of rainfall

For hydrological impact studies, robust projections of precipitation variability and change at regional scales are necessary. Recent advancements in computing power have enabled climate models to simulate more processes in detail and on a finer scale. In this study, an attempt has been made to assess the performance of one such GCM simulated precipitation data. The frequency, intensity and distribution of rainfall are important factors of precipitation.

A novel BC method which attempts to correct the frequency, intensity and distribution of precipitation obtained from the GCM is used. The performance of the BC method was analysed using a cross-validation approach with various performance indicators like NSE, r , RMSE, MAE, R^2 and PBIAS. An increase in NSE and R^2 from 0.66 to 0.75 and 0.69 to 0.79 was observed after bias correction. MAE and PBIAS decreased from 138.62 to 59.62 and 15.42 to 6.61, respectively. Hence, the following conclusion can be made:

- The new methodology used in the study to correct the frequency, intensity and distribution of rainfall has significantly improved the predictions of GCM by improving the PBIAS from 59.62 to 6.61.

Although the study demonstrated the improvement in the distribution patterns of precipitation when BC is applied, it did not give particular emphasis on the precipitation extremes. Hence, a future study could assess the performance of BC in terms of extreme precipitation events. This can improve the reliability of data when used for climate impact studies.

5.1.1.2 Bias correction of temperature

Robust projections of temperature variability and change, particularly at regional scales, are necessary for impact studies. Recent advancements in computing power have enabled climate models to simulate more processes in detail and on a finer scale. In this study, an attempt has been made to improve the performance of one such GCM simulated temperature data. The GCM simulations are improved by using six bias correction techniques. The performance evaluation of each bias correction technique was done in order to find the best-performing methods for the given data and study area. The performance of each bias correction method was analysed using a two-sample cross-validation approach with various performance indicators. The bias corrected GCM data, along with observed data, are further used for analysing the trend of seasonal and annual maximum and minimum temperature in the basin.

A bias correction method must be chosen based on the purpose of bias corrected outputs. Some bias correction methods, namely quantile mapping has the ability to improve the statistics and distribution of variables but may disrupt the temporal sequence. Whereas other simple methods may not correct the distribution but may preserve the temporal sequence. Hence, the findings from the study emphasise the necessity of comparison of available BC methods before choosing a suitable bias correction for a given study area, GCM and application.

The following are key conclusions from this study:

- The study revealed that bias-correction techniques could improve the simulated temperature data in the basin. A significant decrease of around 50% and 80% was observed in the bias of the uncorrected data when the corrections were applied.

- The performance evaluation indicated that delta correction, empirical quantile mapping, adjusted quantile mapping, Gamma-Pareto quantile mapping and quantile delta mapping method could equally well improve the predictions of GCM. This shows that simple bias correction techniques like the delta change method are found to be useful. However, the Linear scaling method did not perform well, preventing its use in the study area.

5.1.2 Ranking of GCMs

This study focused on the evaluation of the performance of 21 GCMs given by the NEX-GDDP dataset and 13 CMIP6 GCMs in simulating precipitation, maximum temperature and minimum temperature. Their performance was evaluated through RMSE, SS and r. The range of values of RMSE, r and SS for different GCMs indicated that they could reasonably simulate the climate variables in the selected basin.

The performance of GCMs for each indicator was not the same. Thus, it is essential to consider multiple criteria for the assessment of GCMs. Suitable weights were calculated for these indicators through the entropy method after the normalization of indicators. The entropy method gave unbiased weights to the indicator, which is objective. Based on the indicators and the weights assigned to them, the rank of each GCM was calculated using TOPSIS, VIKOR, weighted average and PROMETHEE-II. Group ranking was employed to find the top-ranked GCMs for each grid by considering the 4 MCDM methods and for the whole basin. Following are the two major conclusions from the study:

- The best GCMs for the entire basin were found to be MIROC-ESM-CHEM for precipitation and IPSL-CM5ALR for temperature in the case of the NEX-GDDP dataset.
- BCC-CSM2-MR was seen as the best GCM for precipitation, while INM-CM5-0 and MPI-ESM1-2-HR were found to be the best for minimum and maximum temperature, respectively, in the basin for the CMIP6 dataset.

The top-ranked GCMs for the basin can be used for creating an ensemble of GCMs for the basin for further studies. The results of the study can be used for impact assessments of

climate variables in the basin. The methodology used in this study can be applied to any other basin. The authors suggest basin-scale performance evaluation of GCMs before choosing a particular GCM for impact assessment studies.

5.1.3 Ensembling of GCMs

In this study, an attempt has been made to evaluate the performance of MMEs developed using six ensembling methods. These ensembling techniques include simple statistical technique (mean), regression models (i.e., SVM and MLR), ensemble learning models (i.e., ETR and RF), and deep learning time series model (i.e., LSTM). The performance evaluation of each ensembling technique was done in order to find the best-performing MMEs of 21 NEX-GDDP and 13 CMIP6 GCMs in the Netravati basin. This comparison shows that the application of an LSTM model for climate model ensemble prediction performs significantly better than the benchmark models, including other ML techniques and mean ensembling techniques in the case of precipitation. It gave a coefficient of determination of 0.94 and 0.92 in the case of NEX-GDDP and CMIP6 monthly precipitation datasets, respectively. The MME of the LSTM method could simulate the monsoon rainfall magnitude satisfactorily when compared to all the other methods. Hence, LSTM deep learning models are seen to be an attractive approach for climate data prediction. This could be because of its capability to learn long-term dependencies in observed data, which leads to better prediction results that outperform several alternative ML and statistical approaches. In the case of temperature, all the ML methods showed equally good performance, with RF and LSTM performing consistently well in all the cases of temperature. The coefficient of determination in the range of 0.9 and 0.8 are observed for MMEs developed using RF and LSTM techniques in the case of monthly average maximum and minimum temperature, respectively. Hence, based on this study, RF and LSTM are recommended for the creation of MMEs in the basin. In general, all ML approaches performed better than the mean ensemble approach. However, this study limits its scope to ML methods and does not analyse its performance on extreme values. Hence, a future study which analyses its effectiveness on extreme values may be done. Further, other multi-model combinations like triple collocation and Bayesian approaches may be

explored in the future. Thus, based on the present study, the following specific conclusions may be drawn:

- The inter-comparison of MMEs developed using mean, SVM, MLR, ETR, RF and LSTM show that ML-based MMEs perform better than the mean ensemble approach. Therefore, ML methods are recommended for the creation of MMEs of climate data in future studies.
- A time series model like LSTM could be a good choice for the creation of MMEs. Hence, more studies which explore the usage of time series/sequential models for the creation of MMEs may be done in the future.

5.1.4 LULC change detection and prediction

In this work, we investigated the effect of two auxiliary features, i.e., multiple remote sensing indices and topographic features, on the accuracy of LULC classification and revealed that auxiliary features could improve the OA of classification. The OA of the RF method increased from 86.03% to 89.87% in the year 2020 with the usage of auxiliary features. The comparison of SVM and RF classifier revealed that RF had outperformed SVM in terms of accuracy. Hence, RF is recommended for classification over SVM. Further, CA–Markov model of LCM module in Idrisi TerrSet software is an effective tool in predicting the spatio-temporal change projection of the LULC. It is found that the projected and classified images of 2020 are in good agreement. The LULC analysis shows a decline in forest area and an increase in the urban area, and the same trend is expected in the future.

Thus, based on this objective, the following specific conclusions may be drawn:

1. The use of auxiliary data like topography and spectral indices can increase the classification accuracy.
2. The RF classifier performed better than the SVM classifier in the basin
3. The pattern of LULC change shows a significant increase in built-up and a decrease in the forest.

5.1.5 Hydrological modelling using SWAT

Hydrological modelling using SWAT was performed to study and predict the impacts of LULC and climate on streamflow. The SWAT-CUP was used for calibration, validation and sensitivity analysis to get an NSE of 0.77 during validation. The calibrated SWAT model was further used to study the future impacts of LULC and climate change. From the results of the SWAT analysis the following key conclusions are made:

- The annual streamflow for all future climate scenarios is expected to decrease when compared to the historical baseline period.
- In contrast streamflow is expected to increase due to the predicted LULC change by 13.41% by 2100. This increase is due to the increase in built-up area in the basin. Hence groundwater recharge is anticipated to be decreased.
- The effect of climate change on streamflow is more compared to LULC change. Hence reduction in streamflow is predicted for the Netravati catchment, combining the effects of LULC and climate change.

These findings call for the requirement of conservation measures for the available water. The study thus highlights the need to modify the catchment level infrastructure and conservation of water resources in light of climate and LULC change.

5.2 LIMITATION OF THE STUDY

1. The bias corrections methods used in the study could not efficiently correct the extreme values of climate variables.
2. The LULC change prediction model has not considered drivers representing economic growth and agricultural practices.
3. Only two LULC maps serve as the base for the prediction of future LULC in CA-Markov model.
4. The SWAT model was calibrated using a single gauging station data. Multi-gauge calibration would increase the reliability of the model.

5. The study has not concentrated on the extreme events in climate variables and streamflow.

5.3 SCOPE OF FUTURE WORK

1. Studies on extreme events and their impacts on hydrological components may be studied.
2. Land use land cover and climate change impacts on other hydrological components like evapotranspiration, ground water etc., can be studied.
3. The comparison of climate variables and their impact variables based on different scenarios can be made.

REFERENCES

- Abijith, D., Saravanan, S., Singh, L., Jennifer, J. J., Saranya, T., and Parthasarathy, K. S. (2020). “GIS-based multi-criteria analysis for identification of potential groundwater recharge zones - a case study from Ponnaniyaru watershed, Tamil Nadu, India.” *HydroResearch*, 3, 1–14.
- Ahmed, K., Sachindra, D. A., Shahid, S., Iqbal, Z., Nawaz, N., and Khan, N. (2020). “Multi-model ensemble predictions of precipitation and temperature using machine learning algorithms.” *Atmos. Res.*, 236, 104806.
- Ahn, K. H., and Merwade, V. (2014). “Quantifying the relative impact of climate and human activities on streamflow.” *J. Hydrol.*, 515, 257–266.
- Ali, J., Khan, R., Ahmad, N., and Maqsood, I. (2012). “Random forests and decision trees.” *IJCSI Int. J. Comput. Sci. Issues*, 9(5), 272–278.
- Alshari, E. A., and Gawali, B. W. (2021). “Development of classification system for LULC using remote sensing and GIS.” *Glob. Transitions Proc.*, 2(1), 8–17.
- Amengual, A., Homar, V., Romero, R., Alonso, S., and Ramis, C. (2012). “A statistical adjustment of regional climate model outputs to local scales: application to Platja de Palma, Spain.” *J. Clim.*, 25(3), 939–957.
- Anwar, Z., Alam, A., Elahi, N., and Shah, I. (2022). “Assessing the trends and drivers of land use land cover change in district Abbottabad lower Himalayan region Pakistan.” *Geocarto Int.*, 1–16.
- Awad, M., and Khanna, R. (2015). “Efficient learning machines: theories, concepts, and applications for engineers and system designers.” M. Awad and R. Khanna, eds., Berkeley, CA: Apress, 67–80.
- Ayar, P. V., Vrac, M., Bastin, S., Carreau, J., Déqué, M., and Gallardo, C. (2016). “Intercomparison of statistical and dynamical downscaling models under the EURO- and MED-CORDEX initiative framework: present climate evaluations.” *Clim. Dyn.*, 46(3–4), 1301–1329.

- Ayugi, B., Tan, G., Ruoyun, N., Babaousmail, H., Ojara, M., Wido, H., Mumo, L., Ngoma, N. H., Nooni, I. K., and Ongoma, V. (2020). “Quantile mapping bias correction on Rossby centre regional climate models for precipitation analysis over Kenya, East Africa.” *Water*, 12(3), 1–23.
- Azadi, F., Ashofteh, P., and Loáiciga, H. A. (2019). “Reservoir water-quality projections under climate-change conditions.” *Water Resour. Manag.*, 33(1), 401–421.
- Babar, S., and Ramesh, H. (2014). “Analysis of extreme rainfall events over Nethravathi basin.” *ISH J. Hydraul. Eng.*, 20(2), 212–221.
- Babar, S., and Ramesh, H. (2015). “Streamflow response to land use – land cover change over the Nethravathi River basin, India.” *J. Hydrol. Eng.*, 20(10), 1–11.
- Banskota, A., Kayastha, N., Falkowski, M. J., Wulder, M. A., Froese, R. E., and White, J. C. (2014). “Forest monitoring using Landsat time series data: a review.” *Can. J. Remote Sens.*, 40(5), 362–384.
- Bao, Y., and Wen, X. (2017). “Projection of China’s near- and long-term climate in a new high-resolution daily downscaled dataset NEX-GDDP.” *J. Meteorol. Res.*, 31(1), 236–249.
- Basheer, A. K., Lu, H., Omer, A., Ali, A. B., and Abdelgader, A. M. S. (2016). “Impacts of climate change under CMIP5 RCP scenarios on the streamflow in the Dinder River and ecosystem habitats in Dinder National Park, Sudan.” *Hydrol. Earth Syst. Sci.*, 20(4), 1331–1353.
- Bastola, S., Murphy, C., and Sweeney, J. (2011). “The role of hydrological modelling uncertainties in climate change impact assessments of Irish river catchments.” *Adv. Water Resour.*, 34(5), 562–576.
- Benestad, R., Parding, K., Dobler, A., and Mezghani, A. (2017). “A strategy to effectively make use of large volumes of climate data for climate change adaptation.” *Clim. Serv.*, 6, 48–54.
- Berg, P., Feldmann, H., and Panitz, H. J. (2012). “Bias correction of high resolution regional climate model data.” *J. Hydrol.*, 448, 80–92.

- Bergstra, J., Komer, B., Eliasmith, C., Yamins, D., and Cox, D. D. (2015). “Hyperopt: a Python library for model selection and hyperparameter optimization.” *Comput. Sci. Discov.*, 8(1), 014008.
- Berihun, M. L., Tsunekawa, A., Haregeweyn, N., Meshesha, D. T., Adgo, E., Tsubo, M., Masunaga, T., Fenta, A. A., Sultan, D., and Yibeltal, M. (2019). “Exploring land use/land cover changes, drivers and their implications in contrasting agro-ecological environments of Ethiopia.” *Land use policy*, 87, 104052.
- Beven, K., and Smith, P. (2015). “Concepts of information content and likelihood in parameter calibration for hydrological simulation models.” *J. Hydrol. Eng.*, 20(20), A4014010.
- Beven, K., and Westerberg, I. (2011). “On red herrings and real herrings: disinformation and information in hydrological inference.” *Hydrol. Model. Water Cycle*, 25(10), 1676–1680.
- Bhatla, R., Verma, S., Pandey, R., and Tripathi, A. (2019). “Evolution of extreme rainfall events over Indo-Gangetic plain in changing climate during 1901–2010.” *J. Earth Syst. Sci.*, 128(5), 120.
- Bhatt, D., and Mall, R. K. (2015). “Surface water resources, climate change and simulation modeling.” *Aquat. Procedia*, 4, 730–738.
- Bhatti, H. A., Rientjes, T., Haile, A. T., Habib, E., and Verhoef, W. (2016). “Evaluation of bias correction method for satellite-based rainfall data.” *Sensors*, 16(6), 884.
- Bi, C., Bi, H., Sun, G., Chang, Y., and Gao, L. (2014). “Scale effects and variability of forest – water yield relationships on the Loess Plateau, China.” *For. Chron.*, 90(2), 184–191.
- Blöschl, G., and Montanari, A. (2010). “Climate change impacts – throwing the dice?” *Hydrol. Process.*, 24(3), 374–381.
- Boorman, D. B., and Sefton, C. E. M. (1997). “Recognising the uncertainty in the quantification of the effects of climate change on hydrological response.” *Clim. Chang.*, 35, 415–434.

- Bormann, H., Breuer, L., Gräff, T., Huisman, J. A., and Croke, B. (2009). “Assessing the impact of land use change on hydrology by ensemble modelling (LUCHEM) IV: model sensitivity to data aggregation and spatial (re-)distribution.” *Adv. Water Resour.*, 32(2), 171–192.
- Bouktif, S., Fiaz, A., Ouni, A., and Serhani, M. A. (2020). “Multi-sequence LSTM-RNN deep learning and metaheuristics for electric load forecasting.” *Energies*, 13(2), 1–21.
- Brans, J. P., and Vincke, P. (1985). “A preference ranking organization method: the PROMETHEE method for multiple criteria decision-making.” *Manage. Sci.*, 31(6), 647–656.
- Brans, J. P., Vincke, P., and Mareschal, B. (1986). “How to select and how to rank projects: the PROMETHEE method.” *Eur. J. Oper. Res.*, 24(2), 228–238.
- Breiman, L. (2001). “Random forests.” *Mach. Learn.*, 45(1), 5–32.
- Campbell, D. J., Lusch, D. P., Smucker, T. A., and Wangui, E. E. (2005). “Multiple methods in the study of driving forces of land use and land cover change: a case study of SE Kajiado District, Kenya.” *Hum. Ecol.*, 33(6), 763–794.
- Cannon, A. J., Sobie, S. R., and Murdock, T. Q. (2015). “Bias correction of GCM precipitation by quantile mapping: how well do methods preserve changes in quantiles and extremes?” *J. Clim.*, 28(17), 6938–6959.
- Cervantes, J., Garcia-Lamont, F., Rodríguez-Mazahua, L., and Lopez, A. (2020). “A comprehensive survey on support vector machine classification: applications, challenges and trends.” *Neurocomputing*, 408, 189–215.
- Chatterjee, P., and Chakraborty, S. (2016). “A comparative analysis of VIKOR method and its variants.” *Decis. Sci. Lett.*, 5(4), 469–486.
- Chaumont, D. (2014). *A guidebook on climate scenarios: using climate information to guide adaptation research and decisions*. 2016 Edition, Ouranos, 94.
- Chawla, I., and Mujumdar, P. P. (2015). “Isolating the impacts of land use and climate change on streamflow.” *Hydrol. Earth Syst. Sci.*, 19(8), 3633–3651.

Chen, J., Brissette, F. P., Lucas-Picher, P., and Caya, D. (2017). “Impacts of weighting climate models for hydro-meteorological climate change studies.” *J. Hydrol.*, 549, 534–546.

Chen, J., Brissette, F. P., Poulin, A., and Leconte, R. (2011). “Overall uncertainty study of the hydrological impacts of climate change for a Canadian watershed.” *Water Resour. Res.*, 47, W12509.

Chokkavarapu, N., and Mandla, V. R. (2017). “Impact assessment of watershed management on land use/land cover change using RS and GIS: a case study.” *Int. J. Civ. Eng. Technol.*, 8(4), 394–400.

Chollet, F. (2018). *Deep learning with Python*. Manning Publication, New York.

Clark, M. P., Wilby, R. L., Gutmann, E. D., Vano, J. A., Gangopadhyay, S., Wood, A. W., Fowler, H. J., Prudhomme, C., Arnold, J. R., and Brekke, L. D. (2016). “Characterizing uncertainty of the hydrologic impacts of climate change.” *Curr. Clim. Chang. reports*, 2, 55–64.

Çöltekin, A., Griffin, A. L., Slingsby, A., Robinson, A. C., Christophe, S., Rautenbach, V., Chen, M., Pettit, C., and Klippel, A. (2020). “Geospatial information visualization and extended reality displays.” *Manual Digital Earth*. Gou, H., Goodchild, M. F., Annoni, A., eds., Springer, Singapore.

Dams, J., Nossent, J., Senbeta, T. B., Willems, P., and Batelaan, O. (2015). “Multi-model approach to assess the impact of climate change on runoff.” *J. Hydrol.*, 529, 1601–1616.

Das, J., Treesa, A., and Umamahesh, N. V. (2018). “Modelling impacts of climate change on a river basin: analysis of uncertainty using REA & possibilistic approach.” *Water Resour. Manag.*, 32(15), 4833–4852.

Debats, S. R., Luo, D., Estes, L. D., Fuchs, T. J., and Caylor, K. K. (2016). “A generalized computer vision approach to mapping crop fields in heterogeneous agricultural landscapes.” *Remote Sens. Environ.*, 179, 210–221.

Déqué, M. (2007). “Frequency of precipitation and temperature extremes over France in an anthropogenic scenario: model results and statistical correction according to observed

values.” *Glob. Planet. Change*, 57(1–2), 16–26.

Déqué, M., Calmanti, S., Christensen, O. B., Dell Aquila, A., Maule, C. F., Haensler, A., Nikulin, G., and Teichmann, C. (2017). “A multi-model climate response over tropical Africa at +2 °C.” *Clim. Serv.*, 7, 87–95.

Dey, P., and Mishra, A. (2017). “Separating the impacts of climate change and human activities on streamflow: a review of methodologies and critical assumptions.” *J. Hydrol.*, 548, 278–290.

Dias, L. C. P., Macedo, M. N., Costa, M. H., Coe, M. T., and Neill, C. (2015). “Effects of land cover change on evapotranspiration and streamflow of small catchments in the upper Xingu River basin, Central Brazil.” *J. Hydrol. Reg. Stud.*, 4, 108–122.

Dixon, B., and Earls, J. (2012). “Effects of urbanization on streamflow using SWAT with real and simulated meteorological data.” *Appl. Geogr.*, 35(1–2), 174–190.

Dobler, A., and Ahrens, B. (2008). “Precipitation by a regional climate model and bias correction in Europe and South Asia.” *Meteorol. Zeitschrift*, 17(4), 499–509.

Dobler, C., Hagemann, S., Wilby, R. L., and Stotter, J. (2012). “Quantifying different sources of uncertainty in hydrological projections in an Alpine watershed.” *Hydrol. Earth Syst. Sci.*, 16(11), 4343–4360.

Dwarakish, G. S., and Ganasri, B. P. (2015). “Impact of land use change on hydrological systems: a review of current modeling approaches.” *Cogent Geosci.*, 1, 1115691.

Errasti, I., Ezcurra, A., Sáenz, J., and Ibarra-Berastegi, G. (2011). “Validation of IPCC AR4 models over the Iberian Peninsula.” *Theor. Appl. Climatol.*, 103(1), 61–79.

Evans, J. P., Ji, F., Lee, C., Smith, P., Argüeso, D., and Fita, L. (2013). “A regional climate modelling projection ensemble experiment – NARClIM.” *Geosci. Model Dev. Discuss.*, 6, 5117–5139.

Ezéchiél, O., Eric, A. A., Josué, Z. E., Eliézer, B. I., and Amédée, C. (2016). “Comparative study of seven bias correction methods applied to three regional climate models in Mekrou catchment (Benin , West Africa).” *Int. J. Curr. Eng. Technol.*, 6(5), 1831–1840.

- Fan, M., and Shibata, H. (2015). "Simulation of watershed hydrology and stream water quality under land use and climate change scenarios in Teshio River watershed, northern Japan." *Ecol. Indic. J.*, 50, 79–89.
- Fang, G. H., Yang, J., Chen, Y. N., and Zammit, C. (2015). "Comparing bias correction methods in downscaling meteorological variables for a hydrologic impact study in an arid area in China." *Hydrol. Earth Syst. Sci.*, 19(6), 2547–2559.
- Ficklin, D. L., Luo, Y., Luedeling, E., and Zhang, M. (2009). "Climate change sensitivity assessment of a highly agricultural watershed using SWAT." *J. Hydrol.*, 374(1–2), 16–29.
- Franklin, J. (1995). "Predictive vegetation mapping: geographic modelling of biospatial patterns in relation to environmental gradients." *Prog. Phys. Geogr. Earth Environ.*, 19(4), 474–499.
- Frazier, A. E., Vadjunec, J. M., Kedron, P., and Fagin, T. (2019). "Linking landscape ecology and land system architecture for land system science: an introduction to the special issue." *J. Land Use Sci.*, 14(2), 123–134.
- Friehat, T., Mulugeta, G., and Gala, T. S. (2015). "Modeling urban sprawls in northeastern Illinois." *J. Geosci. Geomatics*, 3(5), 133–141.
- Ganasri, B. P., Raju, A., and Dwarakish, G. S. (2013). "Different approaches for land use land cover change detection: a review." *J. Eng. Technol.*, 2(3), 44–48.
- Garg, V., Nikam, B. R., Thakur, P. K., Aggarwal, S. P., Gupta, P. K., and Srivastav, S. K. (2019). "Human-induced land use land cover change and its impact on hydrology." *HydroResearch*, 1, 48–56.
- Geurts, P., Ernst, D., and Wehenkel, L. (2006). "Extremely randomized trees." *Mach. Learn.*, 63(1), 3–42.
- Ghalehtimouri, K. J., Shamsoddini, A., Mousavi, M. N., Binti Che Ros, F., and Khedmatzadeh, A. (2022). "Predicting spatial and decadal of land use and land cover change using integrated cellular automata Markov chain model based scenarios (2019–2049) Zarriné-Rūd River basin in Iran." *Environ. Challenges*, 6, 100399.

Ghorbanian, A., Kakooei, M., Amani, M., Mahdavi, S., Mohammadzadeh, A., and Hasanlou, M. (2020). “Improved land cover map of Iran using Sentinel imagery within google earth engine and a novel automatic workflow for land cover classification using migrated training samples.” *ISPRS J. Photogramm. Remote Sens.*, 167, 276–288.

Glavan, M., Ceglar, A., and Pintar, M. (2015). “Assessing the impacts of climate change on water quantity and quality modelling in small Slovenian Mediterranean catchment - lesson for policy and decision makers.” *Hydrol. Process.*, 29(14), 3124–3144.

Gorelick, N., Hancher, M., Dixon, M., Ilyushchenko, S., Thau, D., and Moore, R. (2017). “Google earth engine: planetary-scale geospatial analysis for everyone.” *Remote Sens. Environ.*, 202, 18–27.

Gosain, A. K., Rao, S., and Basuray, D. (2006). “Climate change impact assessment on hydrology of Indian river basins.” *Curr. Sci.*, 90(3), 346–353.

Govind, N. R., and Ramesh, H. (2019). “The impact of spatiotemporal patterns of land use land cover and land surface temperature on an urban cool island: a case study of Bengaluru.” *Environ. Monit. Assess.*, 191(5).

Gutjahr, O., and Heinemann, G. (2013). “Comparing precipitation bias correction methods for high-resolution regional climate simulations using COSMO-CLM: effects on extreme values and climate change signal.” *Theor. Appl. Climatol.*, 114(3–4), 511–529.

Gyamfi, C., Ndambuki, J. M., and Salim, R. W. (2016a). “Simulation of sediment yield in a semi-arid river basin under changing land use: an integrated approach of hydrologic modelling and principal component analysis.” *Sustain.*, 8(11), 1–17.

Gyamfi, C., Ndambuki, J. M., and Salim, R. W. (2016b). “Hydrological responses to land use/cover changes in the Olifants basin, South Africa.” *Water*, 8(12), 1–16.

Halmy, M. W. A., Gessler, P. E., Hicke, J. A., and Salem, B. B. (2015). “Land use/land cover change detection and prediction in the north-western coastal desert of Egypt using Markov-CA.” *Appl. Geogr.*, 63, 101–112.

Hamad, R., Balzter, H., and Kolo, K. (2018). “Predicting land use/land cover changes using a CA-Markov model under two different scenarios.” *Sustainability*, 10(10), 1–23.

- Hassan, F., Safdar, T., Khan, A. U., Irtaza, G., Kazmi, S. M. H., and Murtaza, F. (2020). "Urbanization change analysis based on SVM and RF machine learning algorithms." *Int. J. Adv. Comput. Sci. Appl.*, 11(5), 591–601.
- Hattermann, F. F., Vetter, T., Breuer, L., Su, B., Daggupati, P., Donnelly, C., Fekete, B., Flörke, F., Gosling, S. N., Hoffmann, P., Liersch, S., Masaki, Y., Motovilov, Y., Müller, C., Samaniego, L., Stacke, T., Wada, Y., Yang, T., and Krysanova, V. (2018). "Sources of uncertainty in hydrological climate impact assessment: a cross-scale study." *Environ. Res. Lett.*, 13(1), 015006.
- Hawkins, E., and Sutton, R. (2009). "The potential to narrow uncertainty in regional climate predictions." *Bull. Am. Meteorol. Soc.*, 90(8), 1095–1107.
- Hay, L. E., Clark, M. P., Wilby, R. L., Gutowski Jr, W. J., Leavesley, G. H., Pan, Z., Arritt, R. W., and Takle, E. S. (2002). "Use of regional climate model output for hydrologic simulations." *J. Hydrometeorol.*, 3(5), 571-590.
- Holman, I. P., Brown, C., Carter, T. R., Harrison, P. A., and Rounsevell, M. (2019). "Improving the representation of adaptation in climate change impact models." *Reg. Environ. Chang.*, 19(3), 711–721.
- Hotelling, H. (1933). "Analysis of a complex of statistical variables into principal components." *J. Educ. Psychol.*, 24, 417–441.
- Hundecha, Y., and Bárdossy, A. (2004). "Modeling of the effect of land use changes on the runoff generation of a river basin through parameter regionalization of a watershed model." *J. Hydrol.*, 292, 281–295.
- Hurskainen, P., Adhikari, H., Siljander, M., Pellikka, P. K. E., and Hemp, A. (2019). "Auxiliary datasets improve accuracy of object-based land use/land cover classification in heterogeneous savanna landscapes." *Remote Sens. Environ.*, 233, 111354.
- Hwang, C. L., and Yoon, K. (1981). "Multiple attribute decision making: methods and applications." *Lect. Notes Econ. Math. Syst.*, 186(1).
- Hyandye, C. (2015). "GIS and logit regression model applications in land use/land cover change and distribution in Usangu catchment." *Am. J. Remote Sens.*, 3(1), 6.

Ines, A. V. M., and Hansen, J. W. (2006). “Bias correction of daily GCM rainfall for crop simulation studies.” *Agric. For. Meteorol.*, 138(1–4), 44–53.

IPCC. (2012). *Managing the risks of extreme events and disasters to advance climate change adaptation. Spec. Rep. Intergov. Panel Clim. Chang.*, New York, USA: Cambridge University Press.

Isik, S., Kalin, L., Schoonover, J. E., Srivastava, P., and Lockaby, B. G. (2013). “Modeling effects of changing land use/cover on daily streamflow: an artificial neural network and curve number based hybrid approach.” *J. Hydrol.*, 485, 103–112.

Izurieta, J. E. A., Márquez, C. O., García, V. J., Recalde-Moreno, C. G., Rodríguez-Llerena, M. V., and Damián-Carrión, D. A. (2017). “Land cover classification in an ecuadorian mountain geosystem using a random forest classifier, spectral vegetation indices, and ancillary geographic data.” *Geosci.*, 7(2), 34.

Jain, S., Salunke, P., Mishra, S. K., Sahany, S., and Choudhary, N. (2019). “Advantage of NEX-GDDP over CMIP5 and CORDEX data: Indian summer monsoon.” *Atmos. Res.*, 228, 152–160.

Jiang, T., Chen, Y. D., Xu, C., Chen, X., Chen, X., and Singh, V. P. (2007). “Comparison of hydrological impacts of climate change simulated by six hydrological models in the.” *J. Hydrol.*, 336, 316–333.

Jolliffe, I. T., and Cadima, J. (2016). “Principal component analysis: a review and recent developments.” *Philos. Trans. R. Soc. A*, 374(2065).

Jubb, I., Canadell, P., and Dix, M. (2013). “Representative concentration pathways (RCPs).” *Aust. Clim. Chang. Sci. Progr.*, 5–7.

Jung, I., Moradkhani, H., and Chang, H. (2012). “Uncertainty assessment of climate change impacts for hydrologically distinct river basins.” *J. Hydrol.*, 467, 73–87.

Kale, M. P., Chavan, M., Pardeshi, S., Joshi, C., Verma, P. A., Roy, P. S., Srivastav, S. K., Srivastava, V. K., Jha, A. K., Chaudhari, S., Giri, Y., and Krishna Murthy, Y. V. N. (2016). “Land-use and land-cover change in Western Ghats of India.” *Environ. Monit. Assess.*, 188(7), 387.

- Kamwi, J. M., Cho, M. A., Kaetsch, C., Manda, S. O., Graz, F. P., and Chirwa, P. W. (2018). "Assessing the spatial drivers of land use and land cover change in the protected and communal areas of the Zambezi region, Namibia." *Land*, 7(4), 131.
- Karlsson, I. B., Sonnenborg, T. O., Refsgaard, J. C., Trolle, D., Børgesen, C. D., Olesen, J. E., Jeppesen, E., and Jensen, K. H. (2016). "Combined effects of climate models, hydrological model structures and land use scenarios on hydrological impacts of climate change." *J. Hydrol.*, 535, 301–317.
- Katz, R. W. (2002). "Techniques for estimating uncertainty in climate change scenarios and impact studies." *Clim. Res.*, 20, 167–185.
- Katz, R. W., Craigmile, P. F., Guttorp, P., Haran, M., Sansó, B., and Stein, M. L. (2013). "Uncertainty analysis in climate change assessments." *Nat. Clim. Chang.*, 3(9), 769–771.
- Kauffeldt, A., Halldin, S., Rodhe, A., Xu, C. Y., and Westerberg, I. K. (2013). "Disinformative data in large-scale hydrological modelling." *Hydrol. Earth Syst. Sci.*, 17(7), 2845–2857.
- Khan, N., Shahid, S., Ahmed, K., Ismail, T., Nawaz, N., and Son, M. (2018). "Performance assessment of general circulation model in simulating daily precipitation and temperature using multiple gridded datasets." *Water*, 10(12), 1793.
- Kim, J., Choi, J., Choi, C., and Park, S. (2013). "Impacts of changes in climate and land use/land cover under IPCC RCP scenarios on stream flow in the Hoeya River basin, Korea." *Sci. Total Environ.*, 452, 181–195.
- Kim, K. B., Kwon, H., and Han, D. (2015). "Bias correction methods for regional climate model simulations considering the distributional parametric uncertainty underlying the observations." *J. Hydrol.*, 530, 568–579.
- Kobayashi, N., Tani, H., Wang, X., and Sonobe, R. (2020). "Crop classification using spectral indices derived from Sentinel-2A imagery." *J. Inf. Telecommun.*, 4(1), 67–90.
- Koko, A. F., Yue, W., Abubakar, G. A., Hamed, R., and Alabsi, A. A. N. (2020). "Monitoring and predicting spatio-temporal land use/land cover changes in Zaria City, Nigeria, through an integrated cellular automata and Markov chain model (CA-Markov)."

Sustainability, 12(24), 1–21.

Kondraju, T. T., Mandla, V. R. B., Mahendra, R. S., and Kumar, T. S. (2014). “Evaluation of various image classification techniques on Landsat to identify coral reefs.” *Geomatics, Nat. Hazards Risk*, 5(2), 173–184.

Kour, R., Patel, N., and Krishna, A. P. (2016). “Climate and hydrological models to assess the impact of climate change on hydrological regime: a review.” *Arab. J. Geosci.*, 9(9), 544.

Krysanova, V., and Hattermann, F. F. (2017). “Intercomparison of climate change impacts in 12 large river basins: overview of methods and summary of results.” *Clim. Change*, 141(3), 363–379.

Krysanova, V., Hattermann, F., Huang, S., Hesse, C., Vetter, T., Liersch, S., Koch, H., and Kundzewicz, Z. W. (2015). “Modelling climate and land-use change impacts with SWIM: lessons learnt from multiple applications.” *Hydrol. Sci. J.*, 60(4), 606–635.

Krysanova, V., and Srinivasan, R. (2015). “Assessment of climate and land use change impacts with SWAT.” *Reg. Environ. Chang.*, 15(3), 431–434.

Kumar, K. S., Kumari, K. P., and Bhaskar, P. U. (2016). “Application of Markov chain & cellular automata based model for prediction of urban transitions.” *Int. Conf. Electr. Electron. Optim. Tech. ICEEOT 2016*, 4007–4012.

Kumar Raju, B. C., and Nandagiri, L. (2017). “Analysis of historical trends in hydrometeorological variables in the upper Cauvery basin, Karnataka, India.” *Curr. Sci.*, 112(3), 577–587.

Kumar, S., Chanda, K., and Pasupuleti, S. (2020). “Spatiotemporal analysis of extreme indices derived from daily precipitation and temperature for climate change detection over India.” *Theor. Appl. Climatol.* 140, 343–357.

Kumar, V., and Jain, S. K. (2011). “Trends in rainfall amount and number of rainy days in river basins of India (1951-2004).” *Hydrology Research*, 42(4), 290–306.

Kundu, S., Khare, D., and Mondal, A. (2017). “An integrated modelling system to predict

hydrological processes under climate and land-use/cover change scenarios.” *Ecol. Eng.*, 105(10), 1–23.

Kundu, S., Mondal, A., Khare, D., Hain, C., and Lakshmi, V. (2018). “Projecting climate and land use change impacts on actual evapotranspiration for the Narmada River basin in central India in the future.” *Remote Sens.*, 10(4), 578.

Kundzewicz, Z. W., Krysanova, V., Benestad, R. E., Hov, Ø., Piniewski, M., and Otto, I. M. (2018). “Uncertainty in climate change impacts on water resources.” *Environ. Sci. Policy*, 79, 1–8.

Kusangaya, S., Warburton, M. L., Garderen, E. A. van, and Jewitt, G. P. W. (2014). “Impacts of climate change on water resources in southern Africa: a review.” *Phys. Chem. Earth, Parts A/B/C*, 67, 47–54.

Laflamme, E. M., Linder, E., and Pan, Y. (2016). “Statistical downscaling of regional climate model output to achieve projections of precipitation extremes.” *Weather Clim. Extrem. J.*, 12, 15–23.

LaFond, K. M., Griffis, V. W., and Spellman, P. (2014). “Forcing hydrologic models with GCM output: bias correction vs. the ‘delta change’ method.” *World Environ. Water Resour. Congr. 2014 Water Without Borders - Proc. 2014 World Environ. Water Resour. Congr.*, 1, 2146–2155.

Legesse, D., Vallet-Coulomb, C., and Gasse, F. (2003). “Hydrological response of a catchment to climate and land use changes in tropical Africa: case study south central Ethiopia.” *J. Hydrol.*, 275, 67–85.

Lenderink, G., Buishand, A., and Deursen, W. Van. (2007). “Estimates of future discharges of the river Rhine using two scenario methodologies: direct versus delta approach.” *Hydrol. Earth Syst. Sci.*, 11(3), 1145–1159.

Li, H., Sheffield, J., and Wood, E. F. (2010). “Bias correction of monthly precipitation and temperature fields from intergovernmental panel on climate change AR4 models using equidistant quantile matching.” *J. Geophys. Res. Atmos.*, 115(D10).

Li, X., Wang, K., Liuz, L., Xin, J., Yang, H., and Gao, C. (2011). “Application of the

entropy weight and TOPSIS method in safety evaluation of coal mines.” *Procedia Eng.*, 26, 2085–2091.

Li, Z., Liu, W.-Z., Zhang, X.-C., and Zheng, F.-L. (2009). “Impacts of land use change and climate variability on hydrology in an agricultural catchment on the Loess Plateau of China.” *J. Hydrol.*, 377(1–2), 35–42.

Lin, Y., Verburg, P. H., Chang, C., Chen, H., and Chen, M. (2009). “Landscape and urban planning developing and comparing optimal and empirical land-use models for the development of an urbanized watershed forest in Taiwan.” *Landsc. Urban Plan. J.*, 92, 242–254.

Lutz, A. F., Maat, H. W. ter, Biemans, H., Shrestha, A. B., Westerd, P., and Immerzeel, W. W. (2016). “Selecting representative climate models for climate change impact studies: an advanced envelope-based selection approach.” *Int. J. Climatol.*, 36(12), 3988–4005.

Ma, H., Yang, D., Tan, S. K., Gao, B., and Hu, Q. (2010). “Impact of climate variability and human activity on streamflow decrease in the Miyun Reservoir catchment.” *J. Hydrol.*, 389(3–4), 317–324.

Mahmood, R., and Babel, M. S. (2013). “Evaluation of SDSM developed by annual and monthly sub-models for downscaling temperature and precipitation in the Jhelum basin, Pakistan and India.” *Theor. Appl. Climatol.*, 113(1–2), 27–44.

Mamuye, M., and Kebebewu, Z. (2018). “Review on impacts of climate change on watershed hydrology.” *J. Environ. Earth Sci.*, 8(1), 91–99.

Mango, L. M., Melesse, A. M., McClain, M. E., Gann, D., and Setegn, S. G. (2011). “Land use and climate change impacts on the hydrology of the upper Mara River basin, Kenya: results of a modeling study to support better resource management.” *Hydrol. Earth Syst. Sci.*, 15(7), 2245–2258.

Maraun, D. (2016). “Bias correcting climate change simulations - a critical review.” *Curr. Clim. Chang. Reports*, 2(4), 211–220.

Maraun, D., Wetterhall, F., Ireson, A. M., Chandler, R. E., Kendon, E. J., Widmann, M., Brienen, S., Rust, H. W., Sauter, T., Themeßl, M., Venema, V. K. C., Chun, K. P., Goodess,

- C. M., Jones, R. G., Onof, C., Vrac, M., and Thiele-Eich, I. (2010). "Precipitation downscaling under climate change: recent developments to bridge the gap between dynamical models and the end user." *Rev. Geophys.*, 48(3), 1–34.
- Maurer, E. P., and Hidalgo, H. G. (2008). "Utility of daily vs monthly large-scale climate data: an intercomparison of two statistical downscaling methods." *Hydrol. Earth Syst. Sci.*, 12, 551–563.
- Maurer, E. P., and Pierce, D. W. (2014). "Bias correction can modify climate model simulated precipitation changes without adverse effect on the ensemble mean." *Hydrol. Earth Syst. Sci.*, 18(3), 915–925.
- Maximo, C., McAvaney, B., Pitman, A., and Perkins, S. (2008). "Ranking the AR4 climate models over the Murray-Darling basin using simulated maximum temperature, minimum temperature and precipitation." *Int. J. Climatol.*, 28, 1097–1112.
- Maxwell, A. E., Strager, M. P., Warner, T. A., Ramezan, C. A., Morgan, A. N., and Pauley, C. E. (2019). "Large-area, high spatial resolution land cover mapping using random forests, GEOBIA, and NAIP orthophotography: findings and recommendations." *Remote Sens.*, 11, 1409.
- Mendez, M., Maathuis, B., Hein-Griggs, D., and Alvarado-Gamboa, L. F. (2020). "Performance evaluation of bias correction methods for climate change monthly precipitation projections over Costa Rica." *Water*, 12(2), 482.
- Meter, V. K., Thompson, S. E., and Basu, N. B. (2016). "Human impacts on stream hydrology and water quality." *Stream Ecosyst. a Chang. Environ.*, 11, 441–490.
- Mileham, L., Taylor, R. G., Todd, M., Tindimugaya, C., and Thompson, J. (2009). "The impact of climate change on groundwater recharge and runoff in a humid, equatorial catchment: sensitivity of projections to rainfall intensity." *Hydrol. Sci. J.*, 54(4), 727–738.
- Milly, P. C. D., Betancourt, J., Falkenmark, M., Hirsch, R. M., Kundzewicz, Z. W., Lettenmaier, D. P., and Stouffer, R. J. (2008). "Climate change: stationarity is dead: whither water management?" *Science*, 319, 573–574.
- Minville, M., Brissette, F., and Leconte, R. (2008). "Uncertainty of the impact of climate

change on the hydrology of a nordic watershed.” *J. Hydrol.*, 358(1–2), 70–83.

Mishra, V., Bhatia, U., and Tiwari, A. D. (2020). “Bias-corrected climate projections for South Asia from coupled model intercomparison project-6.” *Sci. Data*, 7(1), 1–13.

Mizuta, R., Yoshimura, H., Murakami, H., Matsueda, M., Endo, H., Ose, T., Kamiguchi, K., Hosaka, M., Sugi, M., Yukimoto, S., Kusunoki, S., and Kitoh, A. (2012). “Climate simulations using MRI-AGCM3.2 with 20-km grid.” *J. Meteorol. Soc. Japan*, 90, 233–258.

Moradkhani, H., and Sorooshian, S. (2009). “General review of rainfall-runoff modeling: model calibration, data assimilation, and uncertainty analysis.” *Hydrol. Model. Water Cycle*, Berlin, Heidelberg: Springer Berlin Heidelberg, 1–24.

Morais, D. C., and Almeida, A. T. de. (2012). “Group decision making on water resources based on analysis of individual rankings.” *Omega*, 40(1), 42–52.

Mudbhatkal, A., and Mahesha, A. (2017). “Regional climate trends and topographic influence over the Western Ghat catchments of India.” *Int. J. Climatol.*, 38(5), 2265–2279.

Mudbhatkal, A., and Mahesha, A. (2018). “Bias correction methods for hydrologic impact studies over India’s Western Ghat basins.” *J. Hydrol. Eng.*, 23(2), 1–13.

Mudelsee, M. (2019). “Trend analysis of climate time series: a review of methods.” *Earth-Science Rev.*, 190, 310–322.

Mujumdar, P. P. (2013). “Climate change : a growing challenge for water management in developing countries.” *Water Resour. Manag.*, 27(4), 953–954.

Myers, N., Mittermeier, R. A., Mittermeier, C. G., Fonseca, G. A. B., and Kent, J. (2000). “Biodiversity hotspots for conservation priorities.” *Nature*, 403, 853–858.

Naboureh, A., Li, A., Bian, J., Lei, G. G., and Amani, M. (2020). “A hybrid data balancing method for classification of imbalanced training data within google earth engine: case studies from mountainous regions.” *Remote Sens.*, 12(20), 3301.

- Narsimlu, B., Gosain, A. K., and Chahar, B. R. (2013). "Assessment of future climate change impacts on water resources of upper Sind River basin, India using SWAT model." *Water Resour. Manag.*, 27(10), 3647–3662.
- Näschen, K., Diekkrüger, B., Evers, M., Höllermann, B., Steinbach, S., and Thonfeld, F. (2019). "The impact of land use/land cover change (LULCC) on water resources in a tropical catchment in Tanzania under different climate change scenarios." *Sustain.*, 11(24), 1–28.
- Nash, J. E., and Sutcliffe, J. V. (1970). "River flow forecasting through conceptual models part I—a discussion of principles." *J. Hydrol.*, 10(3), 282–290.
- Nath, B., Wang, Z., Ge, Y., Islam, K., Singh, R. P., and Niu, Z. (2020). "Land use and land cover change modeling and future potential landscape risk assessment using Markov-CA model and analytical hierarchy process." *ISPRS Int. J. Geo-Information*, 9(2), 134.
- Nilawar, A. P., and Waikar, M. L. (2019). "Impacts of climate change on streamflow and sediment concentration under RCP 4.5 and 8.5: a case study in Purna River basin, India." *Sci. Total Environ.*, 650, 2685–2696.
- Nóbrega, M. T., Collischonn, W., Tucci, C. E. M., and Paz, A. R. (2011). "Uncertainty in climate change impacts on water resources in the Rio Grande basin, Brazil." *Hydrol. Earth Syst. Sci.*, 15(2), 585–595.
- Noori, N., and Kalin, L. (2016). "Coupling SWAT and ANN models for enhanced daily streamflow prediction." *J. Hydrol.*, 533, 141–151.
- Notebaert, B., Verstraeten, G., Ward, P., Renssen, H., and Rompaey, A. Van. (2011). "Modeling the sensitivity of sediment and water runoff dynamics to holocene climate and land use changes at the catchment scale." *Geomorphology*, 126(1–2), 18–31.
- Ntegeka, V., Baguis, P., Roulin, E., and Willems, P. (2014). "Developing tailored climate change scenarios for hydrological impact assessments." *J. Hydrol.*, 508, 307–321.
- Nguyen, C. T., Chidthaisong, A., Kieu Diem, P., and Huo, L.-Z. (2021). "A Modified Bare Soil Index to Identify Bare Land Features during Agricultural Fallow-Period in Southeast Asia Using Landsat 8." *Land*, 10(3), 231,1-17.

O'Neill, B. C., Kriegler, E., Ebi, K. L., Kemp-Benedict, E., Riahi, K., Rothman, D. S., Ruijven, B. J. van, Vuuren, D. P. van, Birkmann, J., Kok, K., Levy, M., and Solecki, W. (2017). "The roads ahead: narratives for shared socioeconomic pathways describing world futures in the 21st century." *Glob. Environ. Chang.*, 42, 169–180.

O'Neill, B. C., Kriegler, E., Riahi, K., Ebi, K. L., Hallegatte, S., Carter, T. R., Mathur, R., and Vuuren, D. P. van. (2014). "A new scenario framework for climate change research: the concept of shared socioeconomic pathways." *Clim. Change*, 122(3), 387–400.

Olsson, T., Jakkila, J., Veijalainen, N., Backman, L., Kaurola, J., and Vehviläinen, B. (2015). "Impacts of climate change on temperature, precipitation and hydrology in Finland - studies using bias corrected regional climate model data." *Hydrol. Earth Syst. Sci.*, 19(7), 3217–3238.

Opricovic, S. (1998). "Multicriteria Optimization of Civil Engineering Systems." *PhD Thesis, Fac. Civ. Eng. Belgrade*, 302.

Opricovic, S., and Tzeng, G. H. (2004). "Compromise solution by MCDM methods: a comparative analysis of VIKOR and TOPSIS." *Eur. J. Oper. Res.*, 156(2), 445–455.

Oyebode, O., Adeyemo, J., and Otieno, F. (2014). "Uncertainty sources in climate change impact modelling of water resource systems." *Acad. J. Sci.*, 3(2), 245–260.

Pai, D. S., Sridhar, L., Rajeevan, M., Sreejith, O. P., Satbhai, N. S., and Mukhopadhyay, B. (2014). "Development of a new high spatial resolution ($0.25^\circ \times 0.25^\circ$) long period (1901-2010) daily gridded rainfall data set over India and its comparison with existing data sets over the region." *Mausam*, 65(1), 1–18.

Pang, B., Yue, J., Zhao, G., and Xu, Z. (2017). "Statistical downscaling of temperature with the random forest model." *Adv. Meteorol.*, 2017.

Parthasarathy, K. S. S., and Deka, P. C. (2021). "Spatio-temporal classification and prediction of land use and land cover change for the Vembanad Lake system, Kerala: a machine learning approach." *Environ. Sci. Pollut. Res.*

- Parthasarathy, K. S. S., Saravanan, S., Deka, P. C., and Devanatham, A. (2022). “Assessment of potentially vulnerable zones using geospatial approach along the coast of Cuddalore district, East coast of India.” *ISH J. Hydraul. Eng.*, 28(sup1), 422–432.
- Pechlivanidis, I. G., and Arheimer, B. (2015). “Large-scale hydrological modelling by using modified PUB recommendations: the India-HYPE case.” *Hydrol. Earth Syst. Sci.*, 19(11), 4559–4579.
- Pedregosa, F., Varoquaux, G., Gramfort, A., Michel, V., Thirion, B., Grisel, O., Blondel, M., Prettenhofer, P., Weiss, R., Dubourg, V., Vanderplas, J., Passos, A., Cournapeau, D., Brucher, M., Perrot, M., and Duchesna, É. (2011). “Scikit-learn: machine learning in Python.” *J. Mach. Learn. Res.*, 12(85), 2825–2830.
- Perkins, S. E., Pitman, A. J., Holbrook, N. J., and McAneney, J. (2007). “Evaluation of the AR4 Climate Models’ Simulated Daily Maximum Temperature, Minimum Temperature, and Precipitation over Australia Using Probability.” *J. Clim.*, 20(17), 4356–4376.
- Pervez, S., and Henebry, G. M. (2015). “Assessing the impacts of climate and land use and land cover change on the freshwater availability in the Brahmaputra River basin.” *J. Hydrol. Reg. Stud.*, 3, 285–311.
- Petchprayoon, P., Blanken, P. D., Ekkawatpanit, C., and Hussein, K. (2010). “Hydrological impacts of land use/land cover change in a large river basin in central-northern Thailand.” *Int. J. Climatol.*, 30(13), 1917–1930.
- Phiri, D., and Morgenroth, J. (2017). “Developments in Landsat land cover classification methods: a review.” *Remote Sens.*, 9(9), 967.
- Piani, C., Weedon, G. P., Best, M., Gomes, S. M., Viterbo, P., Hagemann, S., and Haerter, J. O. (2010). “Statistical bias correction of global simulated daily precipitation and temperature for the application of hydrological models.” *J. Hydrol.*, 395(3–4), 199–215.
- Piao, S., Ciais, P., Huang, Y., Shen, Z., Peng, S., Li, J., Zhou, L., Liu, H., Ma, Y., Ding, Y., Friedlingstein, P., Liu, C., Tan, K., Yu, Y., Zhang, T., and Fang, J. (2010). “The impacts of climate change on water resources and agriculture in China.” *Nature*, 467(7311), 43–51.

Pielke, R. A., Pitman, A., Niyogi, D., Mahmood, R., McAlpine, C., Hossain, F., Goldewijk, K. K., Nair, U., Betts, R., Fall, S., Reichstein, M., Kabat, P., and Noblet, N. de. (2011). “Land use/land cover changes and climate: modeling analysis and observational evidence.” *WIREs Clim Chang.*, 2, 828–850.

Pomerol, J. C., and Romero, S. B. (2012). *Multicriterion decision in management: principles and practice*, Springer New York, 25.

Praskievicz, S., and Chang, H. (2009). “A review of hydrological modelling of basin-scale climate change and urban development impacts.” *Prog. Phys. Geogr.*, 33(5), 650–671.

Praskievicz, S., and Chang, H. (2011). “Impacts of climate change and urban development on water resources in the Tualatin River basin, Oregon.” *Ann. Assoc. Am. Geogr.*, 101(2), 249–271.

Qu, L., Chen, Z., Li, M., Zhi, J., and Wang, H. (2021). “Accuracy improvements to pixel-based and object-based LULC classification with auxiliary datasets from google earth engine.” *Remote Sens.*, 13(3), 453.

Raghavendra, S., and Deka, P. C. (2014). “Support vector machine applications in the field of hydrology: A review.” *Appl. Soft Comput. J.*, 19, 372–386.

Rajbongshi, P., Das, T., and Adhikari, D. (2018). “Microenvironmental heterogeneity caused by anthropogenic LULC foster lower plant assemblages in the riparian habitats of lentic systems in tropical floodplains.” *Sci. Total Environ.*, 639, 1254–1260.

Raju, K. S., and Kumar, D. N. (2014a). “Ranking of global climate models for India using multicriterion analysis.” *Clim. Res.*, 60(2), 103–117.

Raju, K. S., and Kumar, D. N. (2014b). *Multicriterion analysis in engineering and management*. Prentice Hall India, New Delhi.

Raju, K. S., and Kumar, D. N. (2015). “Ranking general circulation models for India using TOPSIS.” *J. Water Clim. Chang.*, 6(2), 288–299.

Raju, K. S., and Kumar, D. N. (2018). *Impact of Climate Change on Water Resources*. Springer, Singapore

- Raju, K. S., Sonali, P., and Kumar, D. N. (2017). "Ranking of CMIP5-based global climate models for India using compromise programming." *Theor. Appl. Climatol.*, 128, 563–574.
- Rawat, J. S. e, and Kumar, M. (2015). "Monitoring land use/cover change using remote sensing and GIS techniques: a case study of Hawalbagh block, district Almora, Uttarakhand, India." *Egypt. J. Remote Sens. Sp. Sci.*, 18(1), 77–84.
- Reichler, T., and Kim, J. (2008). "How well do coupled models simulate today's climate?" *Bull. Am. Meteorol. Soc.*, 89(3), 303–311.
- Ren, Y., Lü, Y., Comber, A., Fu, B., Harris, P., and Wu, L. (2019). "Spatially explicit simulation of land use/land cover changes: current coverage and future prospects." *Earth-Science Rev.*, 190, 398–415.
- Riahi, K., Vuuren, D. P. van, Kriegler, E., Edmonds, J., O'Neill, B. C., Fujimori, S., Bauer, N., Calvin, K., Dellink, R., Fricko, O., Lutz, W., Popp, A., and Tavoni, M. (2017). "The Shared Socioeconomic Pathways and their energy, land use, and greenhouse gas emissions implications: An overview." *Global Environmental Change*, 42, 153–168.
- Richards, J. A., Landgrebe, D. A., and Swain, P. H. (1982). "A means for utilizing ancillary information in multispectral classification." *Remote Sens. Environ.*, 12(6), 463–477.
- Rikimaru, A., Roy, P. S., and Miyatake, S. (2002). "Tropical forest cover density mapping." *Trop. Ecol.*, 43(1), 39–47.
- Rodríguez-Blanco, M., Arias, R., Taboada-Castro, M., Nunes, J., Keizer, J., and Taboada-Castro, M. (2016). "Potential impact of climate change on suspended sediment yield in NW Spain: a case study on the Corbeira catchment." *Water*, 8(10), 444.
- Rouse, J. W., Haas, R. H., Schell, J. A., and Deering, D. W. (1974). "Monitoring Vegetation Systems in the Great Plains with ERTS." *NASA Spec. Publ.*, 309.
- Rwigi, S. K., Muthama, J. N., and Opere, A. O. (2016). "Simulated impacts of climate change on surface water yields over the Sondu basin in Kenya." *Int. J. Innov. Educ. Res.*, 4(8), 160–172.

Sachindra, D. A., Ahmed, K., Rashid, M. M., Shahid, S., and Perera, B. J. C. (2018). “Statistical downscaling of precipitation using machine learning techniques.” *Atmos. Res.*, 212, 240–258.

Sagheer, A., and Kotb, M. (2019). “Unsupervised pre-training of a deep LSTM-based stacked autoencoder for multivariate time series forecasting problems.” *Sci. Rep.*, 9(1), 19038.

Sahoo, S., Dey, S., Dhar, A., Debsarkar, A., and Pradhan, B. (2019). “On projected hydrological scenarios under the influence of bias-corrected climatic variables and LULC.” *Ecol. Indic.*, 106, 105440.

Shahi, E., Karimi, S., and Jafari, H. R. (2020). “Monitoring and modeling land use/cover changes in Arasbaran protected area using and integrated Markov chain and artificial neural network.” *Model. Earth Syst. Environ.*, 6(3), 1901–1911.

Shelestov, A., Lavreniuk, M., Kussul, N., Novikov, A., and Skakun, S. (2017). “Exploring google earth engine platform for big data processing: classification of multi-temporal satellite imagery for crop mapping.” *Front. Earth Sci.*, 5(17), 1–10.

Sheykhmousa, M., Mahdianpari, M., Ghanbari, H., Mohammadimanesh, F., Ghamisi, P., and Homayouni, S. (2020). “Support vector machine versus random forest for remote sensing image classification: a meta-analysis and systematic review.” *IEEE J. Sel. Top. Appl. Earth Obs. Remote Sens.*, 13, 6308–6325.

Shrestha, M., Acharyaa, S. C., and Shrestha, P. K. (2017). “Bias correction of climate models for hydrological modelling – are simple methods still useful?” *Meteorol. Appl.*, 24(3), 531–539.

Simpson, G. C. (1921). “The origin of the south-west monsoon.” *Nature*, 107(2683), 154.

Singh, V., Jain, S. K., and Singh, P. K. (2019). “Inter-comparisons and applicability of CMIP5 GCMs, RCMs and statistically downscaled NEX-GDDP based precipitation in India.” *Sci. Total Environ.*, 697, 134163.

Singh, V., and Xiaosheng, Q. (2019). “Data assimilation for constructing long-term gridded daily rainfall time series over Southeast Asia.” *Clim. Dyn.*, 53(5–6), 3289–3313.

- Sinha, R. K., and Eldho, T. I. (2018). “Effects of historical and projected land use/cover change on runoff and sediment yield in the Netravati River basin, Western Ghats, India.” *Environ. Earth Sci.*, 77(3), 111.
- Sinha, R. K., Eldho, T. I., and Subimal, G. (2020). “Assessing the impacts of land use/land cover and climate change on surface runoff of a humid tropical river basin in Western Ghats, India.” *Int. J. River Basin Manag.*, 1–12.
- Smitha, P. S., Narasimhan, B., Sudheer, K. P., and Annamalai, H. (2018). “An improved bias correction method of daily rainfall data using a sliding window technique for climate change impact assessment.” *J. Hydrol.*, 556, 100–118.
- Soro, G., Yao, A., Kouame, Y., and Bi, T. (2017). “Climate change and its impacts on water resources in the Bandama basin, Côte D’ivoire.” *Hydrology*, 4(1), 18.
- Sreelatha, K., and Anand Raj, P. (2019). “Ranking of CMIP5-based global climate models using standard performance metrics for Telangana region in the southern part of India.” *ISH J. Hydraul. Eng.*, 27(sup1), 556-565.
- Srivastava, A. K., Rajeevan, M., and Kshirsagar, S. R. (2009). “Development of a high resolution daily gridded temperature data set (1969 – 2005) for the Indian region.” *Atmos. Sci. Lett.*, 10, 249–254.
- Su, B., Huang, J., Zeng, X., Gao, C., and Jiang, T. (2017). “Impacts of climate change on streamflow in the upper Yangtze River basin.” *Clim. Change*, 141(3), 533–546.
- Switanek, B. M., Troch, A. P., Castro, L. C., Leuprecht, A., Chang, H. I., Mukherjee, R., and Demaria, M. C. E. (2017). “Scaled distribution mapping: A bias correction method that preserves raw climate model projected changes.” *Hydrol. Earth Syst. Sci.*, 21(6), 2649–2666.
- Talchabhadel, R., and Karki, R. (2019). “Assessing climate boundary shifting under climate change scenarios across Nepal.” *Environmental Monit. Assess.*, 191(8), 520.
- Tang, J., Niu, X., Wang, S., Gao, H., Wang, X., and Wu, J. (2016). “Statistical downscaling and dynamical downscaling of regional climate in China: present climate evaluations and future climate projections.” *J. Geophys. Res. Atmos. Res.*, 121, 2110–2129.

- Taylor, K. E. (2001). “Summarizing multiple aspects of model performance in a single diagram.” *J. Geophys. Res.*, 106(D7), 7183–7192.
- Tegegne, G., Park, D. K., and Kim, Y. O. (2017). “Comparison of hydrological models for the assessment of water resources in a data-scarce region, the upper Blue Nile River basin.” *J. Hydrol. Reg. Stud.*, 14, 49–66.
- Teutschbein, C., and Seibert, J. (2012). “Bias correction of regional climate model simulations for hydrological climate-change impact studies: review and evaluation of different methods.” *J. Hydrol.*, 456, 12–29.
- Thamilselvan, P. (2015). “A comparative study of SVM, RF and CART algorithms for image classification.” *Proc. Natl. Conf. Emerg. Trends Adv. Comput.*, 36–40.
- Themeßl, M. J., Gobiet, A., and Leuprecht, A. (2011). “Empirical-statistical downscaling and error correction of daily precipitation from regional climate models.” *Int. J. Climatol.*, 31(10), 1530–1544.
- Thomson, A. M., Calvin, K. V, Smith, S. J., Kyle, G. P., Volke, A., Patel, P., Delgado-arias, S., Bond-lamberty, B., Wise, M. A., Clarke, L. E., and Edmonds, J. A. (2011). “RCP4.5: a pathway for stabilization of radiative forcing by 2100.” *Clim. Chang.*, 109(1–2), 77–94.
- Treesa, A., Das, J., and Umamahesh, N. V. (2017). “Assessment of impact of climate change on streamflows using VIC model.” *Eur. Water*, 59(2013), 61–68.
- Trzaska, S., and Schnarr, E. (2014). *A review of downscaling methods for climate change projections*.
- Tu, J. (2009). “Combined impact of climate and land use changes on streamflow and water quality in eastern Massachusetts, USA.” *J. Hydrol.*, 379(3–4), 268–283.
- Uyanık, G. K., and Güler, N. (2013). “A study on multiple linear regression analysis.” *Procedia - Soc. Behav. Sci.*, 106, 234–240.